Neutron Spectrum Unfolding with Organic Scintillators for Arms-control Verification

by

Christopher C. Lawrence

A dissertation submitted in partial fulfillment
of the requirements for the degree of
Doctor of Philosophy
(Nuclear Engineering and Radiological Sciences)
at The University of Michigan
2014

Doctoral Committee:

       Associate Professor Sara A. Pozzi, Co-Chair
       Emeritus Professor Frederick D. Becchetti Jr., Co-Chair
       Associate Research Scientist Marek Flaska
       Emeritus Professor Ronald F. Fleming
       Professor James P. Holloway
       Associate Professor Clayton D. Scott

Acknowledgements

Table of Contents

List of Figures

List of Tables

List of Abbreviations

DNNG   Detection for Nuclear Nonproliferation Group

HE   high explosive

UND-NSL   University of Notre Dame Nuclear Structure Laboratory

PHS   pulse-height spectrum (spectra)

PMT   photo-multiplier tube

PSD   pulse-shape discrimination

SNM   special nuclear material(s)

TOF   time of flight

Chapter 1
Neutron Spectrum Unfolding for
Warhead Verification

Nuclear-disarmament activists and treaty-verification practitioners have posed an unusual class of measurement challenge. In the warhead-dismantlement scenario they envision, the disarming party must demonstrate certain treaty-relevant attributes of a sample - the metallic state of plutonium, the presence of high explosives, etc. - while obscuring other attributes deemed sensitive information about weapons design. The test item is often imagined as located inside some agreed-upon container which precludes direct visual inspection, but which is permeable to various radiative, acoustic or electromagnetic couplings so that limited measurement techniques can be used to gather information about the item [1]-[6]. Unlike traditional measurement tasks, in which data acquisition is often an unmitigated good, here we are as interested in obscuring some forms of information as we are in measuring others. And in planning for these exotic challenges, we face not just one set of *known* political constraints and priorities, but a range of *unknown* possible constraints in a hypothetical future context.

This set of challenges is bound to motivate some unusual choices amongst available measurement technologies. Previous applications calling for the detailed characterization of weapons components and special nuclear materials (SNM) have often been met with extremely sensitive measurements like high-resolution gamma-ray spectroscopy. But the data from these contain a wealth of classified design information, and would require the use of delicate information barriers which are difficult, or impossible, to validate. Instead, it may be necessary to develop measurement systems that don't simply *obscure* sensitive data, but which never physically acquire it in the first place. And to prepare for the nebulous political future, we are wise to develop a *collection* of measurement tools with complimentary (in)sensitivities, rather than a particular favored system.

Toward this end, I have decided to revisit the prospects for single-detector neutron spectroscopy[i]. Neutron spectra emanated from SNM contain much less information than gamma-ray spectra, but may still bear defining weapons-attribute information. Sensitive design informations like plutonium isotopics, pit mass, and shape could not be revealed by neutron spectroscopy of any realizable resolution, but the relatively broad features of neutron spectra can often be used to distinguish between fission and non-fission sources. Taken in conjunction with other forms of data - limited multiplicity counting, low-resolution gamma-ray spectra, tomographic imaging, etc. - neutron spectroscopy could help constrain an inspectorate's ignorance about a treaty-relevant test item.

But due to the neutron's weakly-interacting nature, neutron spectroscopy is much more difficult (and interesting) than gamma-ray spectroscopy. Gamma-rays can interact quite readily with the Coulomb fields associated with electrons in matter, so that it is easier to devise a detection medium that will absorb the full energies of incident gamma rays. Detection of fast neutrons, on the other hand, relies on elastic scattering[ii], which has little "preference" for the fractional transfer of energy from neutrons to detecting medium. This leads to detector response matrices that are highly ill-conditioned, such that common neutron spectra can't be visually interpreted from detector pulse-height data the way gamma-ray or charged-particle spectra often can. Instead, they must be "unfolded", and neutron-spectrum unfolding is a notoriously difficult inverse problem. Indeed, mathematicians and nuclear scientists alike have battled the problem for decades, and have come up against hard informatic limits that constrain the possible fidelity of the unfolded solutions. This difficulty has largely relegated fast-neutron spectroscopy to dosimetry applications, for which resolution of fine spectral features is unnecessary.

In order to utilize unfolded neutron spectra for treaty verification, we must carry spectrum unfolding from dosimetry applications into a more demanding class of applications - that of source and material characterization. The prospects for this are somewhat dimmed on first look at the literature - mathematical techniques for inverting ill-conditioned matrices are already well

---

[i] I specify "single detector" to distinguish from time-of-flight spectroscopy, which is not practical for most verification scenarios.

[ii] Exceptions to this will be discussed in Chapter 2. The term "fast" neutrons refers roughly to neutrons out of thermal equilibrium with room-temperature media.

developed, as is their application to spectrum unfolding. Many spectrum-unfolding codes are currently available, and they draw on a variety of theoretical frameworks. The current state of their development is such that the quality of unfolding results is "almost independent of the (choice of) code applied" [7]. In general, stable solutions can be obtained with neutron-energy groupings as fine as 200-300 keV, and this is probably insufficient for verification applications. At this stage of developmental saturation, it is unlikely that further development of algorithms will yield better unfolding results, for a given response matrix, than current algorithms are able to produce.

So I take a different approach. Instead of seeking better mathematical techniques for inverting an ill-conditioned matrix, I look for ways to improve the condition of the matrix. The possibilities for this are diverse, but generally require a focus on the *particular* - the *particular* measurement system and the *particular* measurement challenge. This is in contrast to much of the literature which focuses on the *general* conceptual frameworks that ground the unfolding methods. Indeed, unfolded spectra from actual measurements in the reported literature are surprisingly scarce, as are comparisons between different detection systems. While the general techniques and sensibilities of the inverse-problem solver are of great necessity for unfolding, I intend to realize hidden opportunities for improving unfolding capabilities by shifting the focus to the measurement system and measurement task.

This thesis presents a series of developments for neutron-spectrum unfolding with organic scintillation detectors, with an aim at future applications in the verification of arms-control agreements. First, by focusing on the attributes of the detector itself and their effects on the solution stability, I will surpass the limitations described above, and present unfolded spectra with 100-keV-wide energy groupings. This focus on the detection system will be facilitated by accelerator-based time-of-flight (TOF) measurements carried out at the Nuclear-structure Laboratory of the University of Notre Dame. Time-of-flight techniques will permit the detailed measurement of detector response matrices and other attributes, as well as independent measurement of reference spectra for the validation of unfolding trials. The unfolding performance for three different organic scintillators will be compared - the hydrogen-based liquid EJ309, the deuterium-based liquid EJ315, and the hydrogen-based plastic EJ299-33. This

will elucidate the influence of scattering kinematics (*n-p* versus *n-d* scattering), scintillation light output, and pulse-height resolution on response-matrix condition.

Second, I will describe how a particularized consideration of the measurement challenge at hand can facilitate a re-parametrization of the unfolding problem, and dramatically constrain the solution space. This could allow the induction of treaty-relevant parameters that would otherwise be unavailable from scintillator pulse-height data. I will focus on a simplified, one-dimensional case in which the elemental composition of a neutron-attenuating slab is revealed by its differential attenuation of neutrons passing through it. This is inspired by a variant of the warhead-verification scenario envisioned above, which includes an arrangement of near-spherical symmetry where neutrons emitted by the fissioning content of a plutonium pit are passed through concentric shells of neutron-reflecting and high-explosive materials, before reaching a surrounding detection system. The low-Z components of these materials have well-known and distinguishing features in their energy-dependent neutron-interaction cross sections, and this information can be taken into account to constrain the inverse problem. While the realistic three-dimensional case differs substantially from the simplified one-dimensional case, my demonstration provides a first step in this new direction for solving unfolding problems in treaty-verification scenarios.

Given my focus on the measurement system and particular measurement task, little attention will be given to the unfolding algorithm itself. I argue that this isn't a negligence, but simply a re-focusing of efforts on the aspects of the unfolding problem that I believe are under-addressed in the prevailing literature. Detailed reviews of unfolding procedures are given in references [8]-[10], and it would be superfluous to channel them here. Likewise, comparison between the performances of different unfolding codes are widespread, for instance in [11], [12]. Readers interested in the particulars of scintillator response or the history of neutron spectroscopy are directed to the references [13] and [14], [15] respectively. I will attempt here to convey a *qualitative* and *intuitive* understanding of the instability of unfolded solutions, and how it arises from the 'flatness' of scintillator-pulse-height response to fast neutrons. I will then give a brief description to the two main categories of approach to the unfolding problem - those which treat it as a matrix-inversion problem in need of some stabilizing perturbation or constraint, and those which approach it as an inference problem calling for Bayesian or thermodynamic

formalisms. When I unfold measured spectra, I will employ the simplest options available for unfolding: for linear matrix inversion I will use a conjugate gradient method [16], [17], and stabilize the solution with Tikhonov regularization [18]-[20]; for inversion of nonlinear operators, as will be required for the re-parametrized attenuation problem, I will use the common Levenberg-Marquardt algorithm [21].

It is also important to situate my efforts with scintillators amongst the other options available for neutron spectroscopy, and amongst the prevailing conceptions of the coming warhead-verification problem. A deployable system will ultimately require further improvements on the detection system to achieve the unfolding performance I describe here. I will specify fieldable improvements that I envision involving currently-available technologies like automated detector calibration and temperature control. Deployable systems will also require more advanced unfolding methods than I use here. Additionally, other options for the detection medium exist, and may prove superior to organic liquids[iii]. Finally, detailed knowledge of neutron spectra emitted from treaty-relevant test items would only be useful in conjunction with other forms of information. With these qualifications, my overall aim is to demonstrate that neutron spectroscopy techniques - either with organic scintillators or some improved detector - could be a useful addition to the overall treaty-verification toolbox.

References

[1]   J. Fuller, "Verification on the Road to Zero: Issues for Nuclear Warhead Dismantlement," *Arms Control Today*, pp. 1–11, Jul. 2010.

[2]   T. B. Taylor, "Verified Elimination of Nuclear Warheads," *Science & Global Security*, vol. 1, pp. 1–26, Mar. 1989.

[3]   F. von Hippel, "Verification of Nuclear Warheads and Their Dismantlement: A Joint American-Soviet Study," presented at the Institute for Nuclear Materials Management, 31st Annual Meeting, 1990, pp. 1–3.

[4]   R. Kouzes and B. Geelhood, "Methods for Attribute Measurement and Alternatives to Multiplicity Counting," Pacific Northwest National Laboratory, PNNL-13250, May 2000.

[iii] However, the developments described here will still be relevant for unfolding and extracting treaty-relevant information from a hypothetical future detector. It would simply have a better-conditioned response matrix, which is precisely the type of improvement argued for here.

[5] R. Whiteson and D. W. MacArthur, "Information Barriers In the Trilateral Initiative: Conceptual Description," Los Alamos National Laboratory, LAUR-98-2137, Mar. 1998.

[6] R. Waldron, "Arms Control and Nonproliferation Technologies, Spring 2001," Office of Nonproliferation Research and Engineering, Sep. 2001.

[7] H. Klein, "Neutron Spectrometry in Mixed Fields: NE213/BC501A Liquid Scintillation Spectrometers," *Radiation Protection and Dosimetry*, vol. 107, pp. 95–109, Dec. 2003.

[8] V. B. Anykeyev, A. A. Spiridonov, and V. P. Zhigunov, "Comparative Investigation of Unfolding Methods," *Nuclear Instruments and Methods in Physics Research A*, vol. 303, pp. 350–369, Jul. 1991.

[9] M. Matzke, "Unfolding Procedures," *Radiation Protection and Dosimetry*, vol. 107, no. 1, pp. 155–174, Dec. 2003.

[10] M. Reginatto, "Overview of spectral unfolding techniques and uncertainty estimation," *Radiation Measurements*, vol. 45, no. 10, pp. 1323–1329, Dec. 2010.

[11] R. Koohi-Fayegh, S. Green, and M. C. Scott, "A Comparison of Neutron Spectrum Unfolding Codes Used with a Miniature NE213 Detector," *Nuclear Instruments and Methods in Physics Research A*, vol. 460, pp. 391–400, Mar. 2001.

[12] B. Pehlivanovic, S. Avdic, P. Marinkovic, S. Pozzi, and M. Flaska, "Comparison of Unfolding Approaches for Monoenergetic and Continuous Fast-neutron Energy Spectra," Oct. 2011.

[13] J. Birks, *Theory and Practice of Scintillation Counting*. Pergemon Press.

[14] D. J. Thomas, "Neutron spectrometry," *Radiation Measurements*, vol. 45, no. 10, pp. 1178–1185, Dec. 2010.

[15] F. D. Brooks and H. Klein, "Neutron Spectrometry - Historical Review and Present Status," *Nuclear Instruments and Methods in Physics Research A*, vol. 476, pp. 1–11, Dec. 2001.

[16] M. Hestenes and E. Stiefel, "Methods of Conjugate Gradients for Solving Linear Systems," *Journal of Research for the National Bureau of Standards*, vol. 46, pp. 1–28, Sep. 1952.

[17] J. R. Shewchuk, *An Introduction to the Conjugate Gradient Method Without Agonizing Pain*. 1994, pp. 1–64.

[18] D. Phillips, "A Technique for the Numerical Solution of Certain Intergral Equations of the First Kind," pp. 1–14, Feb. 1961.

[19] P. C. Hansen, *The L-curve and Its Use in the Numerical Treatment of Inverse Problems*. 2003, pp. 1–24.

[20] P. C. Hansen, "MATLAB Regularization Toolbox," *Numerical Algorithms*, vol. 46, pp. 189–194, Mar. 2007.

[21] R. Fletcher, "Modified Marquardt Subroutine for Non-linear Least Squares," United Kingdom Atomic Energy Authority, AERE - R 6799, Oct. 1971.

Chapter 2
Organic Scintillators for
Neutron Detection

Neutron-detection systems can generally be divided into two categories: those which rely on neutron capture, and those relying on nuclear elastic scattering. These two categories can in turn be associated with different energy ranges. Since the relevant neutron-capture cross sections drop sharply with energy, capture detectors such as ^{3}He tubes are typically used to detect thermal neutrons[iv]. Detecting fast neutrons with capture detectors requires prior moderation in some hydrogenous medium like polyethylene, whereby energy information about incident neutrons is largely lost [1], [2]. Recoil detectors are more commonly used to detect fast neutrons because the cross sections for elastic scatter (e.g. *n-p*, *n-d*, etc.) are substantial at high energies. Nuclear recoil detectors also make better spectrometers since they can better preserve energy information [3]. While a variety of recoil detection systems are available, I focus here on organic scintillators because they strike a balance between detection efficiency and preservation of energy information [4]. While detection systems exist which offer better preservation of energy information, these have detection efficiencies on the order of 0.01% to 0.1% [5], which is likely problematic for warhead measurements. Organic scintillators have efficiencies ranging from 10% to 60% depending on the size of the active volume, and thus are generally more suitable [6].

A scintillating material is one which produces a small flash of light upon Coulomb interaction with charged-particle radiation [7]. Molecules of these materials have energy-state structures that allow excitation and de-excitation via different routes, such that they can produce de-excitation photons to which the materials themselves are almost completely transparent [1],

---

[iv] The term "thermal" is colloquially used to describe neutrons which have come to thermal equilibrium with room-temperature media, such that their energies are on the order of tens of eV. This is in contrast to "fast" neutrons which are emitted from nuclear interactions with energies in the MeV range. Fission neutrons range in energy from around 0.5 - 15 MeV.

[7]. This light can be collected in a photo-multiplier tube[v] (PMT) and converted to a voltage pulse for analysis (see Fig. 2.1). Measurement data from a scintillation detector is commonly represented as a "pulse-height spectrum" (PHS) $n(L)$, where the dependent "pulse-height" variable L represents the "size" of the scintillation pulse - often proportional to the integrated charge Q on the PMT anode for a given pulse - and n is simply the count of measured pulses detected per unit of pulse height L.
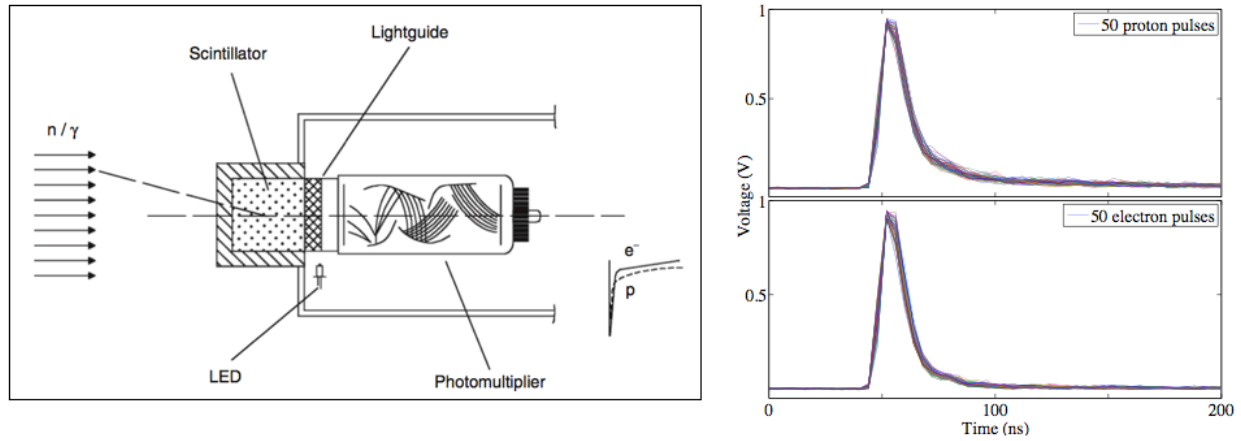
FIG. 2.1. Collection of scintillation light in a photomultiplier tube. The left figure shows a diagram of the scintillation material connected to the photomultiplier tube (PMT) (reproduced from Ref. [8]). The right figure shows fifty overlapped voltage pulses from the anode of a PMT collecting light from proton-induced (above) and electron-induced scintillations in the hydrogen-based liquid EJ309 (below). Proton pulses are associated with *n-p* elastic scattering, and represent neutron detections, while electron pulses are associated with Compton scattering, and represent gamma-ray detections.

Since a neutron cannot directly trigger the scintillation process, it first must scatter on some nucleus - typically hydrogen or carbon - which in turn excites the scintillator material to produce a pulse. Therefore, the scintillating material is often dissolved in some hydrogenous solvent to provide ample scattering centers for incoming neutrons to interact with. The resulting solution may be in liquid, crystal or amorphous-solid form, some volume (on the order of tens to hundreds of cubic centimeters) of which is optically coupled to a PMT. The kinematics of the scattering process, the numbers of scintillation photons produced, the time characteristics of the

---

[v] It should be noted that there are other options for light collection, including silicon photodiodes. However PMTs are the common choice.

scintillation processes, and the efficiency of light collection are all important factors in scintillator pulse-height response, and they depend in part on the choice of scintillator material and solvent. In addition, low-*Z* organic scintillators are also sensitive to gamma rays by route of Compton scatter on electrons, which then excite the scintillator material. So an important requirement of a scintillation detector for neutron spectroscopy is the ability to distinguish between neutron- and gamma-ray-induced pulses. Thus, choice of solution for a scintillation detector is subject to multiple, often competing considerations. This chapter will provide a qualitative overview of the concepts of interest to give an intuitive sense of how we can alter detector performance. Much more detailed treatment is given in Ref. [7].

2.1 Pulse-height response of organic scintillators to neutrons

We begin with an outline of the physical processes that lead to detection of a neutron in a scintillation detector, and the complications that each process adds to the coupling between incident neutron energy E_n and resulting pulse height L. A simplified description is as follows:

1) A neutron entering the detector medium with incident energy E_n has some finite probability of elastically scattering one or more times on either hydrogen or carbon, and thereon transferring energy $E_p \leq E_n$ on the pth collision. The neutron leaves the detector medium with remaining energy $E_n - \sum E_p$.

2) The recoiling particles (indexed by p) slow down by transferring their energy into the surrounding detector medium via the Coulomb interaction. Some of that energy excites scintillating molecules, which subsequently de-excite to produce scintillation light L_{scint}. The fraction of energy deposited via scintillating channels is governed primarily by the linear density of energy loss along the particle track, such that

$$L_{scint} = \sum_p f(A,Z,E_p) \tag{2.1}$$

where A and Z are atomic mass and number respectively. L_{scint} is generally non-linear in E_p.

3) L_{scint} is distributed amongst a collection of scintillation photons, with the attendant Poisson variance, most of which are collected in a PMT to produce a pulse of total integrated charge Q on the anode. The charge Q is converted through a calibration relation into an observed L_{obs} so that, in principle, L_{obs} is drawn from a Poisson distribution of mean L_{scint}. The observed quantity is referred to as the "pulse height" [vi].

To further illustrate, imagine a stream of mono-energetic neutrons of energy E_n, and consider for now only single scatters on hydrogen nuclei (see Fig. 2.2). In an ideal spectrometer, we would like to see a PHS $n(L)$ containing a single peak, whose location L_0 along the pulse-height axis depends linearly on the incident energy E_n. This type of spectral response would require no unfolding. But steps 1-3 listed above each introduce dramatic defects such that the observed $n(L)$ deviate substantially from this ideal.

Step 1 is largely governed by scattering kinematics, and the angular dependence of the n-p cross-section is flat over our energy range of interest. Thus, the resulting distribution over E_p looks somewhat like a step function which extends to the full incident energy E_n. Step 2 is similar to a quenching effect. As the recoiling particle traverses through the detecting medium, it saturates the excitable scintillating systems within the locality along its path, and excess energy is lost to non-scintillating systems. Slower recoil particles deposit their energy with a greater linear density dE/dx along the path, and thus saturate the available scintillating systems more quickly. This means that a greater fraction of their initial energy is lost to non-scintillating systems. Faster recoil particles deposit their energy with lower linear density dE/dx, and thereby have access to more scintillating systems on which to deposit their energy. This introduces a nonlinearity to the relation between energy E_p deposited onto a recoil particle, and the amount of energy transferred to scintillating systems E_{scint} (see Fig. 2.3), which in turn tends to compress features along the low end of the pulse-height axis.

[vi] This may be counter intuitive, since the anode pulse is integrated. However, anode signal is traditionally processed via a shaping amplifier, and height of the processed pulse is recorded - hence the descriptor "pulse height". The hight of the processed pulse is proportional to the integral of the anode pulse.
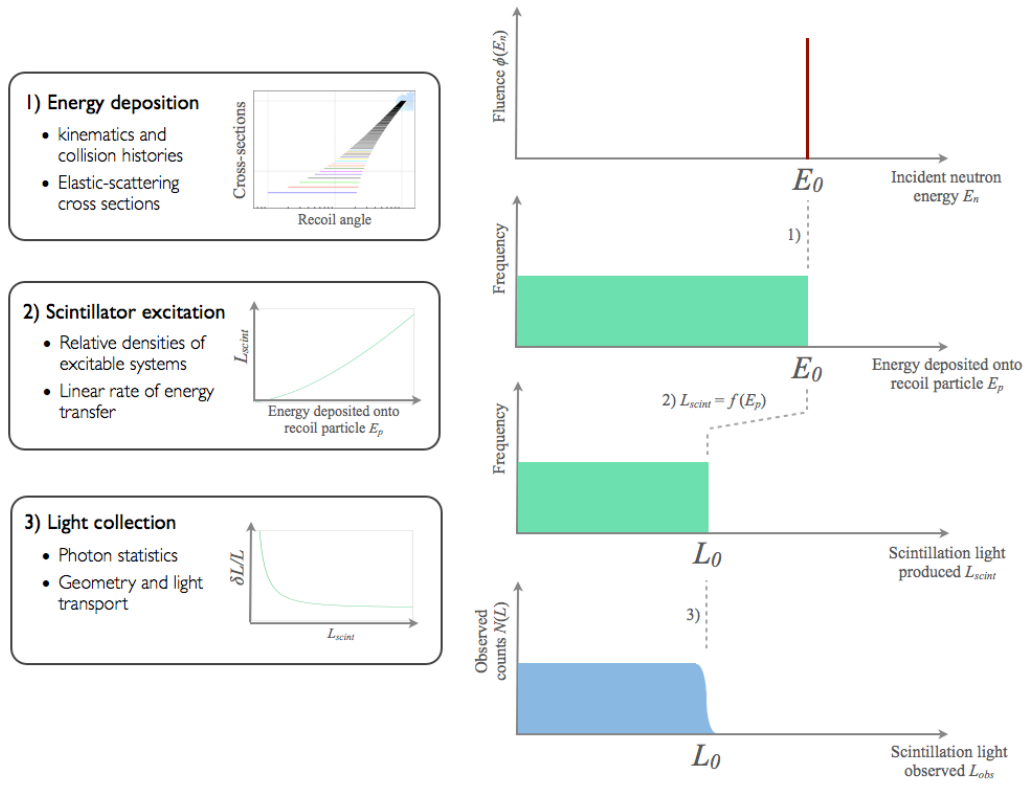
FIG. 2.2. Sequence of physical processes leading to the detection of mono-energetic neutrons in an organic scintillation detector, along with a simplified illustration of the effect of each process on the shape of the observed pulse-height spectrum (PHS) $n(L)$.
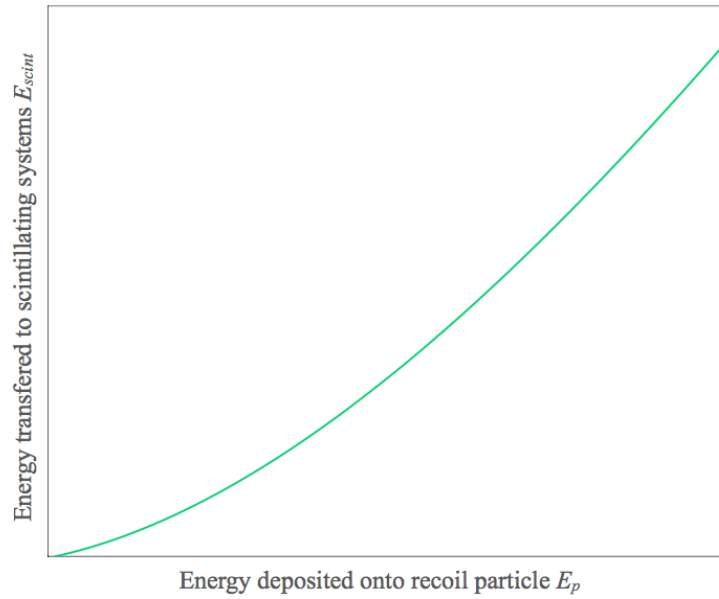
FIG. 2.3. Nonlinear relation $L_{scint}(E_p)$ between energy E_p deposited onto a recoil nucleus and the resulting scintillation light Lscint produced in the slowing-down process.

Step 3 introduces a blurring or "resolution" effect. Since the scintillation light L_{scint} is released in a population of photons prior to collection in a PMT, there is a Poisson variance added to the observed flash:

$$\frac{\delta L_{obs}}{L_{obs}} \propto \frac{1}{\sqrt{E_{scint}}} \ .$$

(2.2)

This blurs the features in the observed PHS $n(L)$. Thus, the predicted observable PHS $n(L)$ from our simplified model looks like a blurred step function, as shown in the lower right portion of Fig. 2.2.

A more complete treatment would consider the contributions of alternative collision histories, and this is provided in Refs. [9], [10]. Here, I will mention two important contributions to the observed PHS, beginning with neutrons that collide twice on hydrogen. Through a convolution of two step functions, it can be shown that the resulting contribution to the PHS contains a prominent hump at a pulse-height location L which is shifted downward slightly from the pulse-height L_o corresponding to single-collision full-energy deposition (see Fig. 2.4) [9].
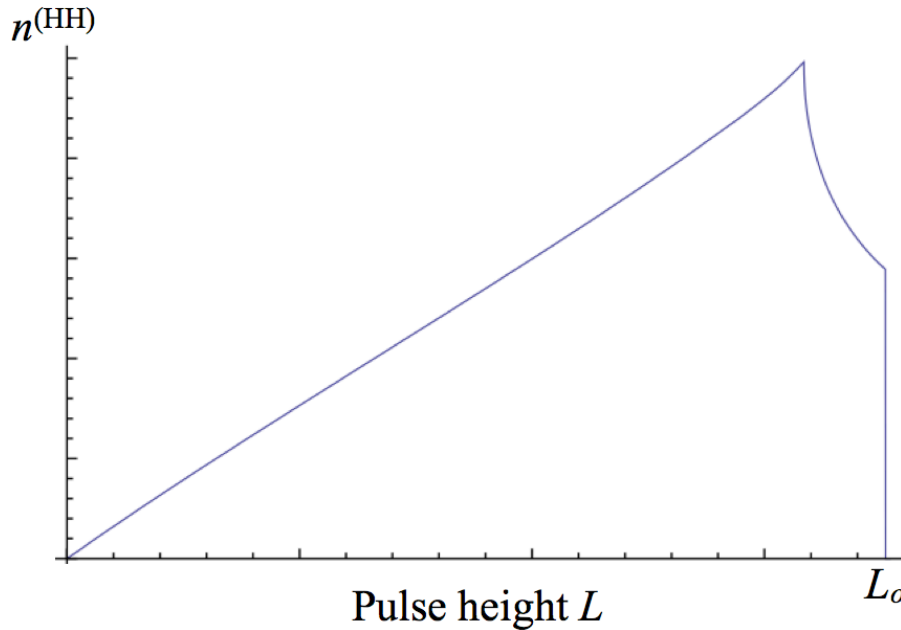
FIG. 2.4. The component $n^{(HH)}(L)$ to the observed PHS $n^{(obs)}(L)$ contributed by neutrons which collide twice on hydrogen (resolution not included). Other collision histories with multiple collisions have a similar "peaking" effect, and together result in a small deviation of $n^{(obs)}(L)$ from step-function-like shape [9].

The other category of collision history that should be mentioned are those which involve carbon nuclei. Since the linear density of *dE/dx* of energy deposited along the track length is higher for larger recoil particles, saturation of locally-available scintillating systems is reached with a smaller amount of energy, and more energy is "wasted" on non-scintillating systems. Thus, heavier recoil particles produce less light for a given initial energy E_p. Additionally, the maximum energy deposited in a neutron collision on a nucleus of size *A* is given by

$$E_p^{max} = \frac{2A}{(A+1)^2} E_n$$

(2.3)

so that a neutron can only deposit up to 14% of its energy onto ^{12}C nucleus in a single collision. These effects taken together indicate that the light output from carbon will be very small over most of our energy range of interest, and this is in fact the case. Collisions on carbon can alter the shape of the PHS by absorbing energies from neutrons which may then collide on hydrogen, but the resulting contribution to the PHS is similar to that shown in Fig. 2.4.

Figure 2.5 shows measured PHS for quasi-mono-energetic neutron spectra of several energies across the fission-energy range[vii]. With the exception of multiple-collision effects mentioned, they generally look like the blurred step functions we expect from *n-p* scattering. The nonlinearity of the light output relation is betrayed by the fact that separation between edges increases with increasing pulse height, even though the incident neutron energies E_n are evenly spaced in steps of 1 MeV. And the blurring effect from Poisson statistics is apparent in the gradual drop off of each step-function edge.

_____

[vii] The dependent "pulse-height" variable *L* is presented in units of MeV "electron equivalent", or MeVee. The MeVee scale is defined in relation to PHS from standard gamma-ray calibration sources. One MeVee is the amount of light produced by a 1-MeV electron stopping in the detector active volume.
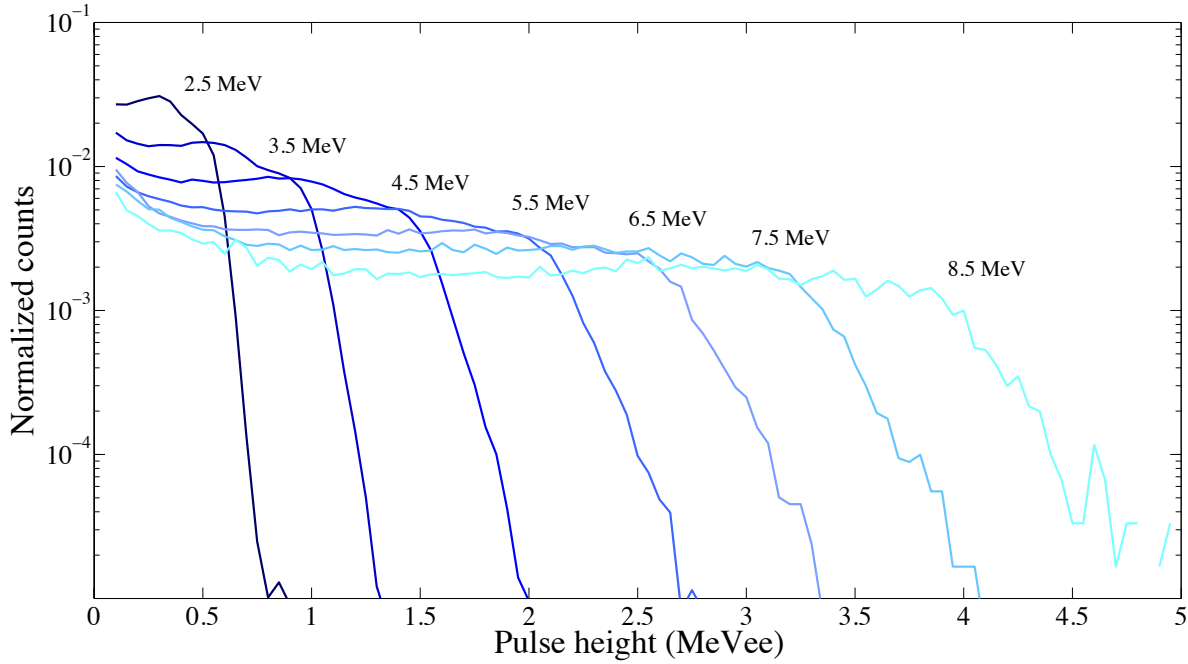
FIG. 2.5. Measured PHS $n(L)$ in a hydrogen-based EJ309 from quasi-mono-energetic neutron spectra selected with 100-keV-wide time-of-flight gates.

To begin to understand why spectrum unfolding is required with this type of pulse-height response, consider neutron spectra $\phi(E_n)$ that contain multiple energies. Each energy component $\phi^{(j)}$ in $\phi(E_n)$ would result in an independent step-function-like component $n^{(j)}$, all of which are superimposed in the overall observed $n^{(obs)}(L)$. As more energy components are added, $n(L)$ becomes more difficult to interpret. When measuring the continuous fission-neutron spectra relevant to arms-control applications, we are faced with a superposition of infinitely many step functions, such that $n(L)$ are nearly impossible to interpret visually. As an illustration, consider two very different neutron spectra shown in Fig. 2.6. The left-most figure depicts the spectrum of neutrons produced by a ^{252}Cf fission source (lighter, smooth red curve), as well as the same spectrum passed through two inches of tap water[viii] (darker, jagged curve - both are normalized for convenient portrayal). These very different neutron spectra, incident on a liquid scintillator,

---

[viii] The energy-dependent neutron-interaction cross section of oxygen differentially attenuates neutrons of different energies, introducing stark features to the neutron spectrum.

produce the pulse-height spectra shown in the right half of the figure, which are much less distinguishable.
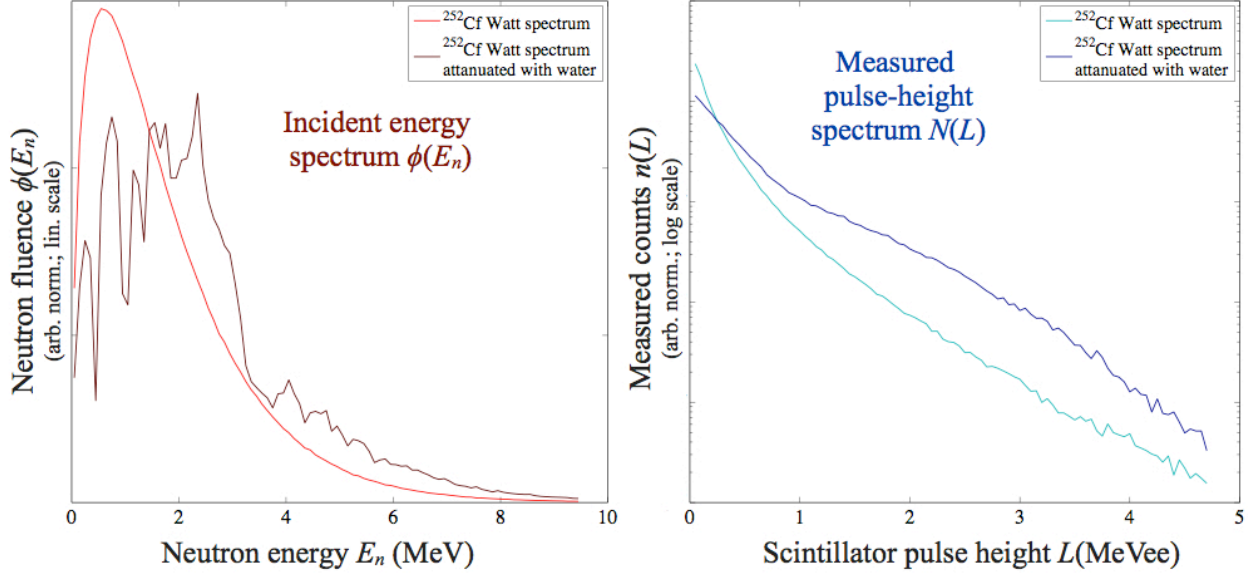
FIG. 2.6. Examples of continuous neutron spectra $\phi(E_n)$, and the resulting observable PHS $n(L)$ from the organic liquid scintillator EJ309. Distinguishable features in $\phi(E_n)$ are not visually observable in $n(L)$, resulting in the need for spectrum unfolding.

The relation between incident neutron energy spectrum $\phi(E_n)$ and resulting PHS $n(L)$ can be represented as a first-order Fredholm convolution:

$$n(L) = \int R(E_n,L)\, \phi(E_n)\, dE_n \tag{2.4}$$

where $R(E_n,L)$ is the detector response matrix - a mapping of the probabilistic coupling between incident neutron energy E_n and resulting pulse height L. The meaning of $R(E_n,L)$ is as follows: given a neutron of energy E_n incident on the detector, $R(E_n,L)$ is the probability that the detector will produce an observable pulse of height L. Figure 2.7 shows a representative response matrix for a hydrogen-based liquid scintillator EJ309, simulated in MCNP-PoliMi [11]. Each column of $R(E_n,L)$ at a fixed energy E_n corresponds to the PHS we expect from mono-energetic neutrons of energy E_n. Given the probabilistic meaning of $R(E_n,L)$, it should be normalized such that each column integrates to the detection efficiency $\epsilon(E_n)$ at the energy corresponding to that column.

This is the matrix which must be inverted in the unfolding process - its ill condition can be associated with its general flatness and lack of feature.
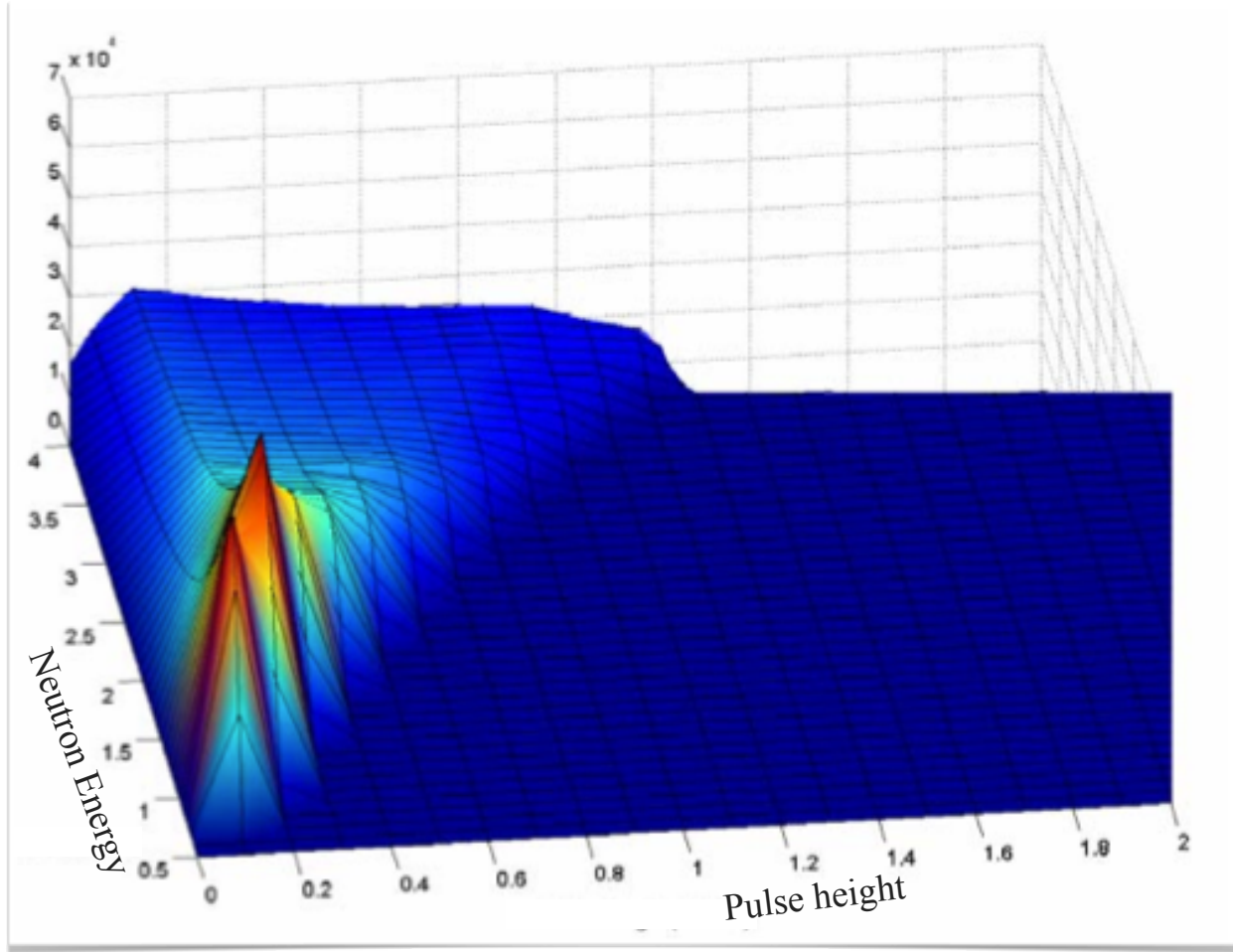
FIG. 2.7. An example of a response matrix $R(E_n,L)$ for a hydrogen-based EN309 scintillation detector, simulated with the Monte Carlo program MCNP-PoliMi [12], as reported in Ref. [11]. Response matrices presented and used in this thesis were measured using accelerator experiments.

2.2 Pulse-shape discrimination for *n-γ* identification

As mentioned above, organic scintillation detectors are sensitive to gamma rays as well as neutrons. The physical processes leading to detection of gamma rays are similar to those resulting in neutron detection, with the exception that elastic scattering of neutrons on target nuclei is replaced with Compton scattering of gamma rays on molecular electrons. Fortunately, many scintillator solutions enable *n/γ* identification through pulse-shape discrimination (PSD).

For these materials, the nuclei-induced pulses (associated with neutron detection) have a slightly more pronounced tail than those induced by recoil electrons (associated with gamma rays) [3], [13]. This can be seen in the right portion of Fig. 2.1.

The difference in pulse shape results from the fact that there are two categories of scintillating de-excitation paths, each with a significantly different time characteristic. Direct fluorescence results from excitation and de-excitation amongst singlet vibrational states in the scintillating molecules, and this contributes the bulk of the scintillation pulse. But some excited molecules transition to longer-lived triplet states prior to de-excitation, and this leads to delayed fluorescence. The fraction of excited systems that transition to triplet states is related to the density of singlet states that are initially excited. A larger and more durable local population of excited singlet states will more readily "feed" the adjacent triplet states. And we saw before that the spatial density of excited scintillation molecules is related to the linear density of energy loss dE/dx of recoiling charged particles, which for a given energy E_p is proportional to the particles' mass. Since nuclei are much more massive than electrons, they lead to larger relative populations of delayed-fluorescing triplet states, and thus more prominent tail contribution to the observed scintillation pulses [7].

A standard way to perform PSD is to take two integrals of each scintillation pulse - one of the entire pulse, and a second of the "tail" of the pulse - and plot the tail integral versus the total integral. Figure 2.8 shows an example of a standard PSD plot for 10^5 pulses measured from a ^{252}Cf fission source with a three-by-two-inch EJ309 detector. Neutron events are clearly separated from gamma-ray events, and can be distinguished by placing a gate around that distribution. The separation between neutron and gamma-ray distributions in a standard PSD plot is variant across different scintillator solutions. Crystals like stilbene and p-terphenyl tend to produce PSD separation superior to that of liquids. We will find that deuterated scintillators have similar PSD performance to standard hydrogen-based liquids. Since PSD performance can substantially affect unfolding results, it is an important attribute of detector performance for any scintillating neutron spectrometer.
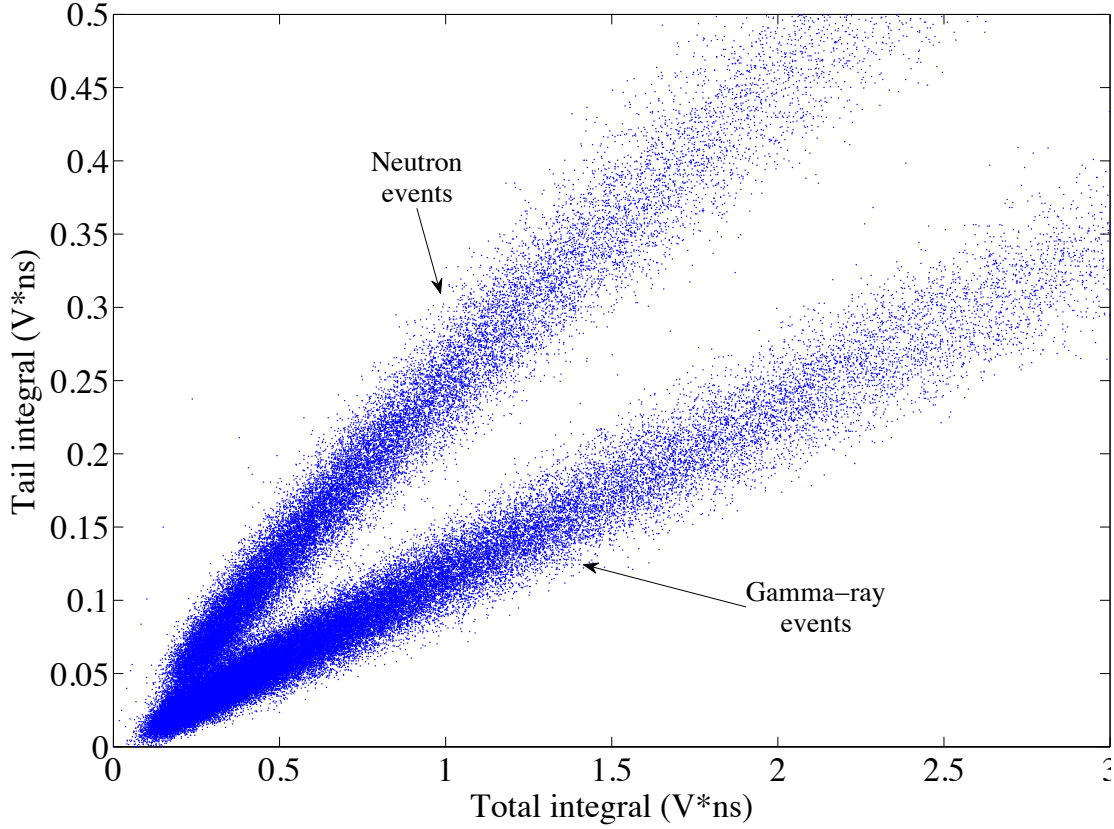
FIG. 2.8. Standard PSD plot - tail integral versus total integral - for 10^5 scintillation pulses from a ^{252}Cf fission source measured in a hydrogen-based EJ309 detector.

2.3 Venues for the improvement of spectrum-unfolding performance of organic scintillators

In Chapter 3, we will develop an understanding of the instability of the spectrum-unfolding problem. Here, suffice it to say that with an ill-conditioned response matrix R, small perturbations η in the detector response $n(L)$ are "amplified" by the inversion process, resulting in large error components ε in the unfolded spectra $\phi(E_n)$. In order to understand how we might improve unfolding results, we can distinguish between improvements in the condition of R that may dampen the amplification of η, and improvements in the stabilization of detector performance which lead to smaller η to begin with. Here we outline some possible improvements from both categories.

2.3.1 Deuterated scintillators: *n-d* versus *n-p* scattering

As described above, one of the main factors that complicate the pulse-height response of organic scintillators is the scattering kinematics of the dominant neutron interaction. Since most detected neutrons only collide once within the detection medium, the broad features of the pulse-height response to neutrons of a given energy correspond to the angular dependence of scattering cross section [1]. Previous studies of neutron spectrum unfolding are almost exclusively done with hydrogen-based liquids like NE213 or BC501A[ix]. With their reliance on *n-p* scattering, which is isotropic in the center of mass frame, hydrogen-based scintillators represent a sort of worst case scenario, yielding a response matrix $R(E_n,L)$ that is very flat (see Fig. 2.7). However, other scintillation detectors are available which employ "deuterated" solvents, like deuterated benzene. The response of deuterated scintillation detectors is dominated by *n-d* scattering, which is non-isotropic in the center-of-mass frame, and prefers backscattering. This preference yields a modest "backscatter peak" in the detector response to neutrons of a given energy [14], [15] (see Fig. 2.9). The corresponding "ridge" in the response matrix amounts to more "structure", and this is one of the ways we can improve the condition of the response matrix. While others have suggested that this may improve spectrum unfolding results [16], [17], demonstration of the unfolding capabilities of deuterated scintillators is absent from the literature, as is comparison with the standard hydrogen-based detectors. In this thesis, I will show a modest but significant improvement in spectrum unfolding performance for deuterated scintillators, over that of the hydrogen-based standard.

[ix] I refer here to "many-channel" spectrum unfolding, as opposed to "few channel" unfolding from Bonner-sphere or bubble-detetector arrays. Few-channel systems are only capable of rudimentary preservation of spectral features.
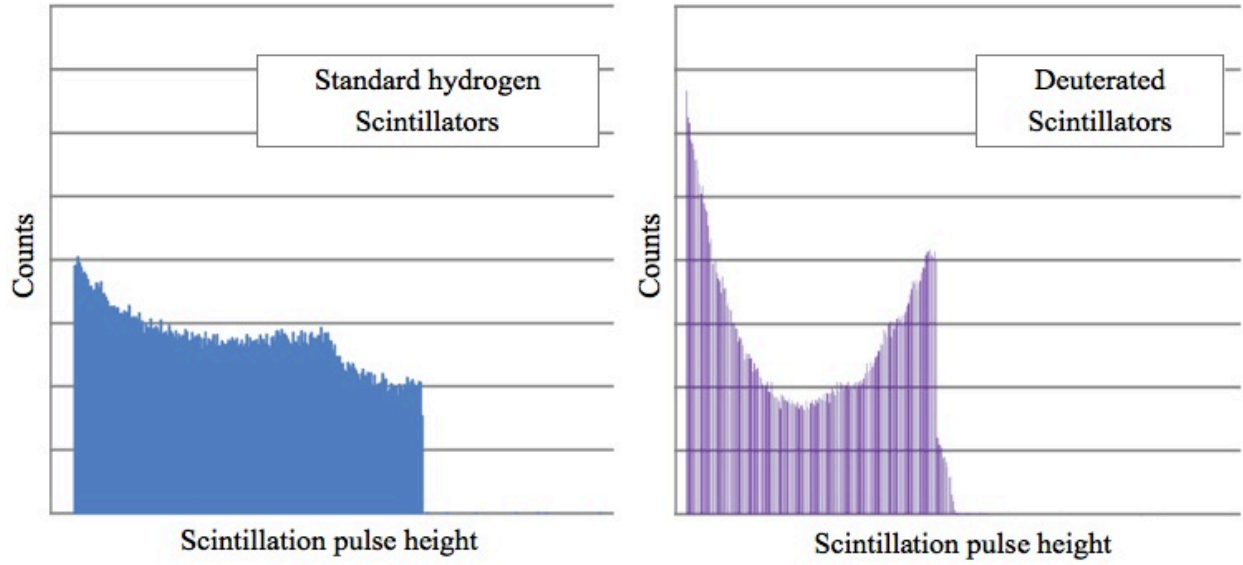
FIG. 2.9. Pulse-height spectra simulated for the hydrogen-based EJ309 and the deuterium-based EJ315, to mono-energetic neutrons of 2.5 MeV. The effect of scattering kinematics on the shape of the detector response is clearly shown. (Resolution is not included).

2.3.2 Energy resolution

The energy resolution of a scintillation detector has a significant impact on the condition of the response matrix, and it is a product of the pulse-height resolution and light-output attributes described above (section 2.1). The pulse-height resolution is a composite of multiple effects, and is dominated by Poisson variance. In general, it follows the relation [1]:

$$\left(\frac{\Delta L_{out}}{L_{out}}\right) = \sqrt{\alpha^2 + \frac{\beta^2}{L_{out}} + \left(\frac{\gamma}{L_{out}}\right)^2}. \tag{2.5}$$

This relation falls off sharply for small values of L_{out}, and approaches some asymptotic value α for large values. Thus, higher light-output $L_{out}(E_p)$ for a given deposition energy E_p results in smaller fractional resolution.

There is strong variation in both $L_{out}(E_p)$ and $\Delta L/L$ amongst scintillator options. For instance, some crystals like p-terphenyl and stilbene can be optimized to have $L_{out}(E_p)$ and $\Delta L/L$ that are superior to organic liquids or plastics. While crystals are often set aside due to their non-isotropic response (neutrons coming in at different angles w.r.t. the crystalline symmetry axes

produce different light-output relations), this would likely not be an issue in the controlled environments envisioned for warhead and material accounting. Unfortunately, these crystals were not readily available during the measurements reported here. Nevertheless, they may provide options for future improvement of response-matrix condition.

Plastic scintillators have recently gained much enthusiasm in the neutron-detection community, due to their wide deployment range [18]-[20]. However, they have inferior light output and resolution relative to common liquid scintillators. While these would be an unwise choice for warhead verification, where liquids and crystals would be unproblematic, they offer an interesting case to demonstrate the effect of energy resolution on response-matrix condition, and ultimately on unfolding results. Along these lines, a comparison between the unfolding performances of plastic and liquid scintillators will be presented, partially in hopes of motivating future development on neutron spectrometers composed of high-energy-resolution crystal scintillators.

2.3.3 Stabilization of detector performance

Spectrum-unfolding practitioners often note the importance of the "accuracy" of the response matrix, without elaborating on the meaning thereof. Plainly stated, the "accuracy" of the response matrix refers to how accurately the response-matrix operator R_{model} characterizes the pulse-height response of the detector *as deployed to measure n(L)*. Consider some field measurement $n^{(f)}(L)$ to be unfolded with response matrix $R_{model}(E_n,L)$, and ask the following questions:

- How well does R_{model} characterize the fielded spectrometer?
- Was R_{model} simulated? If so, with how accurately?
- Was R_{model} measured? If so, was it with the same detector setup? Geometry? PMT? etc.
- Even so, what about PMT gain? What about PSD performance? Are these the same for the modeled/measured R_{model} as for the fielded detector measuring $n^{(f)}(L)$?

With typical studies of the unfolding problem, detector response matrices R_{model} are simulated using Monte Carlo simulations, or drawn from archives of detector measurements found in

RSICC. Often these do not account for PSD misclassification, geometric variation, or other aspects of practical measurements $n^{(f)}(L)$. Also, PMT gain and PSD performance can shift during a measurement due to temperature changes and other environmental variations. Shifts of this sort result in a displacement of the real R_{real} from that represented in the simulated or measured model R_{model}, yielding a corresponding η which is in turn amplified by the inversion of the ill-conditioned matrix R_{model}. This displacement is part of what we want to characterize, and ultimately minimize, to improve unfolding results.

The most obvious discrepancy in detector performance results from shifts in PMT gain. The thermal properties of the PMT and associated electronics can evolve during the measurement and result in perturbations on the MeVee relation that was established prior to the measurement via gamma-ray calibration. In addition, temperature changes in the active volume of the detector can change detector performance. As these attributes shift, they move the features of the pulse-height response along the pulse-height L axis, leading to perturbations η.

Another important discrepancy in detector performance is associated with PSD performance. From Fig. 2.8, it is clear that the neutron and gamma-ray distributions merge at the low pulse-height end of the plot. This means that some neutrons will be lost to misclassification, while misclassified gamma-ray events will distort the shape of the low end of the observed PHS. While this is typically not included in simulated response matrices, it can be included in a measured response matrix. But shifts in PMT gain and pulse-height response can alter the respective neutron and gamma-ray distributions in the PSD plot (Fig. 2.8) relative to any pre-determined PSD gate settings, and thereby change the relative misclassification rates of neutrons and gamma-rays. Additionally, variation in n/γ ratio (of incident radiation) can change the absolute number of gamma-ray events which are misclassified and erroneously included as neutrons. This will alter the shape of the measured PHS $n^{(f)}$ relative to that predicted by R_{model}, and produce an additional η to be amplified in the unfolding process.

Current developments can improve many of these problems. Gain shifts can be stabilized by automated calibration systems that inject optical signals into the PMT during measurement to provide real-time calibration data, and alter the PMT voltage accordingly. Some chemical

additives to the scintillator solution can dramatically improve PSD separation, and automated methods for the placement of the PSD gate can remove shifts in PSD performance [21]. Thus, improvements to unfolding performance that can be derived from stabilizing PMT gain and PSD performance may be realized in future fieldable systems.

2.4 Scintillators chosen for this work

Table (2.1) lists the detectors used in this study. They are selected to demonstrate some of the features of detector response described throughout this chapter. Availability was also a factor - for instance I would have liked to evaluate a high-quality crystal like p-terphenyl or stilbene, but the crystals I had access to were not optimized for high light output or fine resolution.

TAB. 2.1. List of organic scintillators chosen for this study.

Description	Model	Dimensions (cyl)	Dist. feature for unfolding
Hydrogen-based liquid	EJ309	7.62cm dia. by 5.08cm length	Flat response matrix similar to NE213; n-p scattering
Deuterated liquid	EJ315	7.62cm dia. by 5.08cm length	Back-scatter feature from anisotropy of n-d scattering
PSD plastic	EJ299-33	7.62cm dia. by 7.62cm length	Poor energy resolution

The hydrogen-based liquid EJ309 was chosen for its similarity to the hydrogen-based standard NE213 by Nuclear Enterprises, or the Bicron equivalent BC501A. NE213 or BC501A are used in nearly all studies of many-channel spectrum unfolding, but were unavailable at the time my measurements were taken. EJ309 has been shown to perform very similarly to BC501A, with the exception of a higher flash point [22]. Since many suitable EJ309 detectors were available for this work, it was chosen as the hydrogen-based standard for comparison. The well-known deuterated liquid is deuterated benzene NE230 [17]. However, since Nuclear Enterprises is no longer manufacturing scintillators, we obtained the Eljen-technology equivalent EJ315, and this will be the deuterated liquid used for this thesis [14], [15]. In order to look at the effects of energy resolution, I also include the new PSD plastic EJ299-33 [18]. There is much interest in

EJ299-33 due to its wider fieldability [19], [23], [24], but we will find that its lower light output and poorer resolution make it a poor choice for detailed spectrum unfolding, and an interesting demonstration of the importance of these characteristics. Specification of the characteristics of the detector housings and electronics will be given in appendix.

2.5 Remarks

In this chapter, I have tried to convey an intuitive sense of the relevant features of scintillator pulse-height response, and some means by which they may be altered to improve unfolding capabilities. Two important factors were noted to affect the condition of the response matrix - scattering kinematics and energy resolution - and these factors have guided my choices in the detectors evaluated for this study. In Chapters 7 and 8 we will find that deuterated detectors offer a modest but significant improvement in unfolding response over standard hydrogen-based liquids, while the poor resolution of the PSD plastic degrades unfolding performance considerably. I also noted some aspects of detector performance which can shift between or during measurements to degrade unfolding results. In Chapter 8 I will utilize accelerator-based experiments to monitor and remove some of these shifts, and obtain excellent unfolding as a result.

References

[1]   G. Knoll, *Radiation Detection and Measurement*, 3rd ed. 1997.

[2]   T. W. Crane and M. P. Baker, "Neutron Detectors," in *Passive Nondestructive Assay of Nuclear Materials*, no. 13, United States Nuclear Regulatory Commission, 1991, pp. 1–28.

[3]   H. Klein and F. D. Brooks, "Scintillation Detectors for Fast Neutrons," presented at the International Workshop on Fast Neutron Detectors, University of Cape Town, South Africa, 2006, pp. 1–24.

[4]   M. Flaska and S. Pozzi, "Identification of shielded neutron sources with the liquid scintillator BC-501A using a digital pulse shape discrimination method," *Nuclear Instruments and Methods in Physics Research Section A: Accelerators, Spectrometers, Detectors and Associated Equipment*, vol. 577, no. 3, pp. 654–663, Jul. 2007.

[5]   D. L. Chichester, J. T. Johnson, and E. H. Seabury, "Fast-neutron spectrometry using a 3He ionization chamber and digital pulse shape analysis," *Applied Radiation and Isotopes*, vol. 70, no. 8, pp. 1457–1463, Aug. 2012.

[6]   K. Banerjee, T. K. Ghosh, S. Kundu, T. K. Rana, C. Bhattacharya, J. K. Meena, G. Mukherjee, P. Mali, D. Gupta, S. Mukhopadhyay, D. Pandit, S. R. Banerjee, S. Bhattacharya, T. Bandyopadhyay, and S. Chatterjee, "Variation of neutron detection characteristics with dimension of BC501A neutron detector," *Nuclear inst. and Methods in Physics Research, A*, vol. 608, no. 3, pp. 440–446, Sep. 2009.

[7]   J. Birks, *Theory and Practice of Scintillation Counting*. Pergemon Press.

[8]   H. Klein, "Neutron Spectrometry in Mixed Fields: NE213/BC501A Liquid Scintillation Spectrometers," *Radiation Protection and Dosimetry*, vol. 107, pp. 95–109, Dec. 2003.

[9]   A. Enqvist and I. Pázsit, "Calculation of the light pulse distributions induced by fast neutrons in organic scintillation detectors," *Nuclear Instruments and Methods in Physics Research Section A: Accelerators, Spectrometers, Detectors and Associated Equipment*, vol. 618, no. 1, pp. 266–274, Jun. 2010.

[10]   S. A. Pozzi, M. Flaska, A. Enqvist, and I. Pázsit, "Monte Carlo and analytical models of neutron detection with organic scintillation detectors," *Nuclear Instruments and Methods in Physics Research Section A: Accelerators, Spectrometers, Detectors and Associated Equipment*, vol. 582, no. 2, pp. 629–637, Nov. 2007.

[11]   L. Cartegni and S. Pozzi, "Determination of liquid scintillator response matrix for neutron spectrum unfolding," pp. 1–8, Jul. 2004.

[12]   S. A. Pozzi, S. D. Clarke, W. J. Walsh, E. C. Miller, J. L. Dolan, M. Flaska, B. M. Wieger, A. Enqvist, E. Padovani, J. K. Mattingly, D. L. Chichester, and P. Peerani, "MCNPX-PoliMi for nuclear nonproliferation applications," *Nuclear inst. and Methods in Physics Research, A*, vol. 694, no. C, pp. 119–125, Dec. 2012.

[13]   R. A. Winyard, J. E. Lutkin, and G. W. McBeth, "Pulse Shape Discrimination in Inorganic and Organic Scintillators. I," *Nuclear Instruments and Methods*, vol. 95, pp. 141–153, Jun. 1971.

[14]   M. I. Ojaruega, "Fast Neutron Measurements Using Deuterated Liquid Scintillators," 2009.

[15]   M. Ojaruega, F. D. Becchetti, A. N. Villano, H. Jiang, R. O. Torres-Isea, J. J. Kolata, R. J. Goldston, and C. C. Lawrence, "Evaluation of large deuterated scintillators for fast neutron detection (E=0.5–20MeV) using the D(d,n)3He, 13C(d,n) and 27Al(d,n) reactions," *Nuclear inst. and Methods in Physics Research, A*, vol. 652, no. 1, pp. 397–399, Aug. 2010.

[16]   F. D. Brooks, "Development of organic scintillators," *Nuclear inst. and Methods in Physics Research, A*, vol. 162, pp. 477–505, Jun. 1979.

[17]   S. Croft, J. M. Adams, D. S. Bond, N. P. Hawkes, and N. Watkins, "A measurement of the light output function of the deuterated liquid scintillator NE-230 to recoil deuterons with energies between 0.62 and 14.5 MeV *," *Nuclear Instruments and Methods in Physics Research A*, vol. 316, pp. 324–332, Jul. 1992.

[18]   N. Zaitseva, A. Glenn, L. Carman, R. Hatarik, S. Hamel, M. Faust, B. Schabes, N. Cherepy, and S. Payne, "Pulse Shape Discrimination in Impure and Mixed Single-Crystal Organic Scintillators," *IEEE Transactions on Nuclear Science*, vol. 58, no. 6, pp. 3411–3420, Dec. 2011.

[19]   S. A. Pozzi, M. M. Bourne, and S. D. Clarke, "Pulse-shape Discrimination in the Plastic Scintillator EJ-299-33," *Nuclear inst. and Methods in Physics Research, A*, vol. 723, no. C, pp. 19–23, Sep. 2013.

[20] D. Cester, G. Nebbia, L. Stevanato, F. Pino, and G. Viesti, "Experimental Tests of the New Plastic Scintillaotr with Pulse-shape Discrimination Capabilities EJ-299-33," *Nuclear inst. and Methods in Physics Research, A*, vol. 735, no. C, pp. 202–206, Jan. 2014.

[21] C. C. Lawrence, A. Enqvist, M. Flaska, S. A. Pozzi, and F. D. Becchetti, "Comparison of Spectrum-unfolding Performance of (EJ315_ and (EJ309) Liquid Scintillators on Measured Cf-252 Pulse-height Spectra," *Nuclear inst. and Methods in Physics Research, A*, vol. 729, no. C, pp. 924–929, Nov. 2013.

[22] L. Stevanato, D. Cester, G. Nebbia, and G. Viesti, "Neutron detection in a high gamma-ray background with EJ-301 and EJ-309 liquid scintillators," *Nuclear Instruments and Methods in Physics Research Section A: Accelerators, Spectrometers, Detectors and Associated Equipment*, vol. 690, pp. 96–101, Oct. 2012.

[23] N. P. Hawkes and G. C. Taylor, "Analysis of the Pulse-shape Mechanism in a Plastic Scintillator with Efficient Neutron/gamma Pulse-shape Discrimination," *Nuclear inst. and Methods in Physics Research, A*, vol. 729, no. C, pp. 522–526, Nov. 2013.

[24] S. Nyibule, E. Henry, W. U. Schröder, J. Tõke, L. Acosta, L. Auditore, G. Cardella, E. De Filippo, L. Francalanza, S. Gìani, T. Minniti, E. Morgana, E. V. Pagano, S. Pirrone, G. Politi, L. Quattrocchi, F. Rizzo, P. Russotto, A. Trifirò, and M. Trimarchi, "Radioluminescent Characteristics of the EJ 299-33 Plastic Scintillator," *Nuclear inst. and Methods in Physics Research, A*, vol. 728, no. C, pp. 36–39, Nov. 2013.

Chapter 3
Neutron Spectroscopy and
Spectrum Unfolding

The overarching difficulty of fast-neutron spectroscopy is due to the neutron's weakly-interacting nature. Interactions by which a neutron is stopped within a detecting medium - like neutron capture or n-p process - are of quite low cross section for fission-energy neutrons, leading to extremely low detection efficiencies on the order or 10^{-4} - 10^{-3} in detectors employing these processes. The cross-section is higher for elastic scattering on small nuclei, but these interactions are unconstrained in scattering angle, and thus in fractional energy transfer. Thus, neutron spectroscopy is generally either a low-efficiency or a statistical affair. Of course, TOF techniques - whereby neutrons are timed as they traverse some distance - are an exception to these generalizations, and it will be utilized them later to calculate reference spectra for comparison with unfolded trial spectra. But TOF is only available in specialized applications, and should be treated as a separate problem from that of single-detector spectroscopy [1]-[3].

Along with the difficulty of neutron spectroscopy, its historical uses provide an important bit of context for us here. In his review of neutron spectroscopy techniques, D.J. Thomas identifies four different categories of locations in which knowledge of present neutron spectra are important: laboratory settings, workplaces, near reactor cores, and at fusion facilities [3]. The requirements and constraints arising out of these four categories - along with the difficulties mentioned above - have guided and constrained the development of neutron-spectroscopic techniques over the years [3]. A few general comments can be made in this regard. Typically, when high-resolution information has been required, as in laboratory settings, TOF spectroscopy was possible. When TOF was not available, as in the work place or near a reactor core, lower-resolution spectrometry was sufficient for the dose estimates necessary to characterize radiation exposures to humans or reactor vessels, or to obtain information about plasma temperatures. Rarely has material characterization been at stake. In order to apply neutron spectroscopy for

treaty verification, we must bring it into this more demanding category. This will require a balance between high-efficiency neutron detection and detailed preservation of energy information. In this chapter, I'll describe the inverse problem of spectrum unfolding with organic scintillators, why it is difficult or ill-posed, what techniques are used to solve it, and what quality of results are typically expected.

3.1.1 Neutron spectrum unfolding as an inverse problem

Due to the complications in their pulse-height response outlined in Chapter 2, PHS $n(L)$ from organic scintillators cannot readily be visually interpreted. Instead, the incident spectra $\phi(E_n)$ must be "unfolded" from $n(L)$, i.e. the integral relation given by Eq. 2.4 must be solved for the source term $\phi(E_n)$. This is a classic form of inverse problem that arises in many areas of the physical sciences and it has been extensively studied:

$$b(s) = \int A(s,t)\, x(t)\, dt \,. \tag{3.1}$$

The descriptor "inverse" refers to the direction along causality traversed by the analyst. In the easier "forward" problem the source term $x(t)$ - or "cause" - is propagated through a causal operator $A(s,t)$ to calculate the predicted observable "effect" $b(s)$. Forward problems often have unique and straightforward solutions. In the "inverse" problem, the posterior "effect" b is observed, and an estimated "cause" is sought by "inverting" the causal operator A. But in many physical systems of interest, multiple and disparate causes can lead to very similar, or even the same, effects. The solutions x are "unstable" in these cases - either non-unique or sensitively dependent on the inevitable fluctuations attendant to any observable b - and the analyst must resort to inductive techniques, and/or utilize a priori information external to the data b to further constrain the solution.

The degree of instability in x is related to the "flatness" of the matrix $A(s,t)$ - sharp distinguishable features in A help to constrain the solution for a given data set b [4], [5]. This loose concept of "flatness" or "featurelessness" is analogous to the *condition* of a discrete matrix, and indeed adopts this more concrete definition when the continuous Eq. 3.1 is discretized

$$Ax = b. \tag{3.2}$$

Strictly speaking, the *condition number* of the a discrete A is defined as the ratio between the largest and smallest singular values of A

$$cond(A) = \frac{\sigma_{max}}{\sigma_{min}} \tag{3.3}$$

where the singular values σ_i are the square roots of the eigenvalues of $A^{\dagger}A$. Higher condition number is associated with greater instability of inverse solutions [6]. However, even though our spectrum-unfolding problem will be discretized in practice, Eq. 3.3 will be of little use to us because the condition of our matrices will be so horrible as to exhaust the dynamic range of 64-bit numerical calculation. Instead, we will note that the solution instability is related to the rate of decrease of the descending singular values [7]. When the word "condition" is used henceforth, it will refer more qualitatively to the general instability of solutions due to the "flatness" of A, and in Chapter 7 I will employ a framework drawn from Ref. [7] to evaluate matrix condition by plotting the descending eigenvalues of $A^{\dagger}A$.

In this chapter, we want to develop an intuition about the instability of solutions x, how that instability is related to the structure of a given matrix A, and how it is commonly addressed in the context of spectrum unfolding. The labels A, x, and b will be used to refer in general to problems of the form of Eq. 3.1, while R, ϕ, and n will indicate the particular problem of neutron spectrum unfolding. Distinction between different vectors in the same space - for instance, between a candidate solution $x^{(k)}$ and the true unknown solution $x^{(0)}$ - will be indicated with superscripts, and components of a vector will be indexed with subscripts. Matrices are capitalized and vectors are written in lower case.

The methods used for spectrum unfolding arise out of two different conceptual frameworks, and they will be outlined in the latter half of this chapter. For now, I will make some preliminary comments. The instability in x is typically addressed by a compromise between agreement with observed data b, and implementation of some a-priori information. Agreement with data is associated with a residual vector $r^{(k)}$

$$r^{(k)} = b^{obs} - b^{(k)} \qquad\qquad (3.4)$$

which represents the difference between the vector $b^{(k)}$ in data space related to the kth candidate solution $x^{(k)}$ by Eq. 3.1, and the observed data b^{obs}. As such, an "optimal" solution $x^{(opt)}$ might be sought which extremizes some functional

$$\chi^{(k)} = f_{data}\left(r^{(k)}\right) + \lambda f_{a\,priori}\left(x^{(k)}\right) \qquad\qquad (3.5)$$

where f_{data} and $f_{a\,priori}$ are functionals representing the data and a priori constraints respectively. The relative priorities of the two constraints are weighted by a "regularization" parameter λ. The a priori constraint may be some shape requirement, like smoothness, or distance from some expected solution [5], [6], [8]. Once the functional is defined, it can be extremized analytically by the Lagrange method [9], or numerically with some iterative method.

It should also be borne in mind that, in practice, Eq. 3.1 is discretized to give Eq. 3.2. Thus, $A(s,t)$ is converted into a m-by-p matrix A, where m corresponds to the number of data elements in b, and p corresponds the number of independent parameters in the solution vector x. The discretization scheme as often a choice of the practitioner, and one would like to obtain as much information about the source x as possible, i.e. discretize it into more and smaller bins or elements. However, if the solutions are to have any hope of being unique, we will need $m \geq p$. Thus a desire for more solution parameters ultimately drives finer discretization in the data space as well, so that $A(s,t)$ is carved up into more and finer rows. We will see that excessively fine discretization structures result in the instability of the solutions $x^{(opt)}$.

3.1.2 Instability of solutions

A more candid expression of Eq. 3.1 would incorporate the inevitable perturbations $\delta b^{(exp)}$ associated with any practical measurement. Furthermore, the typical solution technique involves evaluating an array of candidate solutions $x^{(k)}$ using the corresponding residual $r^{(k)}$ in data space. We will later distinguish between several species of vector in both spaces, but now let us consider a general perturbation on an "ideal" vector in both spaces:

$$b^{(0)}(s) + \eta(s) = \int A(s,t) \, (x^{(0)}(t) + \varepsilon(t)) \, dt. \tag{3.6}$$

We could call $x^{(0)}$ the true but unknown source (neutron spectrum) and $b^{(0)}$ the "ideal" dataset that would result by propagating $x^{(0)}$ (if it were known) forward through Eq. 3.1; η is a perturbation on $b^{(0)}$; and ε is the perturbation in solution space corresponding to η. We are interested in the relation between the corresponding perturbations ε and η. By superposition:

$$\eta(s) = \int A(s,t) \, \varepsilon(t) \, dt. \tag{3.7}$$

It is often stated that the η is "amplified" by $\int dt A(s,t)$. But this implies an amplitude correlation such that standard error propagation rules could be used, which is misleading. Instead, we see an inverse relation between the amplitudes of η and the *frequency* (w.r.t. dependent variable t) of structure in ε. To see this, consider a sinusoidal component of ε

$$\varepsilon_l = C_l \sin(\omega_l t) \tag{3.8}$$

giving for the corresponding component η_j

$$\eta_l = \int A(s,t) \, (C_l \sin(\omega_l t)) dt. \tag{3.9}$$

It is well known that for a given (square-integrable, continuous) A, η_j vanishes as ω_j increases to infinity

$$\lim_{\omega_l \to \infty}(n_l) = 0. \tag{3.10}$$

Thus, high frequency components ε_j in the solution space are associated with only small components η_j in the observed space. Taken the other way around, this means that very small perturbations in the observable space correspond with high-frequency perturbations of almost arbitrary amplitude in the solution space. We will see later that error in our unfolded solutions often takes oscillatory form.

We can also see that the rate at which the limit expressed in Eq. 3.10 is approached is governed by the "flatness", or the scale of distinguishable features, in R. Regions of high slope -

with respect to t - in the rows of $A(t)$ tend to slow the approach. Looking at the example matrix presented in Fig. 3.6 of the previous chapter, we see that we are in some trouble since it is quite flat and featureless.

We can make a similar argument in the discrete case. The "null" space of a matrix contains all the vectors $x^{(null)}$ for which

$$Ax^{(null)} = 0. \tag{3.11}$$

A non-zero null space for A means that solutions to $Ax = b$ are non-unique - given any solution $x^{(0)}$, we can add any vector from within the $x^{(null)}$ to $x^{(0)}$ and still get a viable solution. This corresponds to an m-by-p A for which $m < p$, or a system of equations bearing more unknowns than independent equations. In practice we can discretize $A(s,t)$ as we like, such that $m \geq p$. But for an $A(s,t)$ of a given structure or "flatness", if we make m large such that the data bin width Δs is much smaller than the scale of structure in $A(s,t)$, adjacent rows of the discretized A become similar to each other and lose their independence. This leads to a problematic region in the solution space $x^{(prob)}$ for which the corresponding observable vectors are small:

$$Ax^{(prob)} = b^{(small)}. \tag{3.12}$$

If $b^{(small)}$ is smaller than the uncertainty δb in the observable $b^{(obs)}$, then components within $x^{(prob)}$ are invisible to the measurement[x].

Now if we are faced with an inverse problem like neutron spectrum unfolding, we naturally want to estimate the source term $x(t)$ with as much fidelity as possible, and thus to discretize it into as many elements as possible (i.e. to make Δt small). This, in turn, compels us to discretize the observable into a large number $m \geq p$ of elements (i.e. to make Δs small). This is limited by the "flatness" of $A(s,t)$. If we make m and p too large, adjacent rows of A lose their independence, and the solutions x acquire prominent oscillatory error components within the problematic space $x^{(prob)}$. So our "success" at this type of inverse problem can be roughly

_____

[x] Here, $b^{(prob)}$ and $x^{(prob)}$ are analogous to the perturbations η and ε (respectively) discussed above for the continuous treatment.

expressed as the dimension *m* for which a solution *x* can be stably obtained. In the context of spectrum unfolding, larger *m* means more narrowly-spaced energy bins.

3.2 Methods for solving the unfolding problem

While the development of unfolding techniques loosely mirrors that of techniques for solving the general Eq. 3.1, some comments here refer to the specific literature on spectrum unfolding. With few exceptions, most literature on spectrum unfolding takes the response matrix *R*, and its poor condition, as a given, and focuses on methods for constraining the solution. While a major theme of this dissertation is the pursuit of improved matrix condition, here we will set that aside and outline some general strategies used for solving the unfolding problem with a given ill-conditioned *R*. As described above, *R* is discretized into *m* pulse-height groups and *p* energy groups, and it is natural that most research activity on spectrum unfolding takes place at the margin where *m* and *p* are large enough for instability in ϕ to onset. So the general task is to choose amongst an array of potentially very different candidate spectra $\phi^{(k)}$ which are roughly equally compatible with the $n^{(obs)}$. Approaches to this problem arise out of two different conceptual frameworks. The older framework treats spectrum unfolding as a matrix inversion problem in need of some perturbation to stabilize the solution, often called regularization. The second, more modern framework treats it as an inference problem. These two categories are outlined in the following sections.

3.2.1 Regularized matrix inversion

The earlier attempts at spectrum unfolding took $R\phi = n$ at face value, treating it as a matrix inversion problem. Inversion of large matrices is often carried out by minimizing some measure of "fit" to data, such as the 2-norm of the residual vector $r^{(k)}$

$$\chi^2 = \|r\|^2 = \sum_i \left[n_i^{obs} - n_i^{(k)} \right] = \sum_i \left[n_i^{obs} - \sum_j R_{ij}\phi_j^{(k)} \right]^2 . \tag{3.13}$$

However, the solution that optimally fits the data is seldom useful with an ill-conditioned R, so some a priori constraint is added to the extremized functional to implement knowledge about the expected solution

$$\chi^2_{reg} = \left\| r \right\|^2 + \lambda f(\phi).$$

(3.14)

This is referred to as regularization. The simplest option for f is the 2-norm of the solution itself

$$\chi^2_{reg} = \left\| r \right\|^2 + \lambda \left\| x \right\|^2.$$

(3.15)

Constraining the length of the solution vector has the effect of removing high-frequency features, and this is reasonable given the nature of the instability described above. While there are other options for f, such as distance from some expected spectrum, we can get a general idea of how regularization works - and some good spectrum unfolding results - by looking at the simple choice in expressed Eq. 3.15. The Eq. 3.15 is minimized by the solution to the equation

$$(R^\dagger R + \lambda I)\phi = R^\dagger n$$

(3.16)

which can be solved using standard techniques like the conjugate-gradient method. Limiting behaviors of the solution ϕ with respect to the regularization parameter λ are fairly straight forward. With very small λ, the solution approaches the un-regularized solution, and is dominated by the oscillatory error component. With very large λ, Eq. 3.16 approaches

$$\lambda I \phi = R^\dagger n$$

(3.17)

so that the shape of the "over-regularized" solution approaches that of $R^\dagger n$, which is not a useful representation of the spectrum ϕ. This behavior is often visualized in the form of an L-curve, so named because of its prominent L-shaped feature. A standard L-curve is a log-log plot of the solution 2-norm versus the residual 2-norm, as is represented in Fig. 3.1. For small λ, the residual norm is small, but the norm of the solution is large because it is dominated by large erroneous oscillations. As λ is increased, the oscillations are damped and the solution norm is decreased.

But as the solution begins to approach $R^\dagger n$, disagreement with the data n is increased, resulting in a larger residual norm. This results in the *L*-shaped feature in the *L*-curve, and a good compromise is achieved by choosing a λ corresponding to the elbow of the curve.
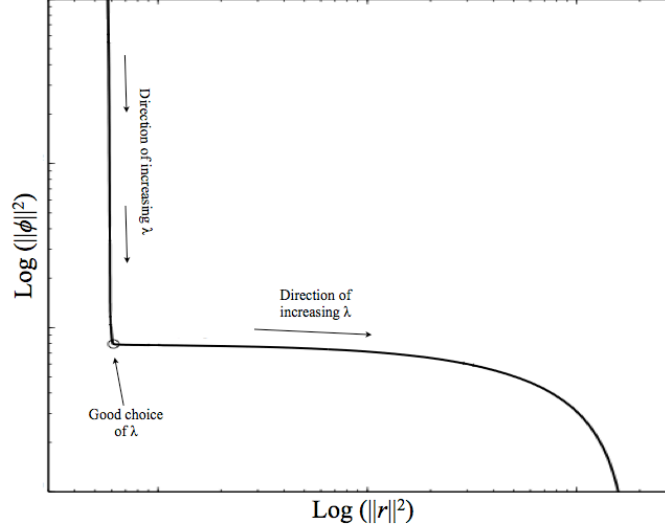
FIG. 3.1. Illustration of the *L*-curve, a visualization of the compromise made in regularized matrix inversion between agreement with data and adherence to some a prior constraint, like solution "smoothness".

One of the earliest unfolding codes developed - FERDOR - used a variant of regularized matrix inversion [7], [10]. A more developed version of FERDOR, called FORIST, is considered representative of the state of the art in this category, and often provides a standard to which other unfolding algorithms are compared [11]. However, it is not clear how to estimate uncertainty in the solutions using these codes [12]. Also, many consider justification for regularization techniques to be ad hoc: since the matrix in question $R^\dagger R$ is not invertible, some clever variant like $R^\dagger R + \lambda I$ is substituted in order to impose smoothness, and it is hoped that the smoothed solution approximates the correct solution [13]. These concerns led to the development of an alternative framework for solving inverse problems which draws from information theory.

3.2.2 Inference formalisms

It seems quite natural to treat inverse problems as problems of inference, especially in the context of spectrum unfolding, where the response matrix R represents a probabilistic coupling

between causes and effects. However, this approach did not become widely used until the mid 1980s and early 90s, after a somewhat supercilious E.T. Jaynes presented a sort of manifesto on inverse problems titled *Prior Information and Ambiguity in Inverse Problems*. In this wonderfully snide document, Jaynes argued that an ill-advised insistence on the *appearance* of deduction had led mathematicians to replace real ill-posed problems with "ad hoc" approximates, with little rational justification. Instead, he suggests that inverse problems should be treated as the inference challenges they are, and approached with techniques from probability and information theories.

In the spectrum unfolding literature, this philosophy is manifested in two types of algorithm: one relying on maximum likelihood estimation, and one which maximizes some notion of entropy. These principles allow the calculation of a probability distribution over possible solutions, and thus provide a framework for uncertainty estimation. Modern unfolding-code packages that employ these techniques include MAXED, UNFANA and HEPRO [7], [12], [14], [15]. I will briefly review them here.

Maximum likelihood estimation is based on the concept of Bayesian inference, and can be implemented in a number of ways. As an example, we can begin with the Poisson nature of counting statistics. From the forward problem, we know that the mean number of counts detected in the ith pulse-height group should be equal to

$$\bar{n}_i = \sum_j R_{ij}\phi_j \tag{3.18}$$

and the observed counts for a given measurement $n_i^{(obs)}$ are drawn from a Poisson distribution

$$P(n_i^{(obs)}) = \frac{\bar{n}_i^{n_i^{(obs)}} \exp(-\bar{n}_i)}{n_i^{(obs)}!}. \tag{3.19}$$

Plugging Eq. 3.18 into Eq. 3.19 gives

$$P(n_i^{(obs)}) = \frac{(\sum_j R_{ij}\phi_j)^{n_i^{(obs)}} \exp(-\sum_j R_{ij}\phi_j)}{n_i^{(obs)}!} \qquad (3.20)$$

as the probability of observing $n_i^{(obs)}$ in the ith pulse-height bin. The probability of observing a particular PHS $n^{(obs)}$ is given by the product over i

$$P(n_i^{(obs)}) = \prod_i \frac{(\sum_j R_{ij}\phi_j)^{n_i^{(obs)}} \exp(-\sum_j R_{ij}\phi_j)}{n_i^{(obs)}!} \qquad (3.21)$$

Now the question is asked, given an observed PHS $n^{(obs)}$: what is the neutron spectrum ϕ which would have made $n^{(obs)}$ *most probable*? Along these lines, Eq. 3.21 is maximized by setting the derivative of its logarithm equal to zero

$$\frac{d}{d\phi_j}\left[\ln(P(n_i^{(obs)}))\right] = 0 \qquad (3.22)$$

to derive a system of "likelihood equations" which are solved for the fluence values ϕ_j [15], [16].

With the maximum-entropy method, a probability over solutions $P(\phi)$ is sought, and an entropy is defined as

$$S = -\int P(\phi)\ln(P(\phi))d\phi \qquad (3.23)$$

with the form of $P(\phi)$ typically chosen as

$$P(\phi) = C\exp\left[-\frac{\beta}{2}\chi^2(\phi)\right] \qquad (3.24)$$

and χ^2 defined as the squared 2-norm of the residual vector. The "temperature" factor β is determined by enforcing that the expectation value of χ^2 should be equal to the number of degrees of freedom in the measurement, namely the number l of pulse-height groups in the PHS [7], [17]

$$\langle \chi^2 \rangle = l. \qquad (3.25)$$

The entropy represented in Eq. 3.23 is then maximized by the Lagrange method [9].

3.3 Typical unfolding results

One of the earliest and most comprehensive studies of spectrum unfolding with liquid scintillators was associated with the development of the FERDOR unfolding code. In 1969, Burrus and Verbinski published a pair of companion articles on their developments. The first described a calculation of the response matrix of a standard NE213 liquid scintillator, using a combination of measurement, simulation, and interpolation. Mono-energetic neutron sources were produced by the reactions $T(p,n)^3He$, $D(d,n)^3He$, and $T(d,n)^4He$ in thin reaction targets[xi], so that PHS could be measured with fourteen different energies ranging from $0.2 < E_n < 22$ MeV. Other energies were simulated, and an interpolation technique was used to fill in the spaces of the matrix between the measured and simulated energies [18]. The second article of the series described the unfolding method used by the FERDOR code, and spectrum unfolding results from PHS measured from a Po-Be neutron source. This study was quite holistic, in that details of detector operation such as pulse-shape analysis and the data-acquisition electronics were described in detail. A more thorough validation of the matrix and the unfolding code was carried out shortly thereafter by Straker et. al [19], which compared unfolded spectra with reference spectra obtained simultaneously using TOF. An example is shown in Fig. 3.2, where a carbon attenuator is used to introduce sharp features to the measured spectrum. The shaded region represents the "confidence bounds" estimated by the FERDOR code. It should be noted, however, that these confidence bounds only account for uncertainty associated with the non-uniqueness of the solution, and do not represent a comprehensive uncertainty analysis. It is clear that the unfolding technique cannot resolve the finer structures of the spectrum. Nevertheless, these results were (appropriately) deemed adequate for many dosimetry applications, and this collection of articles laid much of the groundwork for future spectrum unfolding studies.

[xi] The word thin here can refer to "optically" thin, as the $D(d,n)^3He$ reaction was produced in a gas target.
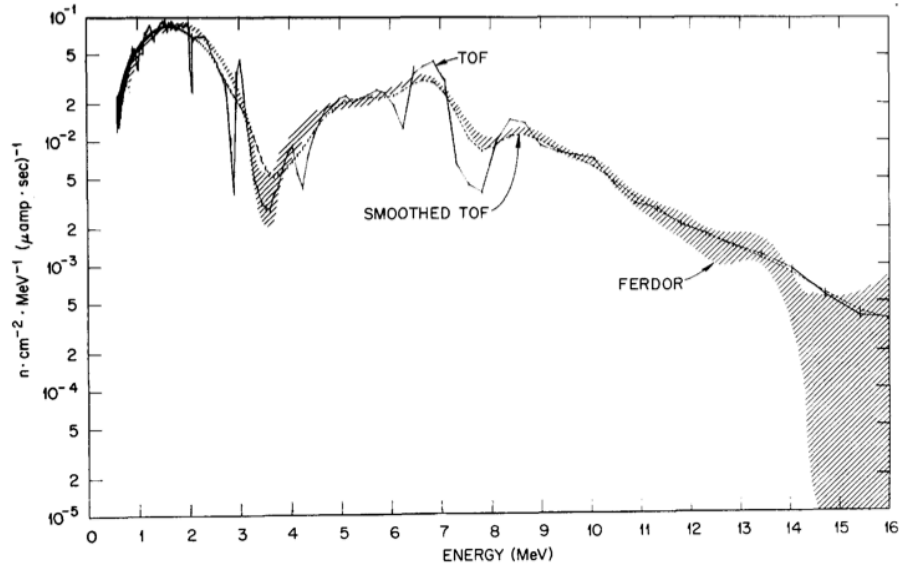
FIG. 3.2. Early unfolding results reported by Straker et al. [19], using the FERDOR unfolding code [10]. Time-of-flight-calculated reference is a shown for comparison (courtesy of Elsevier).

Later developments in spectrum unfolding were partly driven by advances in computing technologies, and this had two important influences. First, the computational cost of iterative unfolding methods was dramatically reduced, so that many new techniques became practical. Second, Monte Carlo methods for simulating detector response became much more widely available, leading to a shift away from direct measurement of both response matrices and PHS for unfolding trials. Taken together, these effects culminated in a general focus on developing, improving, validating and comparing different spectrum-unfolding algorithms. While these developments have produced a great variety of unfolding codes, many of which rest on a firmer intellectual foundation than the earlier codes like FERDOR, they have come at the cost of a focus on the detection system itself as it pertains to spectrum unfolding. Many detailed studies of spectrum unfolding describe the algorithms, and validate them on artificial numerical data [15], [20]-[23], or with simulated PHS [24] [25]. Response matrices are almost always calculated with Monte Carlo simulation. Evaluations of spectrum unfolding with actual measurement are scarce, and when they appear they are usually with neutron spectra that are not very well characterized, like alpha-n sources. In one striking example, Koohi-Fayegh et al. evaluate a series of spectrum unfolding codes by comparing how well they re-produce the results of FORIST, rather than a

known or TOF-calculated reference [11]. Meanwhile, detailed comparison between different types of scintillators is rare.
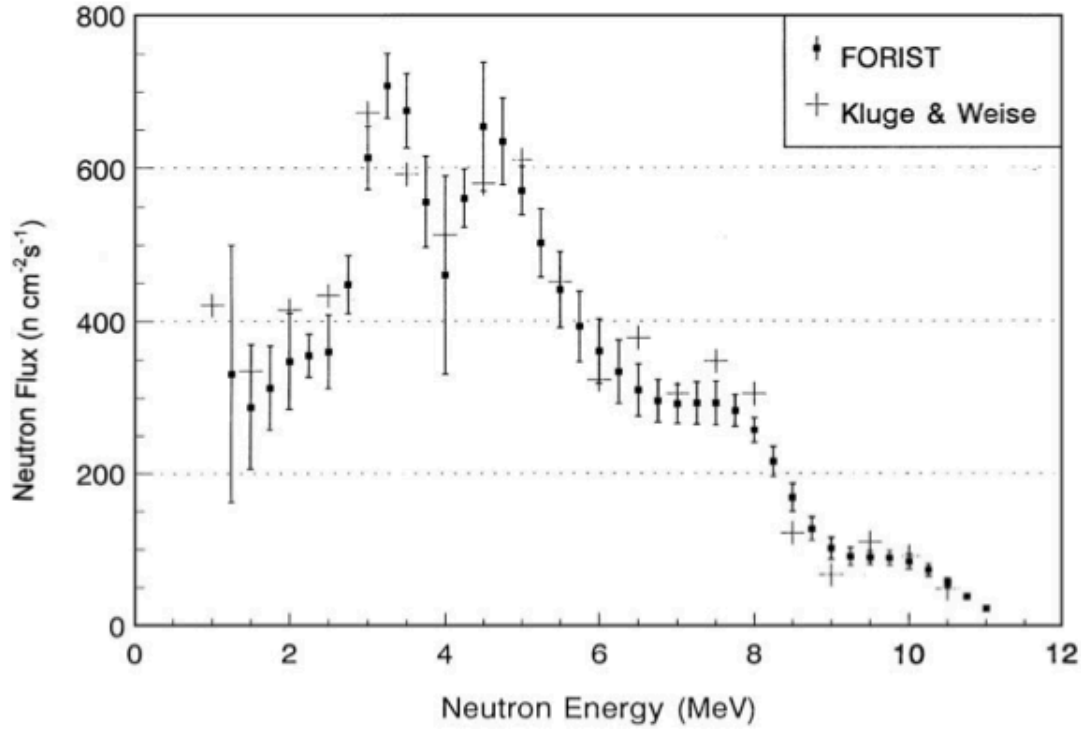
FIG. 3.3. Representative unfolding results in the reported literature, obtained with the FORIST unfolding code. The solution space is discretized into 200-keV-wide energy groups. The spectrum measured is from an Am-Be *α-n* source. A common reference for Am-Be neutron spectrum from Kluge et al. is shown for comparison [11] (courtesy of Elsevier).

Amongst the unfolding results from measured PHS that are reported in the literature, the best results are with energy groups that are 200-300 keV wide. This is exemplified in the FOREST result used by Koohi-Fayegh as an unfolding standard, reproduced here in Fig. 3.3 [11]. This is likely inadequate for treaty-verification applications, for which we would like stable, reliable solutions with energy groups that are 100 keV wide or finer [26].

3.4 Venues for improving spectrum unfolding

At the end of Chapter 2, I suggested some ways in which unfolding performance could be improved by altering detector performance. We can divide these into two categories:

1) Improvements in the condition of detector response matrix;

2) Improvements in the stability and accuracy of representation of detector response.

The first category affects the extent to which measurement errors δn in the observed PHS $n^{(obs)}$ are "amplified" to produce large oscillatory errors $\delta\phi$ in the unfolded spectra. Improvements in the condition of R may help to dampen this amplification. The second category corresponds to ways in which δn are generated in the first place. Tables 1 and 2 list examples in these respective categories. The lists are not intended to be exhaustive.

TAB. 3.1. Attributes of detector pulse-height response that affect the condition of response matrix R.

Attribute	Effect on matrix	Proposed improvement
Scattering kinematics	Broad features in matrix	Deuterated detectors to employ backscatter-peaked n-d scattering in place of isotropic n-p scattering
Pulse-height resolution	Sharpness of features in matrix	Some organic crystals can be optimized for superior energy resolution
Discretization scheme	Mutual independence of matrix rows;	Conform pulse-height bin widths to the scale of matrix features

TAB. 3.2. Sources of perturbation in measured pulse-height spectra that contribute to error in unfolded spectra.

Source of perturbation	Likely improvement for field
Poisson variance in PHS	N/A
Inaccuracies in response matrix	Detector with directly-measured response matrix
Shifts in PMT gain	Direct optical input to scintillator cell for real-time calibration during measurement
Shifts in PSD discrimination threshold	Elgen proprietary additive to improve PSD performance [27]; systematic placement of PSD discrimination curve [28].

Consider each attribute in Tab. 1 in the context of the earlier arguments about the mutual independence of adjacent columns. If the matrix R is discretized with bin widths that are much smaller than the scale of differentiable features in the continuous R, then the adjacent columns lose their independence. It is easy to imagine that more definable features in R, like the back-

scatter structure associated with *n-d* scattering, would preserve the independence of adjacent columns for smaller bin widths than if the matrix were simply flat. And since poorer resolution tends to blur any features that the kinematics produce, it will also compromise column independence. Finally, since the diminishing returns of finer binning structures is governed by the separation of matrix features, and since limited counts must be divided amongst pulse-height bins, the scale of this separation should be taken into account when deciding upon a discretization scheme. Further, the scale of features is variant across the pulse-height scale, due mainly to the nonlinear light-output relation described in Chapter 2, such that evenly space binning across the pulse-height scale will not be ideal. I will look at these attributes further in Chapters 7-9.

Amongst the performance attributes listed in Tab. 2, a further distinction can be made. Poisson variance in the number of detected pulses n_i falling in the *i*th pulse-height bin is unavoidable, and inversely related to the the duration of measurement, which is costly. Thus, for a given measurement time, Poisson variance represents a hard limit on how well the perturbation δn can be constrained. In principle, the other attributes can be improved upon. I will improve upon them in here using TOF techniques. Response matrices R_{model} will be measured using TOF to minimize uncertainty in their accuracy. Trial measurements will be performed using the same TOF setup, providing reliable reference spectra for evaluating the unfolded spectra. But this will yield a more profound advantage: for any trial measurement performed, a response matrix R_{trial} can be constructed from the associated TOF data, the same way R_{model} was calculated from its associated TOF data. In principle, if no shifts in detector performance have occurred, the columns of R_{trial} should look identical to those of R_{model}. This will allow the diagnosis and removal of any shifts in PMT gain or PSD performance that occur. The results shown in Chapter 8 are very good in part because these shifts were removed.

Now, clearly TOF information is not available in the field, otherwise we would not be looking at PHS or unfolding at all. But the shifts in performance that I remove with TOF can easily be guarded against in the field using technologies and materials that are currently available. PSD can be dramatically improved using certain proprietary additives, or with crystal

scintillators [27], [28]. Shifts in gain can be eliminated using automated calibration systems that adjust PMT gain in real time. While these features were not part of the measurement system used here, they are realistic improvements that could be made to a fieldable system.

References

[1]   F. D. Brooks and H. Klein, "Neutron Spectrometry - Historical Review and Present Status," *Nuclear Instruments and Methods in Physics Research A*, vol. 476, pp. 1–11, Dec. 2001.

[2]   H. Klein, "Neutron Spectrometry in Mixed Fields: NE213/BC501A Liquid Scintillation Spectrometers," *Radiation Protection and Dosimetry*, vol. 107, pp. 95–109, Dec. 2003.

[3]   D. J. Thomas, "Neutron spectrometry," *Radiation Measurements*, vol. 45, no. 10, pp. 1178–1185, Dec. 2010.

[4]   R. Allen, W. R. Boland, V. Faber, and G. M. Wing, "Singular Values and Condition Number of Galerkin Matrices Arising from Linear Integral Equations of the First Kind," *Journal of Mathematical Analysis and Applications*, pp. 1–27, Nov. 1985.

[5]   D. Phillips, "A Technique for the Numerical Solution of Certain Intergral Equations of the First Kind," pp. 1–14, Feb. 1961.

[6]   P. C. Hansen, "MATLAB Regularization Toolbox," *Numerical Algorithms*, vol. 46, pp. 189–194, Mar. 2007.

[7]   M. Matzke, "Unfolding Procedures," *Radiation Protection and Dosimetry*, vol. 107, no. 1, pp. 155–174, Dec. 2003.

[8]   M. Freitag, "Tikhonov Regularisation for (Large) Inverse Problems," pp. 1–157, Aug. 2011.

[9]   H. GoldsteinPoole, *Classical Mechanics*, 3rd ed. Pearson, 2002.

[10]   W. R. Burrus and V. V. Verbinski, "Fast-neutron Spectroscopy with Thick Organic Scintillators," *Nuclear Instruments and Methods*, vol. 67, pp. 181–196, Jun. 1969.

[11]   R. Koohi-Fayegh, S. Green, and M. C. Scott, "A Comparison of Neutron Spectrum Unfolding Codes Used with a Miniature NE213 Detector," *Nuclear Instruments and Methods in Physics Research A*, vol. 460, pp. 391–400, Mar. 2001.

[12]   M. Matzke, "Propagation of Uncertainties in Unfolding Proceedures," *Nuclear Instruments and Methods in Physics Research A*, vol. 476, pp. 230–241, Dec. 2002.

[13]   E. T. Jaynes, "Prior Information and Ambiguity in Inverse Problems," presented at the SIAM-AMS, 1984, vol. 14, pp. 151–166.

[14]   M. Matzke, "The HEPROW Program System," pp. 1–40, Jun. 2013.

[15]   S. Itoh, "A Fundamental Study of Neutron Spectra Unfolding Based on the Maximum Likelihood Method," *Nuclear Instruments and Methods in Physics Research A*, vol. 251, pp. 144–155, Jun. 1986.

[16]   B. Pehlivanovic, S. Avdic, P. Marinkovic, S. Pozzi, and M. Flaska, "Comparison of Unfolding Approaches for Monoenergetic and Continuous Fast-neutron Energy Spectra," Oct. 2011.

[17] J. Shore and R. Johnson, "Axiomatic Derivation of the Principle of Maximum Entropy and the Principle of Minimum Cross-entropy," *IEEE Transactions on Information Theory*, vol. 26, no. 1, pp. 1–12, Apr. 1980.

[18] V. V. Verbinski, W. R. Burrus, T. A. Love, W. Zobel, and N. W. Hill, "Calibration of an Organic Scintillator for Neutron Spectrometry," *Nuclear Instruments and Methods*, vol. 65, pp. 8–25, Jun. 1969.

[19] E. A. Straker, C. E. Burgart, T. A. Love, and R. M. Freestone, "Simultaneous Determination of Fast-neutron Spectra by Time-of-flight and Pulse-height Unfolding Techniques," *Nuclear Instruments and Methods*, vol. 97, pp. 275–282, Jun. 1971.

[20] V. B. Anykeyev, A. A. Spiridonov, and V. P. Zhigunov, "Comparative Investigation of Unfolding Methods," *Nuclear Instruments and Methods in Physics Research A*, vol. 303, pp. 350–369, Jul. 1991.

[21] T. Onoda and H. Sekimoto, "A Neutron Spectrometry Unfolding Code Based on Quadratic Programming," *Nuclear Instruments and Methods in Physics Research A*, vol. 272, pp. 844–846, Jun. 1988.

[22] K. Weise and M. Matzke, "A Prior Distributions from the Principle of Maximum Entropy for the Monte Carlo Unfolding of Particle Energy Spectra," *Nuclear Instruments and Methods in Physics Research A*, vol. 280, pp. 103–112, Jul. 1989.

[23] V. B. Anykeyev, A. A. Spiridonov, and V. P. Zhigunov, "Correcting Factors Method as an Unfolding Technique," *Nuclear Instruments and Methods in Physics Research A*, vol. 332, pp. 280–285, Jun. 1992.

[24] S. Avdic, S. Pozzi, and V. PROTOPOPESCU, "Detector response unfolding using artificial neural networks," *Nuclear Instruments and Methods in Physics Research Section A: Accelerators, Spectrometers, Detectors and Associated Equipment*, vol. 565, no. 2, pp. 742–752, Sep. 2006.

[25] H. Sekimoto, "An Unfolding Method Leading to a Positive Solution Only," *Nuclear Instruments and Methods in Physics Research*, vol. 228, pp. 129–132, Jul. 2002.

[26] R. C. Runkle, A. Bernstein, and P. E. Vanier, "Securing special nuclear material: Recent advances in neutron detection and their role in nonproliferation," *J. Appl. Phys.*, vol. 108, no. 11, p. 111101, 2010.

[27] C. C. Lawrence, A. Enqvist, M. Flaska, S. A. Pozzi, and F. D. Becchetti, "Comparison of Spectrum-unfolding Performance of (EJ315_ and (EJ309) Liquid Scintillators on Measured Cf-252 Pulse-height Spectra," *Nuclear inst. and Methods in Physics Research, A*, vol. 729, no. C, pp. 924–929, Nov. 2013.

[28] J. K. Polack, M. Flaska, A. P. Enqvist, and S. A. Pozzi, "A Computer-aided, Visual Charge-integration Pulse-discrimination Method for Organic Scintillators," presented at the Institute for Nuclear Materials Management, 54th Annual Meeting, Palm Desert CA, 2013.

Chapter 4
Accelerator-based Measurements for Full Characterization of Detector Pulse-height Response

I have argued that improvements in the amount of information derivable from scintillator PHS can be realized by focusing on the measurement system. The foundation of this will be a detailed characterization of detector response, which will include the response matrix R, light-output relation $L_{scint}(E_p)$, and pulse-height resolution $\delta L_{obs}/L_{scint}$. Accelerator-based measurements will provide the main tool for these characterizations, and they will be described in this chapter. I begin by describing different techniques for producing neutrons that are constrained in energy using medium-energy ion accelerators, and why continuous-spectrum neutrons sources with TOF gating are chosen for this study. Efforts to limit and characterize room-scattered neutrons are then discussed. Any neutrons that are scattered from objects in the room into our detector will disturb our constraints on the energy of detected neutrons. Finally, I describe the accelerator-produced neutron sources chosen for the measurements reported in this thesis.

4.1 Discrete-energy sources versus time-of-flight gating on continuous-spectrum sources

Medium-energy Van de Graaff accelerators, such as those currently in operation at Ohio University and the University of Notre Dame, are powerful tools for the characterization of neutron detectors. They can produce well-characterized neutron sources by bombarding various target materials with accelerated ions to elicit neutron-emitting nuclear reactions. For our purposes, the main task is to create a measurement situation in which neutrons are produced with different energies across our energy range of interest, and for which the energies of all detected neutrons are known. A common way to achieve this is to produce the reactions $T(p,n)^3$He, $D(d,n)^3$H or $T(d,n)^4$He in thin reaction targets. For a range of ion energies, these reactions

produce neutrons whose energies are uniquely related to the angle of outgoing neutrons[xii], so that a detector at a given angle would detect quasi-mono-energetic neutrons. The energy of the neutrons produced can be altered by changing the energy of incident ions, the detector location (angle with respect to the direction of incoming ions), or the choice of reaction target and incident ion. In one of the earliest studies of spectrum unfolding, Burrus and Verbinski characterized an NE213 scintillator in this way, measuring PHS for neutrons of 14 different energies ranging from $0.2 < E_n < 22$ MeV [1]. However, this method has many drawbacks. The energies available are limited, and each requires a different accelerator setting. Usually, only part of the detector response matrix is measured, and the rest is either interpolated or simulated using Monte Carlo simulations. Additionally, the energy binning is determined by the measurement itself, and cannot be conveniently altered afterwords.

A better alternative is to produce neutrons of a continuous spectrum that covers the energy range of interest, and use a TOF technique to determine the energy of each detected neutron. This allows the entire response matrix to be measured in a single measurement, without any change in the tuning of the accelerator[xiii]. Since the entire energy range is measured, no simulations are required for interpolation, except to produce the efficiency curve used to normalize the response matrix. Also, since neutron energies are binned after the measurement, the discretization structure can be altered at will without performing additional measurements. This will be very important since the discretization structure is a venue on which we hope to improve unfolding results.

Continuous spectra can be produced by choosing a reaction from which neutrons of multiple energies are produced[xiv], and generating the reactions in a thick target in which the incident ions are stopped, so that the energetic structure of the reaction is smeared out. The width or smearing of features in the neutron energy spectra is in part determined by the variation in penetration of the incident ions into the target. In a "thin" target, most incident ions pass through

---

[xii] Only the ground state of the product nucleus is populated.

[xiii] With limited access to accelerator facilities, minimization of tuning time is extremely important.

[xiv] Multiple excited states of the product nucleus are populated.

the target without reacting, and the ions that do react only lose a small part of their incident energy via Coulomb interaction prior to reacting with a target nuclei. In a "thick" target, all incident ions come to a halt, and react at varying positions along their slowing-down paths, so that the ion energy prior to reaction is variant. This smears out the energy structure of neutrons produced in the reaction. Suitable reactions for this include $^{11}B(d,n)$ [2] and $^{27}Al(d,n)$ [3]. For deuteron energies $5 < E_d < 8$ MeV, these reactions produce neutrons which continuously cover our energy range of interest when produced in thick targets. We have used $^{11}B(d,n)$ with $E_d = 5.5$ MeV for our measurements, and the neutron spectrum from this reaction is discussed in Section 4.2 of this chapter.

A TOF technique is implemented as follows. An alternating electric field of frequency f_{bunch} is produced longitudinally along the ion beam at locations upstream from the target. This alternatingly accelerates and decelerates adjacent lengths of beam such that they come together in "bunches" at some location down stream. The amplitude of the bunching RF field is tuned such that the bunch width is minimized at the target location. This produces a series of periodic pulses of ions incident on the target location[xv], with the duration of each pulse as low as 1ns. For each pulse, there is an associated timing signal at t_{start} to mark the time of reaction in the target. The neutron detector is set some distance d_{TOF} from the target location, and the bunching frequency f_{bunch} is set so the period between ion pulses τ_{bunch} on the target is larger than the time required for the slowest neutrons of interest to traverse the distance d_{TOF}. For each detected pulse in the detector, a constant-fraction discriminator marks the time of detection t_{stop}, and the difference $\Delta t_{TOF} = t_{stop} - t_{start}$ is tabulated.

Figure 4.1 shows a histogram of Δt_{TOF} for one of our TOF measurements ($^{11}B(d,n)$ with $E_d = 5.5$ MeV). The reaction produces both neutrons and gamma-rays. The tall and narrow peak at around $\Delta t_{TOF} = 33$ ns corresponds to gamma rays, while the broad distribution between $0.2 < \Delta t_{TOF} < 1.2$ μs corresponds to the continuous spectrum of neutrons. The relation between the start

---

[xv] Strictly speaking, more steps are required after "bunching". Since bunching is imperfect, there will still be ions present in the space between bunches at the target location. These are reduced with an additional alternating electric field transverse to the beam direction, called the "sweeper". In addition, the bunching frequency f_{bunch} is typically limited to a pre-defined value, like 1/100ns, and the frequency of observed pulses at the target location is reduced by factors of two by removing some of the pulses with a "beam selector". Thus, final pulse periods at the target location of $(100ns)*2^{n-1}$ are possible.

signal t_{start} and the actual time at which an incident bunch of ions reaches the target is constant, and can be deduced from the location of the gamma-ray peak (where $v_\gamma = c$) and corrected for. The flat distribution over negative regions along the Δt_{TOF} axis can be attributed to a constant random gamma-ray background, and used to characterize and remove that background.
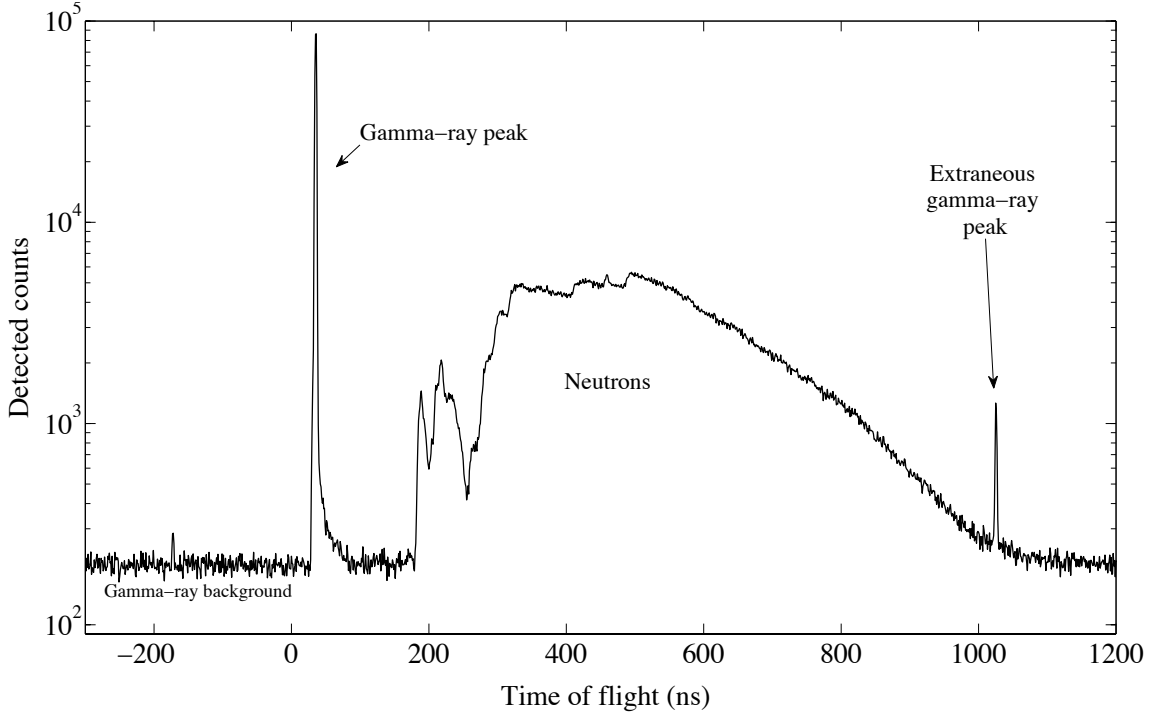
FIG. 4.1. Time-of-flight plot for neutrons produced via the reaction $^{11}B(d,n)$ in a thick target, with deuteron energy E_d = 5.5 MeV, measured with an EJ309 detector placed at d_{TOF} = 10.84 m from the target. Deuterons were accelerated using the 10-MV tandem Van de Graaff accelerator facility at the University of Notre Dame Nuclear Structure Laboratory (UND-NSL). The extraneous gamma-ray peak was attributed to collisions of deuterons on tungsten collimator slits upstream from the target, from which no neutrons are expected.

Since the Δt_{TOF} can be known for virtually all detected neutrons, it can be used to determine the energy of detected neutrons as they reach the detector. In order to construct a response matrix, detected neutrons can be binned via Δt_{TOF} into any desired energy-bin structure, and further binned into any desired pulse-height-bin structure (see Chapter 6). Structures in the response matrix can in turn be used to calculate light-output data $L_{scint}(E_p)$ and pulse-height resolution $\delta L_{obs}/L_{scint}$ (see Chapter 5). Also, since Δt_{TOF} provides an alternative means of n-γ discrimination, independent of PSD, it can be used to evaluate PSD performance. Finally, any

normalized TOF-gated pulse-height spectrum - i.e. any "column" of R - should look the same for multiple measurements, even if the incident spectra prior to gating is altered between measurements. This can be used to track changes in the pulse-height response of a detector over time due PMT-gain shifts or changes in temperature. These attributes make TOF measurements with continuous-spectrum neutrons an optimal technique to characterize our detectors for spectrum unfolding.
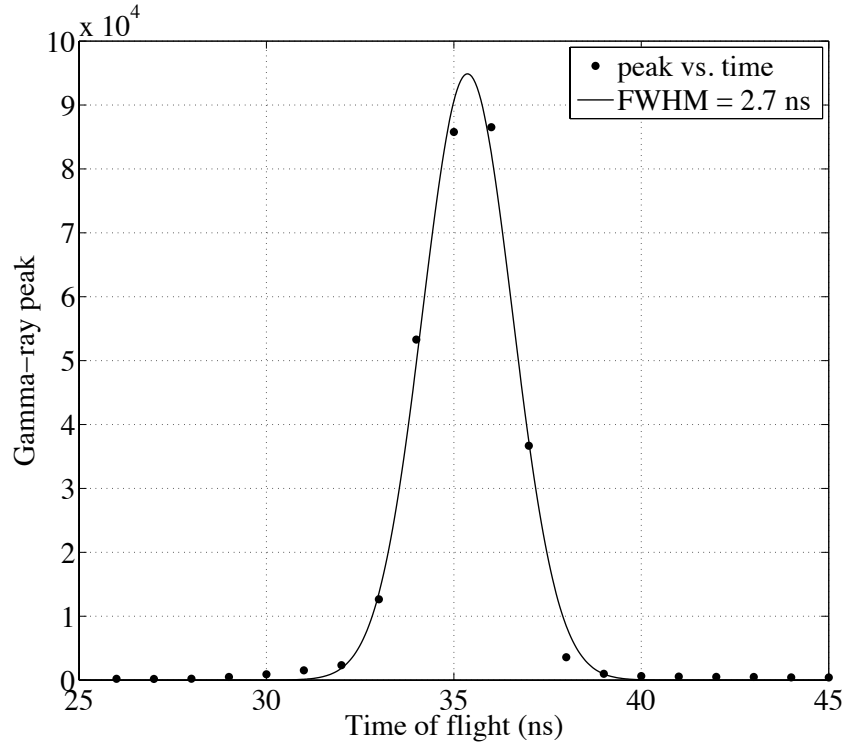
FIG. 4.2. The gamma-ray peak in the TOF spectrum. Timing resolution of the bunching can be estimated by observing the width of the gamma-ray peak, which is a composite of the duration of beam pulses, along with the timing resolution inherent to the detector (EJ309) assembly.

The measurements reported in this thesis were carried out using the 10-MV Van de Graaff accelerator facility at the University of Notre Dame Nuclear Structure Laboratory (UND-NSL). A neutron TOF path of d_{TOF} = 10.84 m was used, and the slowest neutrons of interest - of $E_n \sim$ 0.5 MeV - traverse this distance in approximately $\Delta t_{TOF} \sim 1.2\mu s$. In order to give provide ample time for these slowest neutrons to reach the detector between ion pulses, the bunching period was set to τ_{bunch} = 1.6 µs. As shown in Fig. 4.2, the width of the gamma-ray peak was approximately

2.7 ns, indicating adequate timing resolution, and thus low uncertainty in calculated neutron energies δE_n. Of course, E_n is only derivable from Δt_{TOF} for neutrons that travel directly from the target to the detector without colliding in-between. Thus, we must take care to minimized the contribution to our signal from neutrons which are scattered into our detector from objects in the room. This is the topic of the next section.

4.2 Minimization and characterization of room-scattered neutrons

Figure 4.3 shows a layout of the accelerator facility at UND-NSL, with the 10-MV tandem and the relevant experimental halls labeled [4]. Accelerated ions are guided along beam lines first into the "East target room", and then optionally into the "West target room". This facility has traditionally been used for basic nuclear science research, and has not been optimized for detailed detector characterization. In particular, there is no long dedicated TOF tunnel. In adapting the facility for this purpose, our main challenge was to enable a long TOF path - around ten meters - while minimizing the contribution of room-scattered neutrons to our measurement. This was achieved by using objects in the target rooms as shielding to collimate the neutrons reaching the detector, and through careful placement of the reaction target.

The East and West target rooms are separated by a concrete wall approximately 1.3m thick, through which a beam line passes (see the lower half of Fig. 4.3). A position inside this wall was chosen for the target location so that the surrounding walls would absorb most neutrons exiting the target at large angles (with respect to the incident ion-beam direction). A large ion-beam steering magnet is located about one meter downstream from the wall, and this enhanced the collimation of neutrons. The neutrons of interest - filling a small solid angle about zero degrees - traversed through the zero-degree beam line passing through the magnet and some additional length of evacuated beam line. The room is large enough to place a detector at approximately 10 m from the in-wall target location, at zero degrees, with 4 m clearance to the opposing wall.
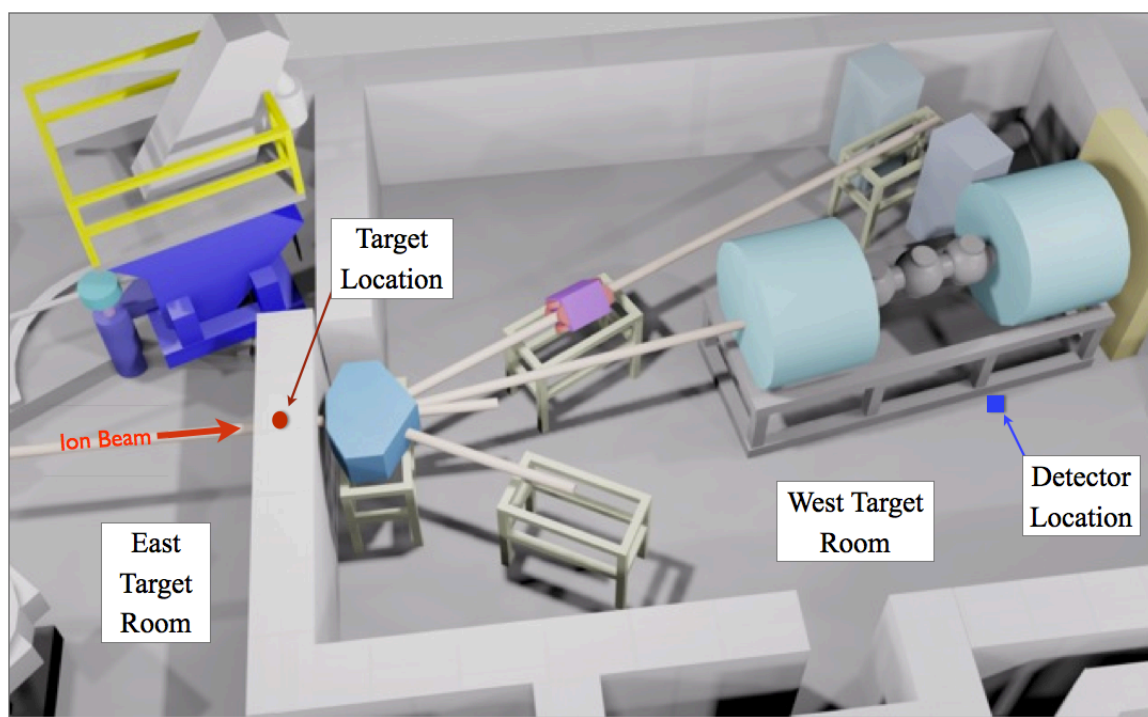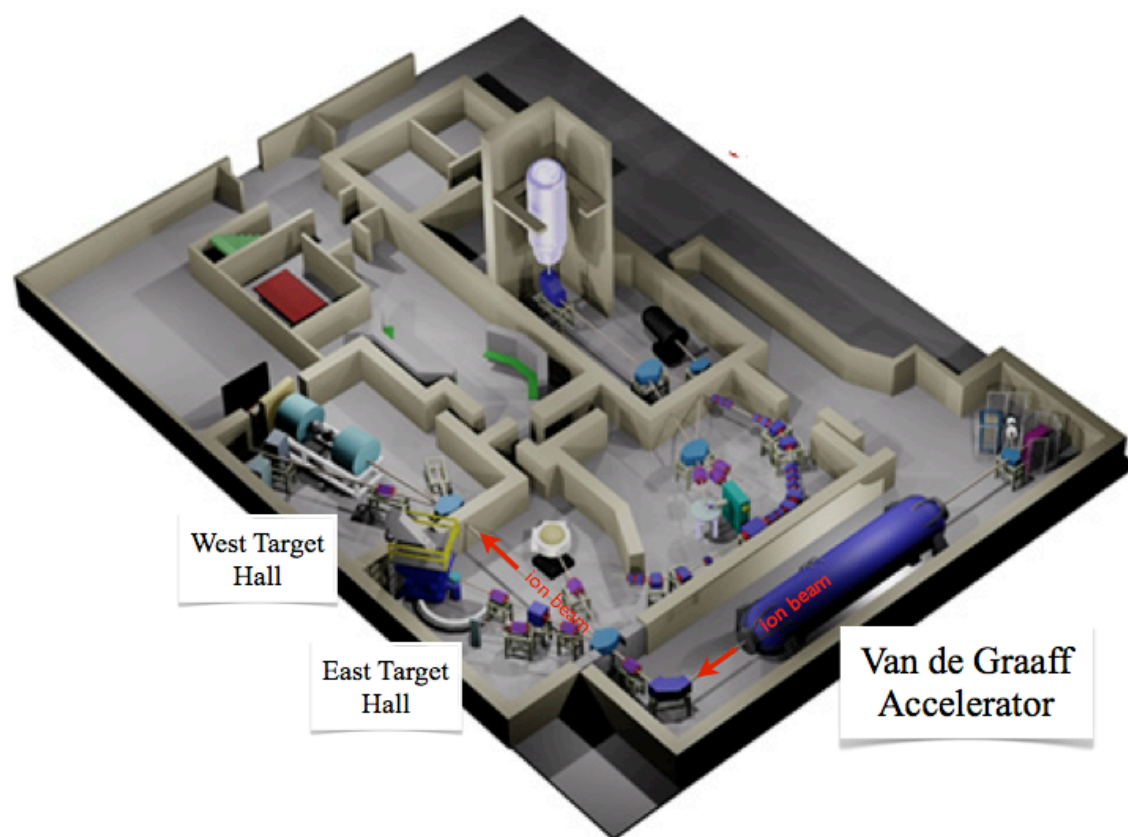
FIG. 4.3. The layout of the nuclear structure laboratory at UND-NSL; placement of in-wall target.

A specially designed target holder was constructed for insertion into the beam line within the wall. The design drawings are shown in Figs. 4.4 and 4.5. The target itself was placed inside a target frame, shown in the upper part of Fig. 4.5. In order to focus the beam onto the target during the experiment, and to monitor the beam current, two separate current measurements are required from the target holder: one from the target itself, and another from a surrounding aperture to detect any portion of the beam which misses the target. These sections of the target holder must be electrically isolated from the beam-line pipe. On the other hand, if the target itself is thermally isolated from the surrounding environment, it may over heat from the beam energy and melt, and spread radioactive target material inside the pipe. In order to avoid this, good thermal contact with the beam line pipe is required.
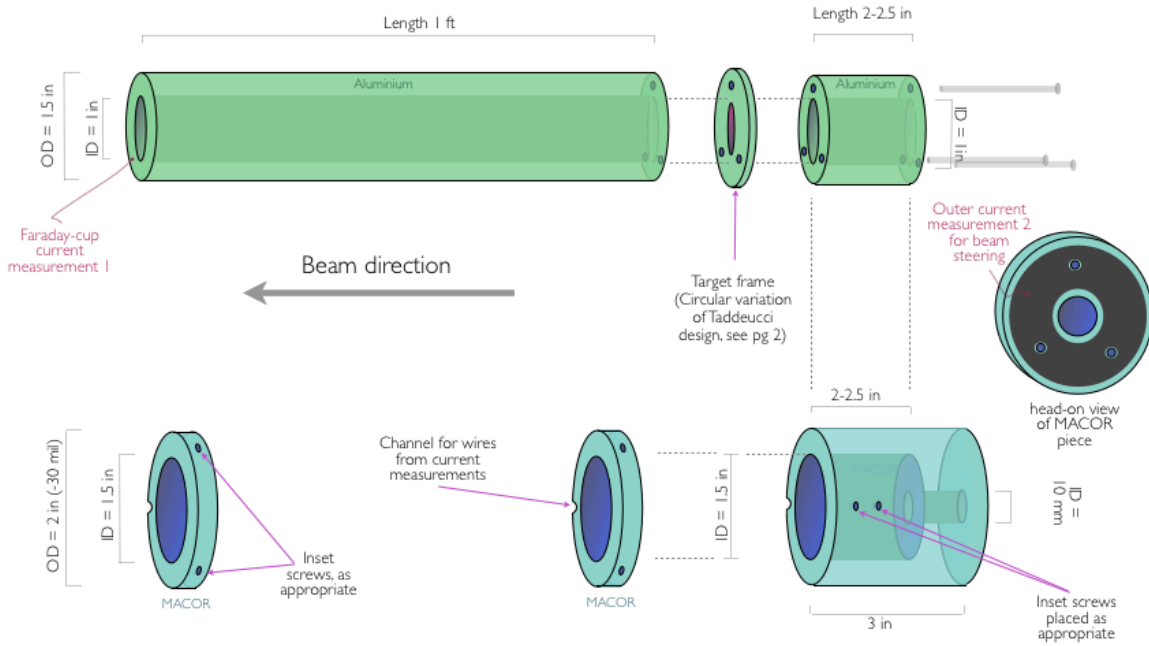
FIG. 4.4. Design drawing of the in-wall target holder designed for creating collimated neutron sources for detector characterization at UND-NSL.
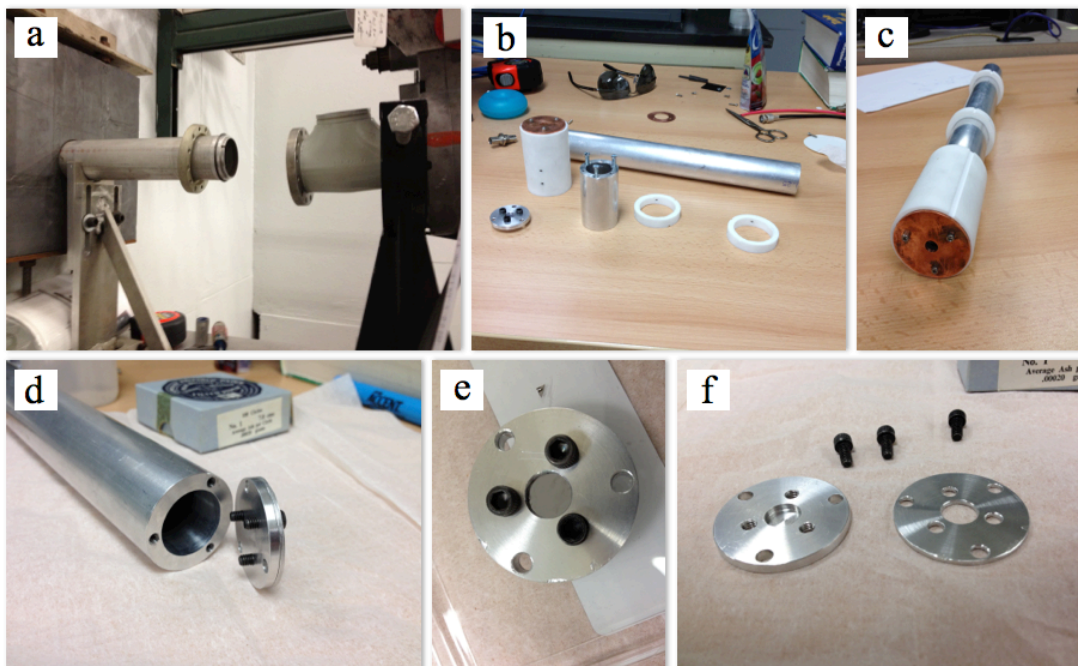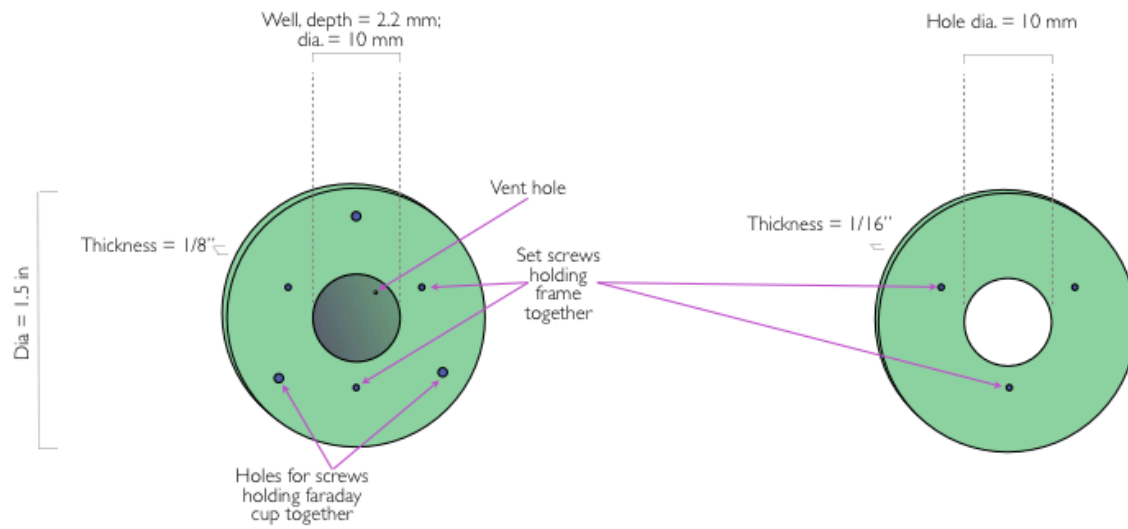
FIG. 4.5. Design drawing of the target frame used in the in-wall target holder (above); photos of the constructed in-wall target holder and frame.

In order to meet these requirements, a 14-inch-long aluminum tube was sectioned as shown in Fig. 4.4 (green parts). The thin slice in the middle formed the target frame. This one-inch-outer-diameter aluminum tube was suspended in the center of the 2-inch-inner-diameter beam-line pipe by an outer structure made of MACOR. MACOR is a machinable ceramic material that has high electrical resistance but good thermal conductivity [5]. The long aluminum tube served as a Faraday cup to absorb any beam current leaving the target in the form of scattered electrons, and to accept much of the heat from the target, which could then radiate from its large surface area. A copper ring was fixed to the upstream surface of MACOR, and this served as the current-collecting aperture for beam tuning. Some photos of the finished target holder are shown in the lower half of Fig. 4.5. This target holder was placed inside the beam line at 80 cm within the concrete wall, as measured from the down-stream wall surface.

4.2.1 Beam-profile measurements

In order to determine how successful this in-wall-target arrangement was at collimating neutrons at the detector location ten meters downstream, beam-profile measurements were carried out in the vicinity of the detector location. The thick ^{11}B target was bombarded with $E_d = $ 5.5-MeV deuterons, as in the later measurements, and the beam current was set to around $I_{target} \sim$ 150 nA, as measured from the target-holder Faraday cup. Current on the copper aperture was negligible ($I_{aperture} < 0.01 I_{target}$) after focusing was carried out. Profile measurements were taken with the three-by-two-inch EJ309 detector placed at several locations spaced three inches apart along vertical and horizontal axes oriented transverse to the beam direction, at a distance of 10 m from the target location. This was just short of the detector distance used for the later detector-characterization measurements. Ten-minute measurements were taken at each location, and the total integrated charge on the target was monitored for each. PSD was used to discriminate between neutron and gamma-ray induced pulses in the detector.

Figure 4.6 shows the results of the profile measurements, plotted as the number of detected neutrons per unit of charge on the target. These measurements indicate excellent collimation at the detector position. There is a beam of neutrons with cross-sectional diameter of

approximately six inches, outside of which the neutron count rate drops by a factor of approximately one hundred. This is surprisingly good considering that there is a pair of large magnets positioned around four meters to the left of the detector location. The fractional contribution of scattered neutrons is likely to be less than this since many would occur outside of the relevant TOF window $0.2 < \Delta t_{TOF} < 1.2$ μs, and can be removed. This arrangement is thus well suited for our detector-characterization measurements.
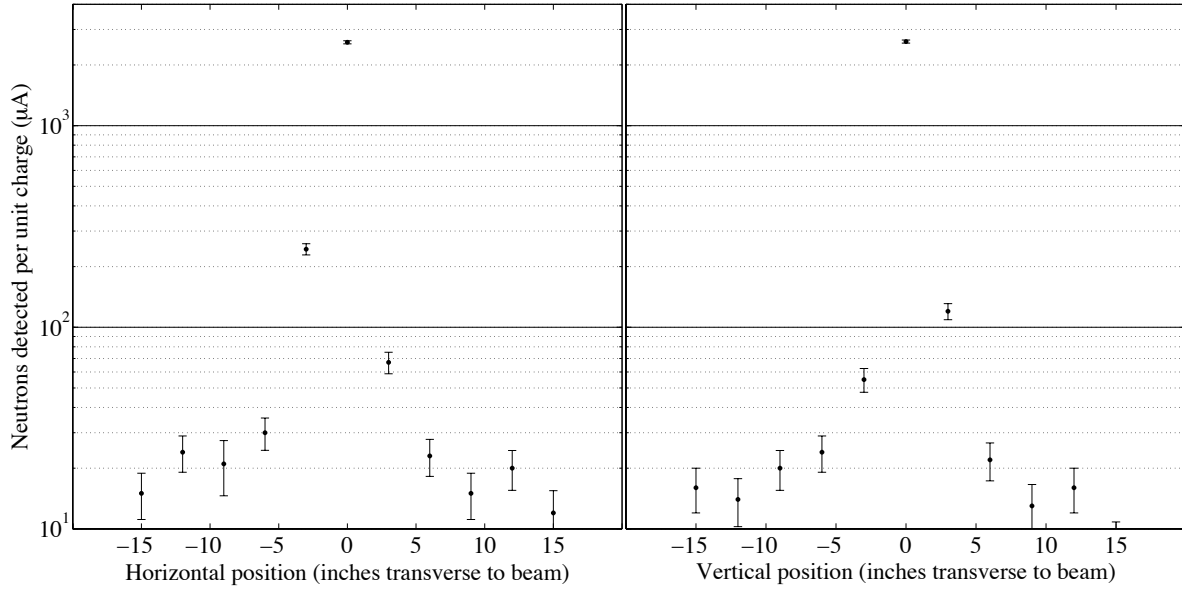
FIG. 4.6. Beam-profile measurements carried out near detector location of ten meters.

4.3 Neutron spectrum from ^{11}B(d,n) with deuteron energy E_d = 5.5 MeV in a stopping target

The reaction ^{11}B(d,n) with was chosen because, with a stopping reaction target, it produces neutrons of a continuous spectrum that extends across our energy range of interest ($0.5 < E_n < 15$ MeV). It also has some distinguishable features in the region above $9 < E_n < 21$ MeV which are useful for beam-tuning diagnostics. The spectrum from this reaction with E_d = 4 MeV has previously been measured by Taddeucci et al. [2], and this can be used for comparison. Since the neutron yield increases slightly with increasing deuteron energy E_d, we chose to use E_d = 5.5 MeV for our measurements. Thus, we expect to see a neutron spectrum of similar shape to that reported by Taddeucci, but shifted slightly higher in energy. Agreement in shape can lend

confidence that all of the deuteron beam is focused on the reaction target, and that all detected neutrons are produced therein. Significant disagreement in shape between the two spectra may indicate that some deuterons are reacting on objects upstream along the beam line, and producing neutrons that are not TOF correlated.

The spectrum at zero degrees from ^{11}B(d,n) with E_d = 5.5 MeV was measured over a period of six hours via TOF, with a three-by-two-inch EJ309 detector at 10.84 m ($\pm$ 5 cm) TOF path length. Figure 4.7 shows the calculated spectrum, normalized as fluence per (MeV*μC*steradian). The detection efficiency of our EJ309 was simulated, and divided out of the measured spectrum. The fractional uncertainty of the normalized fluence value in each energy bin (not shown) is estimated as the quadrature sum of the following fractional uncertainties: uncertainty of integrated charge on the target from incident deuterons; uncertainty in solid angle subtended by the detector; counting uncertainty from Poisson statistics of the number of detected neutrons; and uncertainty in the simulated efficiency. Of these, uncertainty in the simulated efficiency dominates. Comparison between measured and simulated PHS, reported in another study [6], shows fractional agreement in overall counts within 10%, so fractional uncertainty of 10% is attributed to the efficiency simulation. Also included in Fig. 4.3 is the spectrum measured by Taddeucci et al. [2] for the same reaction but lower E_d = 4 MeV. Other than the slight energy shift, which is expected due to the difference in incident E_d, there is very good agreement between the prominent features of the two spectra. However, the absolute fluence from our measurement is higher than that measured by Taddeucci by approximately a factor of three. Some of this difference is likely due to higher E_d. Measurements published by Taddeucci et al. in the same reference indicate that the total integrated neutron yield from ^{11}B(d,n) increases with increasing E_d. From their result, we would expect our neutron yield to be larger than theirs by a factor of ~1.5. The remaining difference, roughly a factor of two, is outside of the uncertainties described above, and remains as a discrepancy between our result and that of Taddeucci. However, the agreement in shape gives us confidence that no interactions are taking place upstream from the target position. Therefore, this is the spectrum of neutrons

used for all of our detector-characterization measurements, carried out in multiple campaigns throughout 2012 and 2013.
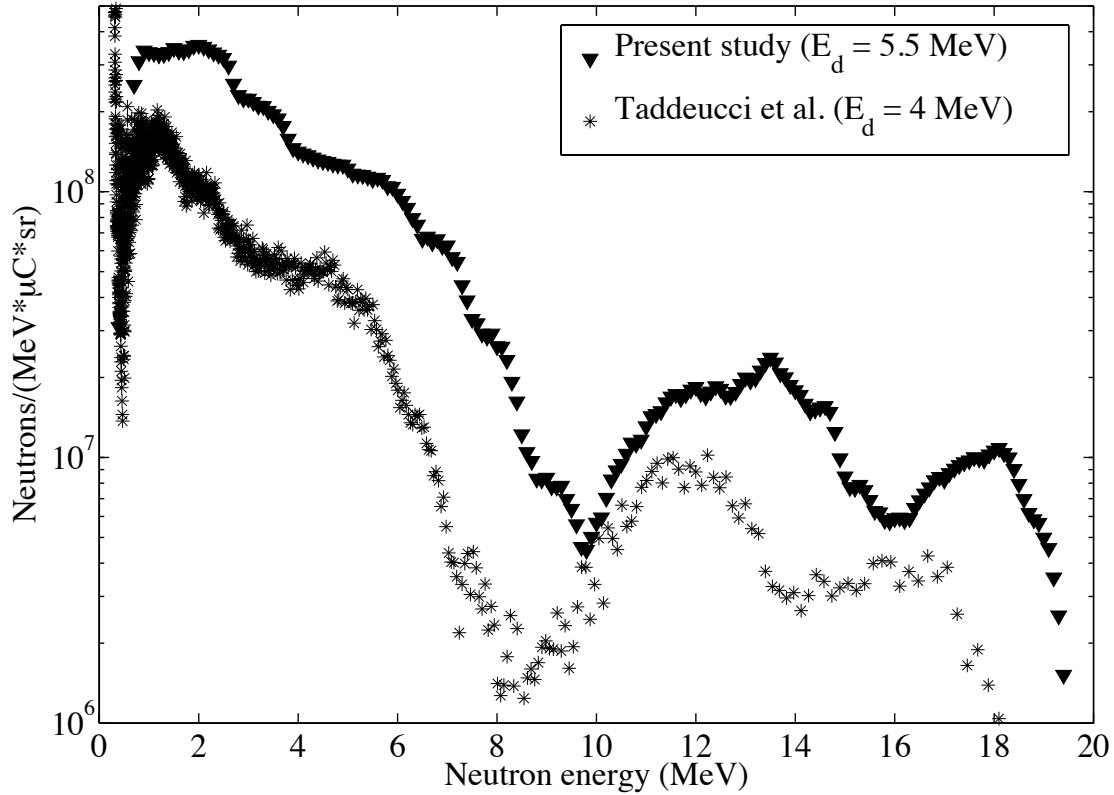
FIG. 4.7. Observed neutron spectrum for the reaction $^{11}B(d,n)$ in a thick target with deuteron energy E_d = 5.5 MeV, measured with an EJ309 scintillator placed at d_{TOF} = 10.84 m. A similar spectrum, measured by Taddeucci et al. for the same reaction with a different deuteron energy is shown for comparison [2].

References

[1]   V. V. Verbinski, W. R. Burrus, T. A. Love, W. Zobel, and N. W. Hill, "Calibration of an Organic Scintillator for Neutron Spectrometry," *Nuclear Instruments and Methods*, vol. 65, pp. 8–25, Jun. 1969.

[2]   T. N. Taddeucci, R. L. Sheffield, T. N. Massey, D. Carter, J. E. O'Donnel, C. R. Brune, D. Ingram, D. Jacobs, and D. Dilullo, "Neutron and Gamma-ray Production with Low-energy Beams," Los Alamos National Laboratory, LA-UR-07-2724, Apr. 2007.

[3]   T. N. Massey, S. Al-Quraishi, C. E. Brient, J. F. Guillemetto, S. M. Grimes, D. Jacobs, J. E. O'Donnel, J. Oldendick, and R. Wheeler, "A Measurment of the 27AL(d,n) Spectrum for Use in Neutron Detector Calibration," *Nuclear Science and Engineering*, vol. 129, pp. 175–179, Aug. 1998.

[4]   U. O. N. Dame, "Accelerator Facilities," *www3.nd.edu*. [Online]. Available: http://www3.nd.edu/~nsl/html/research_facilities.html. [Accessed: 09-Apr-2014].

[5]   "MACOR," Corning, Aug. 2001.

[6]   S. A. Pozzi, S. D. Clarke, W. J. Walsh, E. C. Miller, J. L. Dolan, M. Flaska, B. M. Wieger, A. Enqvist, E. Padovani, J. K. Mattingly, D. L. Chichester, and P. Peerani, "MCNPX-PoliMi for nuclear nonproliferation applications," *Nuclear inst. and Methods in Physics Research, A*, vol. 694, no. C, pp. 119–125, Dec. 2012.

Chapter 5
Light-output Relations and Pulse-height
Resolution Measurements

Chapter 2 described some of the important attributes of organic-scintillator response, and how they effect the shapes of measured PHS. Scintillation light output and pulse-height resolution are two of the most important of these attributes, and can be measured using the accelerator measurements described in Chapter 4. This chapter will be devoted to these calculations. In Chapter 6, I will describe how we can improve the condition of a response matrix by choosing a discretization scheme which removes the non-linearity of the light-output relations measured here, and how the difference in resolution between EJ309 and EJ299-33 correspond to differences in their matrix condition. These relations are also necessary for accurate detector simulation, and for a fair comparison between the PSD performances of different detectors. Data needed for these calculations were acquired in nine hours for each detector, at a TOF distance $d_{TOF} = 10.84$ m, during measurement campaigns in Fall of 2012 and Fall of 2013.

5.1 Light output relations

The light-output relation $L_{scint}(E_p)$ is between the amount of energy E_p deposited on a single recoil nucleus in the detector medium, and the amount of resulting scintillation light L_{scint} produced as the recoil nucleus slows down within the medium. For reasons described in Chapter 2, L_{scint} is commonly expressed in units of MeV "electron equivalent", or MeVee, via calibration with gamma-ray sources. One MeVee is the amount of light produced by a one-MeV electron slowing down and stopping in the detection medium. As described in Chapter 3, the light output relation is non-linear due to a quenching-like effect. As the recoil nucleus slows down and deposits its energy along its track via the Coulomb interaction, it exhausts the excitable scintillating systems which are locally available along that track. The remaining fraction of E_p is

"wasted" on the excitation of non-scintillating systems. The fraction of energy leading to scintillation is inversely proportional to dE/dx, resulting in the nonlinearity of the $L_{scint}(E_d)$ [1]. Additionally, larger recoil nuclei such as ^{12}C, which deposit their energy along a shorter track length than do smaller nuclei of the same initial energy, produce less overall scintillation light [2], [3].

Using the TOF data obtained from the accelerator measurements described in Chapter 4, we can create a series of TOF-gated PHS associated with quasi-mono-energetic neutron spectra of different energies. An example is shown in Fig. 5.1, where PHS from the three-by-two-inch EJ309 detector are plotted for various 100-keV-wide neutron-energy groups. Once these quasi-mono-energetic PHS are obtained, we can associate certain features with some known fraction f_{dep} of energy transfer from incident neutron to recoiling particle.

$$E_p = f_{dep} * E_n. \tag{5.1}$$

Then the location of those features along the pulse-height axis L can be associated with the estimated energy deposition E_p to extract a light-output datum (E_p, L_{scint}). After performing this estimation of (E_p, L_{scint}) for many PHS of different incident neutron energies E_n, we obtain an array of light-output data across a range of energies.

Since hydrogen-based and deuterium-based scintillators rely on different neutron scattering kinematics (*n-p* versus *n-d* scattering), the above procedure will have to be carried out differently for these different detector types. In Sections 5.1.1 and 5.1.2 we will consider them in turn.
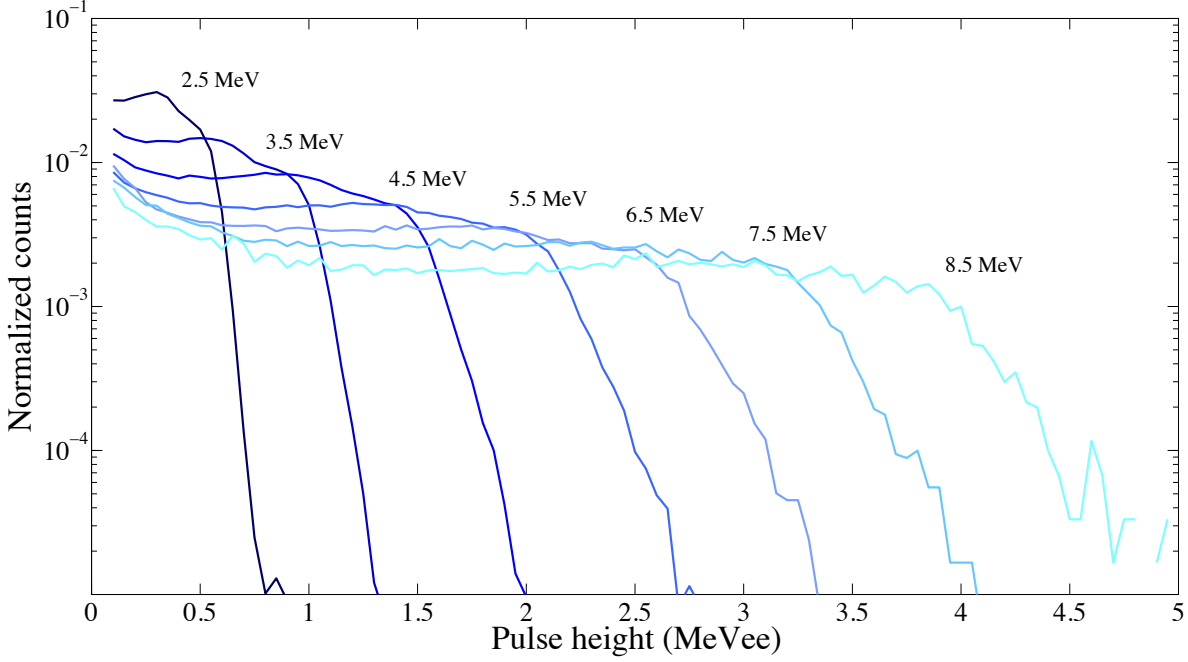
FIG. 5.1. Scintillator pulse-height spectra from quasi-mono-energetic neutron sources, obtained using 100-keV-wide time-of-flight gates, measured with the EJ309 detector.

5.1.1 Extracting light-output data for hydrogen-based scintillators

Figure 5.2 shows an example of a PHS from EJ309 resulting from quasi-mono-energetic neutrons, indicated by blue squares. The hydrogen-based plastic EJ299-33 produces similar PHS, but with falling edges of more gradual slope due to the poorer resolution. As described in Chapter 2, PHS arising from fission-energy neutrons in hydrogen-based detectors are dominated by *n-p* scattering, which is isotropic in the center-of-mass frame. A neutron can deposit up to its entire incident energy E_n onto a proton in a single collision. Thus, the high-pulse-height extent of the PHS shown in Fig. 5.2 corresponds to neutrons which deposit their entire energy onto a proton in a single collision. This can be associated with the drop off located just below 0.8 MeVee. Other features in lower-pulse-height regions can be associated with neutrons that deposit some fraction of their energies in one or more collisions [4], [5]. So if we can devise a systematic way of "locating" the falling edge of the PHS, its position L_{edge} along the pulse-height axis can be associated with full energy deposition $E_{p=1} = E_n$ to yield the datum $(E_{p=1}, L_{scint}) = (E_n, L_{edge})$.

One way of locating L_{edge} is described in Refs. [6] and [7]. First, the PHS is smoothed using a running average and the smoothed PHS is differentiated, as indicated by the green diamonds in Fig. 5.2. A Gaussian-like feature in the differentiated PHS is associated with the falling edge of the original PHS. A Gaussian function is fit to a portion of this feature, and location of the Gaussian centroid L_{cent} is associated with the the edge of the PHS L_{edge}, and ultimately with the light-output L_{scint} resulting from full energy deposition $E_{p=1} = E_n$:

$$L_{cent} \equiv L_{edge} \equiv L_{scint} \tag{5.2}$$

These steps are performed for quasi-mono-energetic measured PHS arising 100-keV-wide TOF gates extending from 0.4 to 7 MeV, for both hydrogen-based detectors EJ309 and EJ299-33.
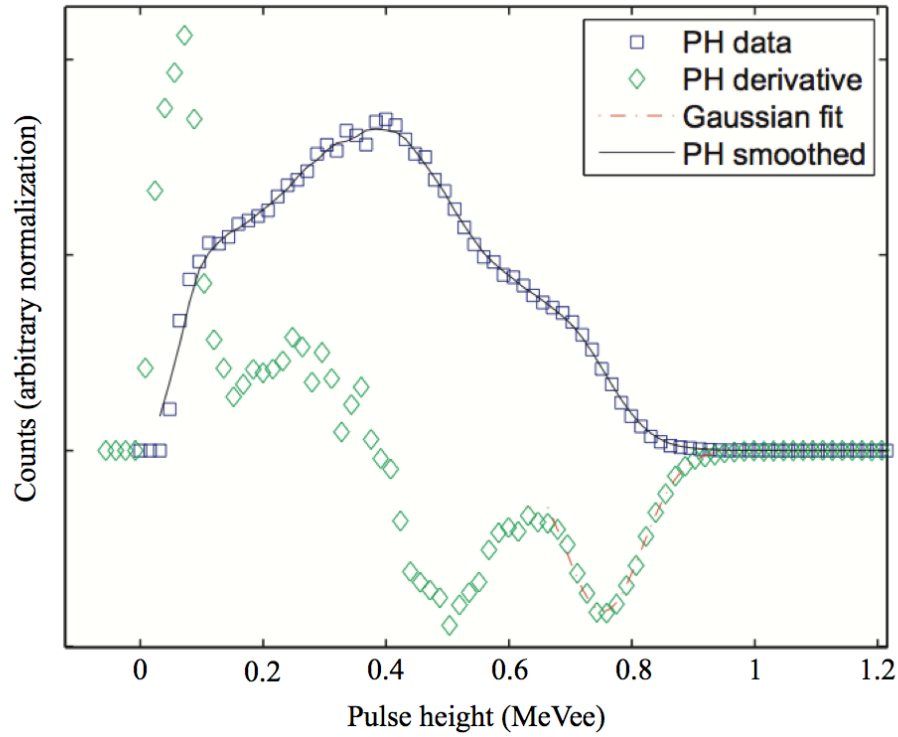
FIG. 5.2. Extraction of one (E_p,L) datum for hydrogen-based scintillators from a quasi-mono-energetic pulse-height spectrum. The centroid of a Gaussian, fit to the differentiated curve, marks the light-output of full-energy-deposition events. The FWHM of the Gaussian provides an estimate of the resolution.

5.1.2 Extracting light-output data for deuterium-based scintillators

Due to the backward-peaked *n-d* scattering cross section, the pulse-height response from deuterated scintillators exhibits a modest "backscatter peak". Additionally, backscattered neutrons from *n-d* scattering deposit the maximum fraction of their energy onto the recoiling deuteron that is kinematically possible:

$$E_{d\,max} = 8/9\ E_n. \tag{5.3}$$

The location L_{bs} of the corresponding back-scatter peak can be associated with this energy transfer. However, due to the smearing of the backscatter peak from pulse-height resolution, it can be difficult to identify its true position.

In order to resolve this, we adopt a procedure described by Croft et al. [8]. For each measured quasi-mono-energetic PHS, a preliminary light-output datum is calculated by attributing the half height of the falling edge to the back-scatter-peak location L_{bs}. These preliminary data are used to estimate a light-output relation for use in simulation of detector response with MCNP-PoliMi [9], [10]. Two simulations are calculated for each measured energy group - one for neutron energies evenly distributed across the 100-keV energy bin and with pulse-height resolution $\Delta L/L$ folded in (measured as described in Section 5.2 of this chapter), and one with truly mono-energetic neutrons from the energy-bin center, and with no resolution included. Both simulated PHS are superimposed in a single plot for each energy group, as exemplified in Fig. 5.3. Then the intersection of the two simulated PHS is used to adjust the height fraction for attribution of the true backscatter peak for each measured energy group. With these new height fractions - which range from 0.62 to 0.66 - the final light-output data are calculated.
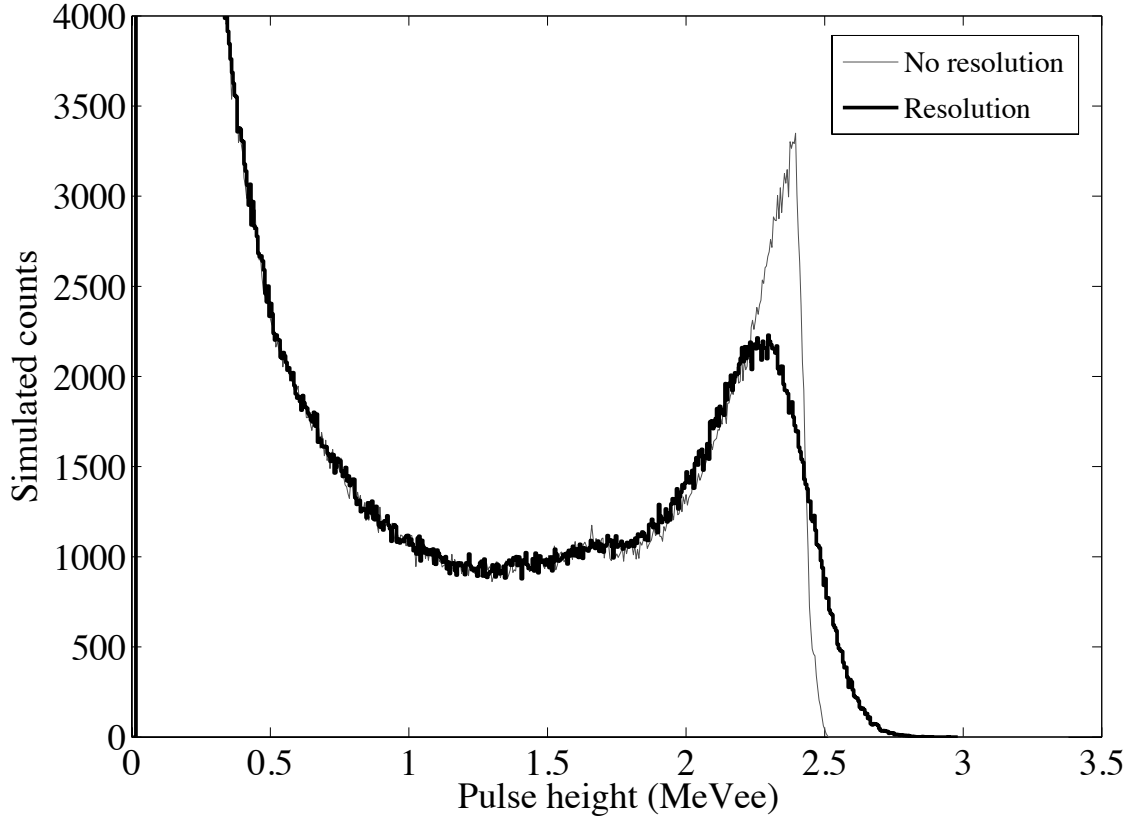
FIG. 5.3. Attribution of 8/9-energy transfer of a single back-scatter collision to a location along the pulse-height axis, for extraction of one (E_d,L) datum for a deuterated scintillator. In order to estimate the effect of resolution, MCNP-PoliMi simulations are performed with and without resolution. The intersection of the edges marks the fractional height ot the true back-scatter location. The calculated fraction is then used to extract the datum (E_d,L) from the measured pulse-height spectrum

5.1.3 Light-output data

Scintillation light-output data for our three-by-two-inch EJ309 and EJ315 detectors, along with the three-by-three-inch EJ299-33, are shown in Fig. 5.4. As expected, the light output from the hydrogen-based EJ309 is higher than that from the deuterated EJ315 [2], [3]. This is due to the higher mass of the deuteron, resulting in higher dE/dx for recoil deuterons than from recoil protons of the same initial energies. The fractional difference is approximately 35% across the energy range measured. The light output for the plastic EJ299-33 falls somewhere in between.

The fractional uncertainty of each data point (E_d,L_{scint}) for the deuterated detector is calculated as the quadrature sum of the following fractional uncertainties: uncertainty in the identification of the 8/9 energy-deposition location; uncertainty in the height of the back-scatter peak; and uncertainty in the light-output calibration. The uncertainty in the 8/9 energy-deposition location was derived from the upper and lower bounds of the height fractions stated above - 0.62 to 0.66. The uncertainty of the maximum of the back-scatter peak was calculated by multiplying the Poisson variance by the inverse slope of the PHS at the position of the stated (E_p,L_{scint}). Uncertainty of the calibration is stated above as 0.02. Fractional uncertainties for the (E_p,L_{scint}) data points for the hydrogen-based detectors in Fig. 5.4 were calculated similarly, except that the uncertainties of the full-energy-deposition locations were calculated using the uncertainties of the centroids in the Gaussian fits which were applied to the differentiated PHS.
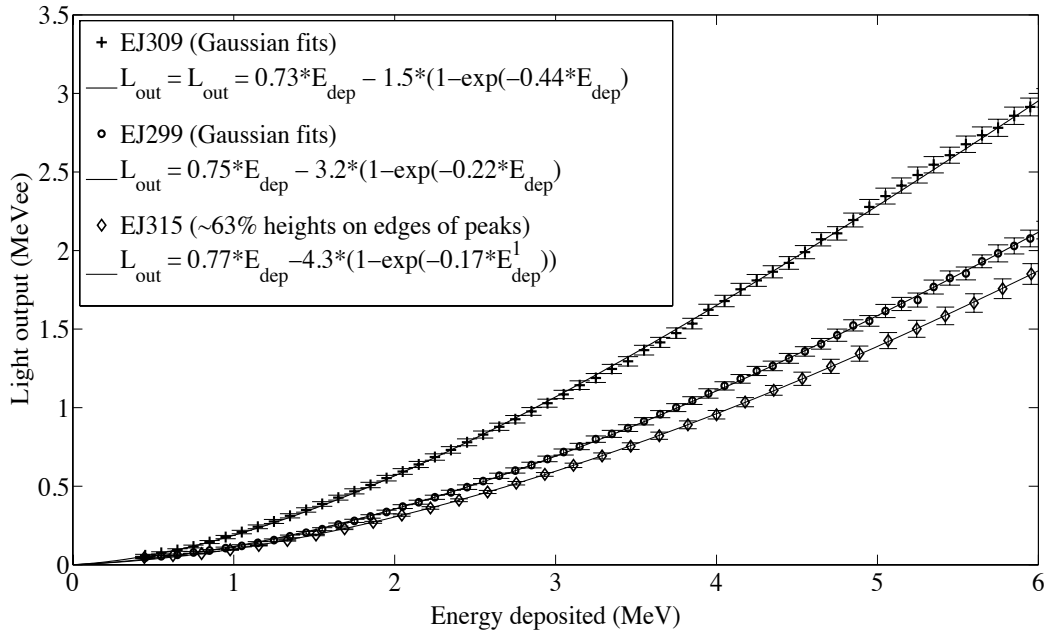
FIG. 5.4. Light output relations calculated for the hydrogen-based EJ309 and EJ299-33, and for the deuterium-based EJ315 detectors. Data are fitted with the functional form Eq. 5.5 for use in Monte Carlo simulations.

Figure 5.5 shows a comparison of our (E_d,L_{scint}) data for EJ315 to data for NE230 measured by Croft et al. [8]. Our data for EJ315 is lower than Croft's data by several sigma relative to the electron signal. This suggests that Eljen's formula EJ315 for a deuterated-benzene scintillating liquid may have a slightly lower intrinsic light-output relation than NE230. This is

not without precedent - others have found differences in light output between formulas from different brands which were claimed to be identical. For instance, it has been shown that BC501A has 20% larger light output for photons than NE213 [11].
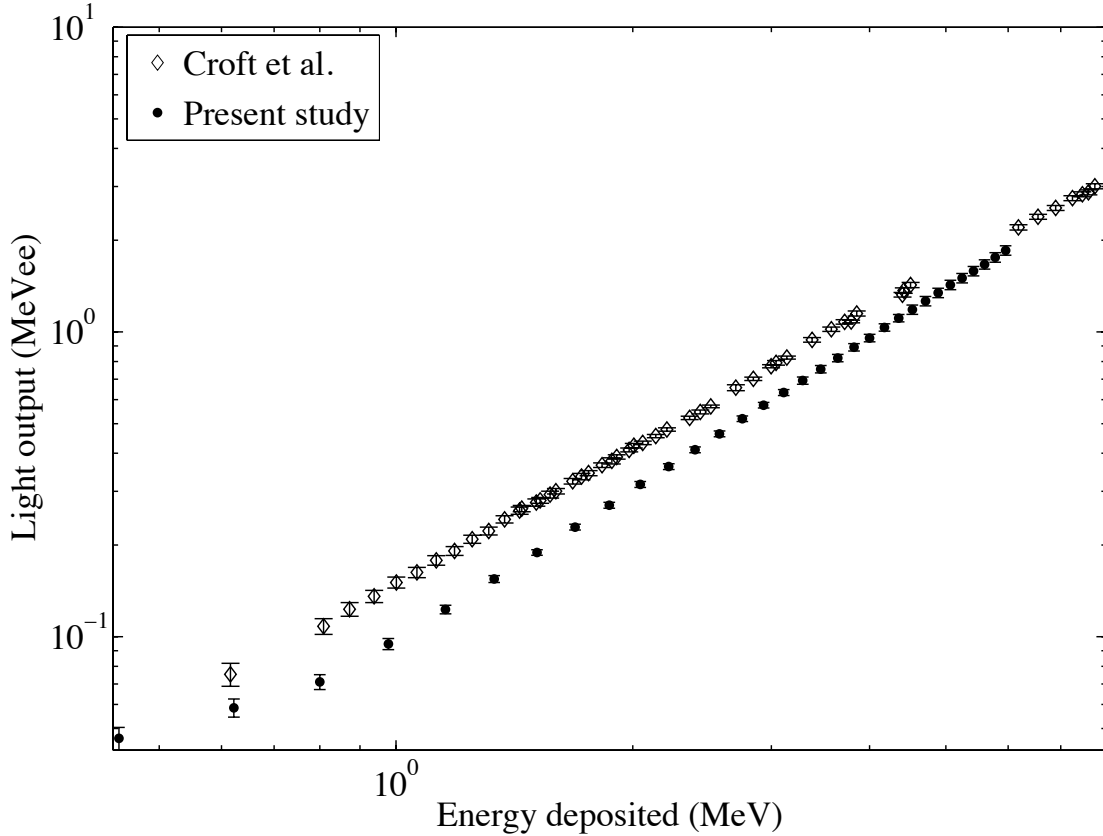
FIG. 5.5. Comparison between the light-output data determined here for the deuterated EJ315, and that reported by Croft. et. al. for the deuterated NE230 [8].

In order to use these light-output data for accurate simulation of detector response in MCNP-PoliMi, we must fit some functional form, and one of the important questions is: what is the best functional form to represent the light-output relation? Multiple functional forms have been proposed, including simple polynomial relations, power laws [8], and rational and exponential forms [6]. Since these curves are largely empirical, having many evenly spaced data points is important for determining which functional form best represents the true relation. In a recent publication, we presented measurement of light-output data for a larger (three-by-three-inch) EJ309 detector and fit multiple functional forms to the data [7]. We then investigated the

performance of each functional form in simulation of detector response using MCNPX PoliMi. We find that even similar looking functional forms lead to dramatically different simulated PHS shapes, and that an exponential relation performs best while giving excellent fit to our measured data [7]:

$$L_{scint}(E_p) = aE_p - b(1-\exp(-cE_p)), \qquad (5.4)$$

and I adopt this functional form here. The fits of form Eq. 5.4 are included in Fig. 5.4 for each detector.

5.2 Pulse-height resolution

The method used to calculate the light-output data for hydrogen-based detectors can also be used to estimate the pulse-height resolution of those detectors. The widths of the Gaussian fits correspond to a composite of several blurring effects: energy uncertainties introduced by the timing resolutions and TOF-distance uncertainty (including variation in penetration of neutrons into the detector active volume prior to collision); the energy widths of the TOF groupings; a subtle blurring from the moving average smoothing; and finally, the detector resolution dL/L itself. The extra-resolution effects can be removed to yield a calculation of detector resolution. The calculated resolution data for our EJ299-33 plastic and EJ309 liquid detectors are shown in Fig. 5.6. Resolution datasets were fit with the following functional form:

$$\left(\frac{\Delta L_{out}}{L_{out}}\right) = \sqrt{\alpha^2 + \frac{\beta^2}{L_{out}} + \left(\frac{\gamma}{L_{out}}\right)^2}. \qquad (5.5)$$

Unfortunately, the shape of the PHS for the deuterated detector does not provide easy extraction of the pulse-height resolution for that detector. However, simulation of PHS for deuterated detectors indicates that the resolution is very similar to that for EJ309.
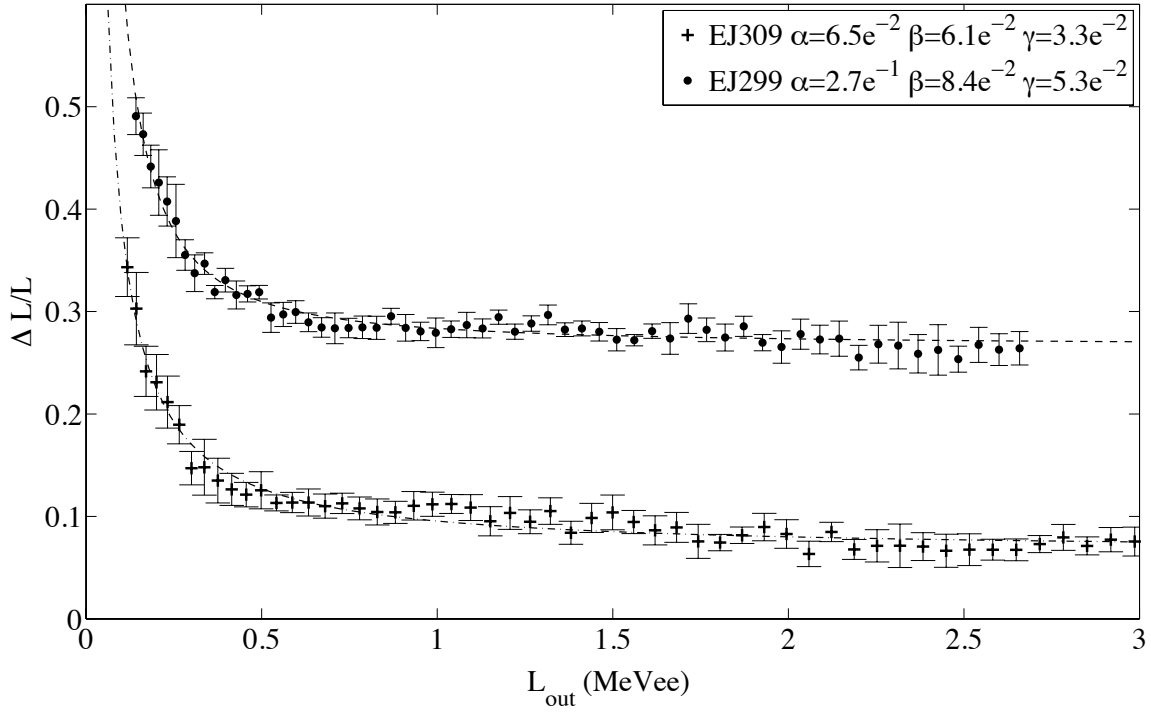
FIG. 5.6. Pulse-height resolution determined for the hydrogen-based liquid EJ309 and plastic EJ299-33.

5.3 Remarks

The results presented in this chapter suggest two important outcomes. First, the light output for the deuterated EJ315 and the hydrogen-based plastic EJ299-33 are considerably lower than that for the hydrogen-based liquid EJ309. Light output will be a factor in the effective energy resolution, so lower light output is a drawback. However, we will find in the following chapters that the advantage of *n-d* scattering is sufficient to yield an improvement in matrix condition for the EJ315 over EJ309, in spite of the disadvantage in light output. The second important result is that the EJ299-33 has much poorer pulse-height resolution than the EJ309. The lower light output and poorer resolution will culminate in a substantial disadvantage for unfolding with the plastic detector.

References

[1]   J. Birks, *Theory and Practice of Scintillation Counting*. Pergemon Press.

[2]   R. L. Craun and D. L. Smith, "Analysis of Response Data for Several Organic Scintillators," *Nuclear Instruments and Methods*, vol. 80, pp. 239–244, Jun. 1970.

[3]   F. D. Becchetti, C. E. Thorn, and M. J. Levine, "Response of Plastic Scintillator Detectors to Heavy Ions, Z<=35, E<=170 MeV," *Nuclear inst. and Methods in Physics Research, A*, vol. 138, pp. 93–104, Jun. 1976.

[4]   A. Enqvist and I. Pázsit, "Calculation of the light pulse distributions induced by fast neutrons in organic scintillation detectors," *Nuclear Instruments and Methods in Physics Research Section A: Accelerators, Spectrometers, Detectors and Associated Equipment*, vol. 618, no. 1, pp. 266–274, Jun. 2010.

[5]   S. A. Pozzi, M. Flaska, A. Enqvist, and I. Pázsit, "Monte Carlo and analytical models of neutron detection with organic scintillation detectors," *Nuclear Instruments and Methods in Physics Research Section A: Accelerators, Spectrometers, Detectors and Associated Equipment*, vol. 582, no. 2, pp. 629–637, Nov. 2007.

[6]   N. V. Kornilov, I. Fabry, S. Oberstedt, and F. Hambsch, "Total characterization of neutron detectors with a 252Cf source and a new light output determination," *Nuclear Instruments and Methods in Physics Research Section A: Accelerators, Spectrometers, Detectors and Associated Equipment*, vol. 599, no. 2, pp. 226–233, Feb. 2009.

[7]   A. Enqvist, C. C. Lawrence, B. M. Wieger, S. A. Pozzi, and T. N. Massey, "Neutron Light-output Response and Resolution Functions in EJ-309 Scintillation Detectors," *Nuclear inst. and Methods in Physics Research, A*, vol. 715, no. C, pp. 79–86, Jul. 2013.

[8]   S. Croft, J. M. Adams, D. S. Bond, N. P. Hawkes, and N. Watkins, "A measurement of the light output function of the deuterated liquid scintillator NE-230 to recoil deuterons with energies between 0.62 and 14.5 MeV *," *Nuclear Instruments and Methods in Physics Research A*, vol. 316, pp. 324–332, Jul. 1992.

[9]   E. Padovani and S. A. Pozzi, "MCNP-POLIMI Manual," pp. 1–27, Mar. 2003.

[10]   S. A. Pozzi, S. D. Clarke, W. J. Walsh, E. C. Miller, J. L. Dolan, M. Flaska, B. M. Wieger, A. Enqvist, E. Padovani, J. K. Mattingly, D. L. Chichester, and P. Peerani, "MCNPX-PoliMi for nuclear nonproliferation applications," *Nuclear inst. and Methods in Physics Research, A*, vol. 694, no. C, pp. 119–125, Dec. 2012.

[11]   M. Moszynski, G. J. Costa, G. Guillaume, B. Heusch, A. Huck, and S. Mouatassim, "Study of n-gamma Discrimination with NE213 and BC501A Liquid Scintillators of Different Size," *Nuclear Instruments and Methods in Physics Research A*, vol. 350, pp. 226–234, Jun. 1994.

Chapter 6
Measurement of Response Matrices

Response matrices R can be calculated from TOF data measured using the experimental techniques described in Chapter 4. Here I present measured matrices for the hydrogen-based liquid EJ309 and plastic EJ299-33, and the deuterium-based EJ315. As indicated in the appendix, the EJ309 and EJ315 are in identical Scionix assemblies with three-by-two-inch cylindrical active cells, while the EJ299-33 plastic has a three-by-three-inch active volume. All three include identical ETL 9821B photo-multiplier tubes. Data is acquired for nine hours with each detector at a TOF distance d_{TOF} = 10.84 m. Pulses arising from gamma-ray events are removed using PSD techniques as described in Chapter 2. The resulting neutron pulse-height and TOF data can then be discretized with any binning structure desired in neutron-energy E_n and pulse height L_{scint} to produce an un-normalized response matrix. Normalization is carried out such that each column, corresponding to an energy group ΔE_j integrates to the intrinsic detection efficiency $\langle \epsilon(E_n) \rangle_{\Delta E}$ of the detector averaged over the energies of the group ΔE_j. Efficiency $\epsilon(E_n)$ is simulated using MCNP-PoliMi [1] and this is the only reliance on Monte Carlo simulation. Since detection efficiency relies mainly on the scattering cross sections of hydrogen, deuterium and carbon - all of which are well known - we can expect these simulated efficiencies to be accurate [1].

As a preliminary calculation for this chapter, matrices were constructed using 100-keV energy bins and 50-keVee pulse-height bins for all detectors. We will find in Chapter 7 that this discretization structure is far from optimal, but it will suffice to reveal some of the structure of each matrix.
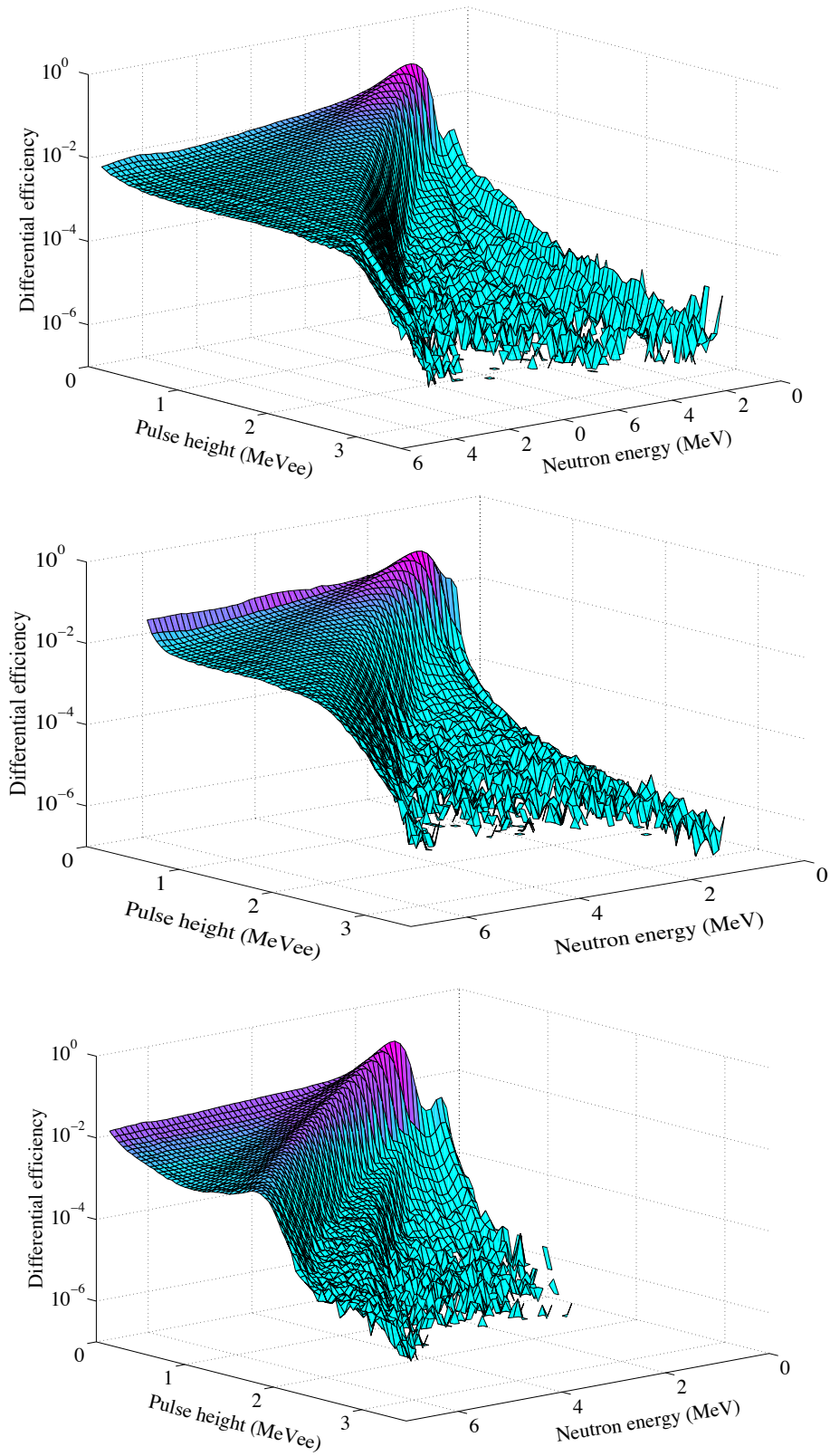
FIG. 6.1. Measured response matrices for EJ309 (top), EJ299-33 (center) and EJ315 (bottom).

The resulting matrices are shown in Fig. 6.1, with the EJ309 on top, EJ299-33 in the center, and EJ315 on the bottom. All are truncated to highlight the prominent features below 7-MeV neutron energy. There is a ridge in the matrix for EJ315 corresponding to the 8/9 energy transfer in back-scattering events, while the EJ309 and EJ299-33 matrices each look more like a plateau. We hope to exploit this difference in future studies of spectrum unfolding. Figure 6.2 shows seven selected columns from each matrix, corresponding to normalized PHS from quasi-mono-energetic incident neutron spectra of different energies. Back-scatter peaking represents the prominent distinction of the EJ315 PHS. The PHS from the EJ315 also shows a small amount of structure from *n-p* scattering and deuteron breakup, which extends some distance past the backscatter peaks. Some *n-p* scattering is expected, since EJ315 contains some hydrogen: approximately $3.5e^{-3}$ atom fraction, versus ~ 0.496 for deuterium and ~ 0.5 for carbon. The distance by which these structures extend past the back-scatter peaks is accounted for by the difference in light output, as well as the fact that *n-p* scattering can result in full transfer of E_n to the recoiling proton, as opposed to 8/9 for *n-d* scattering. These structures line up with the elbows of the corresponding PHS from the EJ309 plot, as expected.
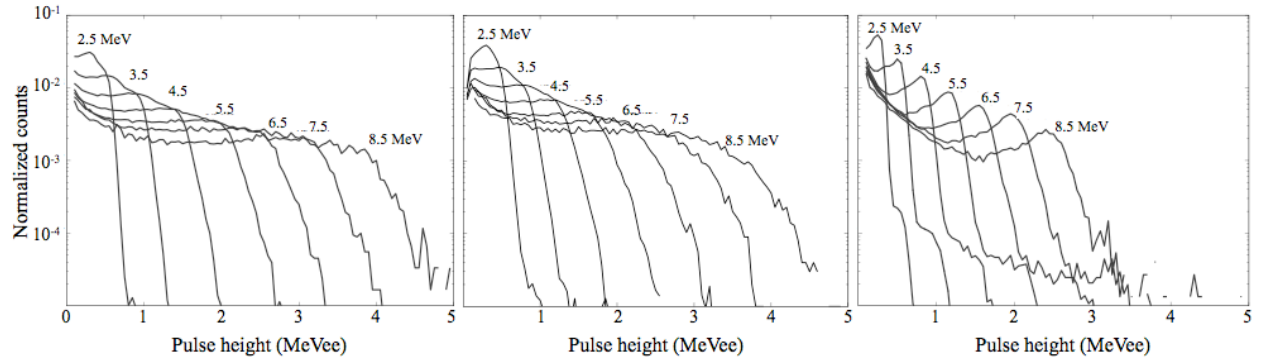
FIG. 6.2. Seven columns selected from the response matrix for EJ309 (left), EJ299-33 (center) and EJ315 (right).

As a first test, I present some initial unfolding trials. Trial spectra were obtained for each detector using a ^{252}Cf fission-neutron source placed a distance of 30 cm from detector face. PHS were obtained in a measurement time of three hours for each detector. This resulted in $1.1e^6$ detected neutrons in the PHS from EJ309, $8e^5$ detected neutrons in the PHS for EJ299-33, and $7e^5$ detected neutrons in the PHS from EJ315. These differences are expected since the

differences in light-output affect the detection efficiency (less pulses are likely to break the detection threshold), and because the cross section for *n-d* scattering is smaller than that for *n-p* scattering over this energy range. The resulting PHS are shown in Fig. 6.3.

Unfolding for these trials is carried out using the simple unfolding code described in appendix A.1. However, since our purpose here is to compare spectrum-unfolding performance between our detectors with the simplest unfolding algorithm possible, I chose to forego regularization and perform spectrum unfolding with larger energy bins, with widths of between 300 and 500 keV.
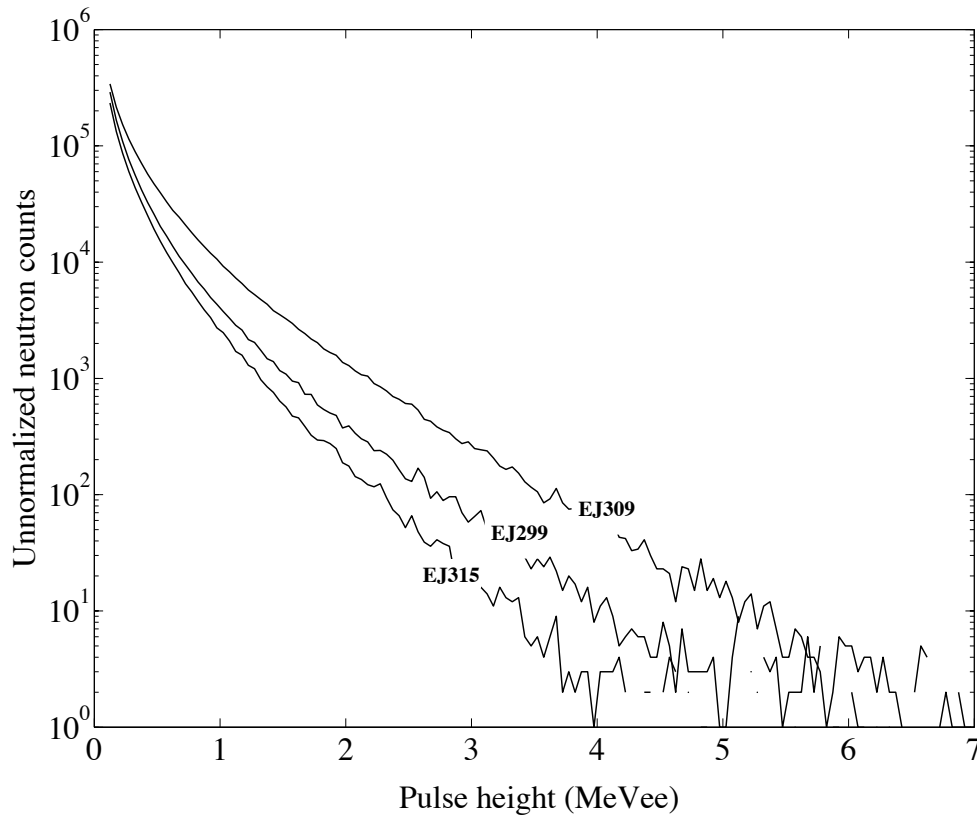
FIG. 6.3. Pulse-height spectra measured with EJ309, EJ299-33 and EJ315 detectors from a [252]Cf fission-neutron source in three hour measurements for each detector. Gamma-ray pulses are removed using pulse-shape discrimination.
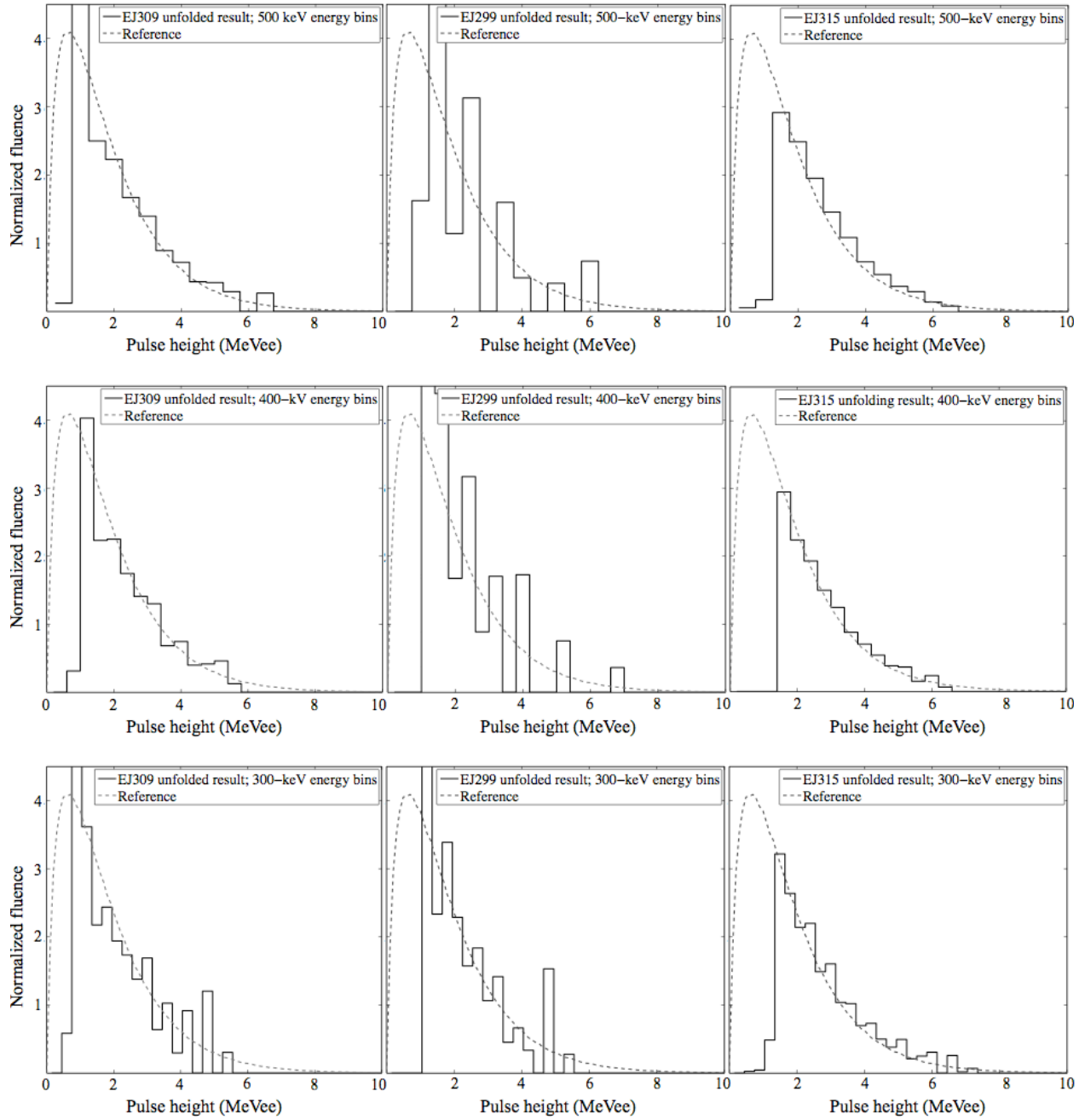
FIG. 6.4. Unfolded neutron spectra from ^{252}Cf measured in EJ309 (left), EJ299-33 (center), and EJ315 (right). Energy-group widths of 500 keV (top), 400 keV (center), and 300 keV (bottom) are used.

From the unfolding results, we can see a number of the effects predicted in previous chapters. Recall that our continuous-spectrum TOF measurement allows us to discretize the *R* with any energy binning desired (see Chapter 4), and that *R* becomes ill conditioned as the

energy-binning is made finer (see Chapter 3). Figure 6.4 shows unfolding trials for each detector carried out with three different discretization schemes - each with progressively more and narrower energy bins - to demonstrate the onset of oscillatory error in the unfolded solutions due to the progressively degraded matrix condition. We can also clearly see the disadvantage of the lower-resolution EJ299-33 plastic - whose solutions are dominated by oscillatory error even for the 500-keV-wide binning - and the advantage of the deuterated EJ315, which produces less oscillations for all three binning structures.

The reader may note that the low-energy cutoff in Fig. 6.4 is higher for EJ315 than it is for EJ309 and EJ299-33. Differences of this nature result from lower light output, and from the difference in single-collision maximum energy transfer. The effect of this is that, for a given pulse-height detection threshold, the minimum detectable neutron energy for EJ315 is higher than that for EJ309 or EJ299-33, and hence the difference in low-energy cutoff. However, the main limitation on lowering the detection threshold is PSD performance, which degrades at lower pulse heights. This can be improved using certain proprietary additives as discussed in Ref. [2].

The unfolding results shown in Fig. 6.4 represent a first successful unfolding result, indicating the successful measurement of response matrices for both. They also illustrate many of the concepts described in previous chapters. They do not, however, represent the quality of results that can be achieved using basic regularization techniques, and more optimal discretization structures. In the next chapter, I will investigate matrix condition further, and describe an improved discretization structure which removes the non-linearity of the light-output relation, and enhances matrix condition. In Chapter 8 I will present much better unfolding results for the EJ309 and EJ315[xvi], with finely-structured neutron spectra measured alongside TOF data for reference. Spectral features on the order of 100-keV wide will be resolved, indicating a substantial improvement over unfolding results found in the literature.

[xvi] Unfortunately, data for the trials in Chapter 8 were not taken with EJ299-33.

References

[1] S. A. Pozzi, S. D. Clarke, W. J. Walsh, E. C. Miller, J. L. Dolan, M. Flaska, B. M. Wieger, A. Enqvist, E. Padovani, J. K. Mattingly, D. L. Chichester, and P. Peerani, "MCNPX-PoliMi for nuclear nonproliferation applications," *Nuclear inst. and Methods in Physics Research, A*, vol. 694, no. C, pp. 119–125, Dec. 2012.

[2] C. C. Lawrence, A. Enqvist, M. Flaska, S. A. Pozzi, and F. D. Becchetti, "Comparison of Spectrum-unfolding Performance of (EJ315_ and (EJ309) Liquid Scintillators on Measured Cf-252 Pulse-height Spectra," *Nuclear inst. and Methods in Physics Research, A*, vol. 729, no. C, pp. 924–929, Nov. 2013.

Chapter 7
Response-matrix Condition

In Chapter 3 I distinguished between two general ways in which I hope to improve spectrum unfolding results by improving the measurement system:

1) improvements in the condition of detector response matrix

2) improvements in the stability and accuracy of the representation of detector response.

The first category determines the extent to which measurement errors δn in the measured PHS are amplified to produce large errors $\delta\phi$. Improvements in the condition of R may help to dampen this amplification. The second category corresponds to ways in which δn are generated in the first place. In this chapter I consider improvements in category one, while Chapter 8 will cover those in category two.

Table 7.1 lists some of the factors that affect the condition of R, along with some possible improvements. The broader features are largely governed by the scattering kinematics and statistics inside the active detector volume, and this is where deuterated detectors stand to improve matrix condition [1]-[3], as will be borne out in the comparison between deuterated liquid EJ315 to the hydrogen-based EJ309.

Pulse-height resolution affects the sharpness of features in the matrix, and has a strong effect on matrix condition [4]. Many organic-crystal scintillators, like stilbene and p-terphenyl, can be optimized to have better resolution than liquids. However, these were unavailable to us at the time of these measurements, so I only mention them as a prospect for future improvements. The effect of resolution will be demonstrated in the comparison of the liquid EJ309 and plastic EJ299-33.

Finally, the binning structure used to discretize the response matrix is an important factor governing matrix condition, and this is driven by competing interests (see Chapter 3). On one

hand, we want sufficient number of rows to "reveal" the structure of the matrix, but this faces diminishing returns due to the broadness of the features. On the other hand, we will always be dealing with finite statistics, and a finer binning structure spreads the limited event counts into more bins, while coarser binning better manages counting statistics. While typical spectroscopy applications divide data into evenly-spaced bins, I find that the best balance is struck by conforming bin width to the scale of the features in the matrix, which varies with pulse height. This variation is due mainly to the nonlinear light-output relation, which tends to compress features in the low pulse-height region. It can be overcome with a novel discretization structure which conforms the bin width to the differential of the light-output relation. This creates more narrow bins in the low-pulse-height region - where typical PHS have abundant counts and features are compressed - and wider bins for higher pulse-height regions where counts are typically scarce and features are more spread out.

TAB. 7.1. (reproduced from Tab. 3.1) Attributes of detector pulse-height response that effect the condition of response matrix R.

Attribute	Effect on matrix	Proposed improvement
Scattering kinematics	Broad features in matrix	Deuterated detectors to employ backscatter-peaked n-d scattering in place of isotropic n-p scattering
Pulse-height resolution	Sharpness of features in matrix	Some organic crystals can be optimized for superior energy resolution
Discretization scheme	Mutual Independence of matrix rows	Conform pulse-height bin widths to the scale of matrix features

In order to evaluate any improvements achieved by altering these factors, we need a way of evaluating matrix condition. Unfortunately, the condition number - defined as the ratio between the largest and smallest singular values of R - will be too large to calculate for any of our matrices. Instead, we follow Matzke et al., and note that matrix condition is related to the rate of decrease of the descending singular values of R [4]. This can be represented visually be plotting the ratio r_p between the pth singular value σ_p and the largest singular value σ_{max}:

$$r_p = \frac{\sigma_p}{\sigma_{max}}.$$ (7.1)

While Matzke and others note the number of singular values for which r_p is greater than some limit - commonly chosen as $r_p > 10^{-4}$ - here I will simply point to the region $10^{-4} < r_p < 10^{-3}$.

7.1 Discretization structure: light-output-conformal versus linear pulse-height binning

In Chapter 6, matrices for EJ309 and EJ315 were presented with 100-keV energy bins and 50-keV pulse-height bins. This is far from optimal: much of the pulse-height structure for low-energy neutrons is engulfed within the large pulse-height bins at the low-end of the pulse-height axis. Using narrow pulse-height bins can uncover this structure, but spreads detected counts - which are scarce in practical measurements - into more bins, leading to larger relative Poisson error δn_{Poiss} in the resulting PHS n_{obs}, which is in turn amplified in the unfolding process.

The "separation" between features in the response matrix R is governed by the nonlinear light-output relation $L_{scint}(E_p)$, which tends to compress features in the low-energy and low-pulse-height regions of R. An improved discretization structure is described here which removes this nonlinearity by conforming the pulse-height bin width to be proportional to the mean differential of the light output relation $L_{scint}(E_p)$ as averaged across each light-output bin:

$$\Delta L_i^{(conf)} \propto \left\langle \frac{dL_{out}}{dE_{dep}} \right\rangle_{\Delta L_i}.$$ (7.2)

The improvement is most prominent for the deuterium-based EJ315, because the back-scatter "ridge" can be shifted onto the diagonal of the matrix. A light-output-conformal binning procedure for deuterated detectors is as follows (see Fig. 7.1):

- begin with bin edges for the desired E_n binning, say

$$E_i = 0, 100 \text{ keV}, 200 \text{ keV}...$$ (7.3)

- multiply each bin edge by 8/9 to account for the backscattering energy transfer fraction

$$E_i^{(bs)} = \frac{8}{9} E_i \qquad (7.4)$$

- insert each bin edge into the light-output relation (see Eq. 5.4 of Chapter 5)

$$L_i^{(conf)} = A \cdot E_i^{(bs)} + B(1 - e^{-C \cdot E_i^{(bs)}}) \qquad (7.5)$$

to yield the bin edges of the conformed binning $L^{(conf)}$. Equation 7.5, by the definition of mean slope across an interval, enforces the desired proportionality expressed in Eq. 7.2. Of course, with unfolding this binning is to be used for the pulse-height binning of the matrix R, as well as the measured PHS n_i from which ϕ_j are to be unfolded. A similar procedure can be used for hydrogen-based detectors, except the second step is omitted, since the maximum energy transfer for n-p scattering is the total incident neutron energy E_n.
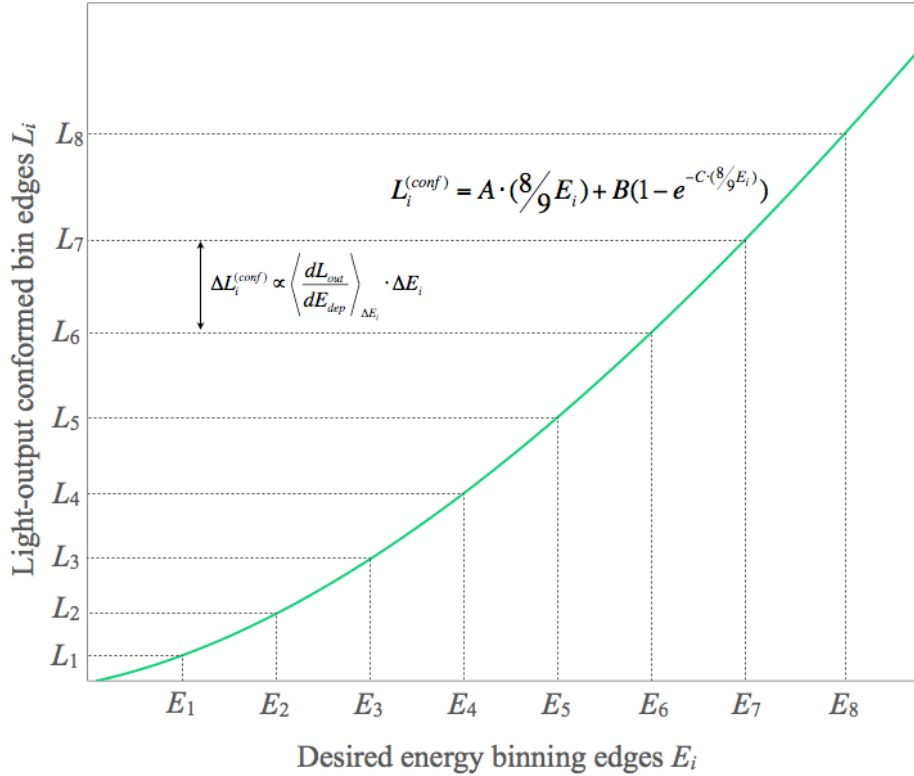
FIG. 7.1. Conformal binning procedure outlined in Eqs. 7.3 - 7.5, designed to remove the non-linearity of the light-output relation. Bin width of each pulse-height bin is made proportional to the mean differential of the light-ouptut relation (see Eq. 5.4) across the bin.

The effect of this binning structure on the shape of the response matrix is shown in Fig. 7.2. The top half of Fig. 7.2 shows the EJ315 response matrix as it was discretized in Chapter 6, with evenly-spaced 50-keVee-wide energy bins, while the bottom half shows an EJ315 matrix constructed from the same data, but with light-output-conformed bins. While the back-scatter-ridge in the linearly-binned matrix is curved and compressed due to the nonlinear light-output relation $L_{scint}(E_{dep})$, in the conformally-binned matrix it is located straight along the matrix diagonal.

Since the bin-width is related to the differential of the non-linear light-output relation, detector response is 'stretched out' across more bins over the low-pulse-height region; over the high-pulse-height region, it is 'compressed' into fewer bins. This is quite convenient considering the statistical challenges of typical measured PHS: for virtually all continuous neutron spectra of interest, the bulk of pulses are in the low-pulse-height region, while in the high-pulse-height bins data are much more scarce. This advantage is borne out in Fig. 7.3, which compares low-E_n' columns for linear- and conformally-binned matrices for EJ315. Much low-pulse-height structure is hidden for the linear-binned matrix, as nearly all columns peak in the first bin. Our conformal binning uncovers this information, so that the sensitivities to each energy group are located in a different pulse-height bin. This reduces the ambiguity in low-energy response from our detector, and may be particularly useful for neutron spectroscopy of weapons-relevant sources, from which most neutrons have energies in this region.
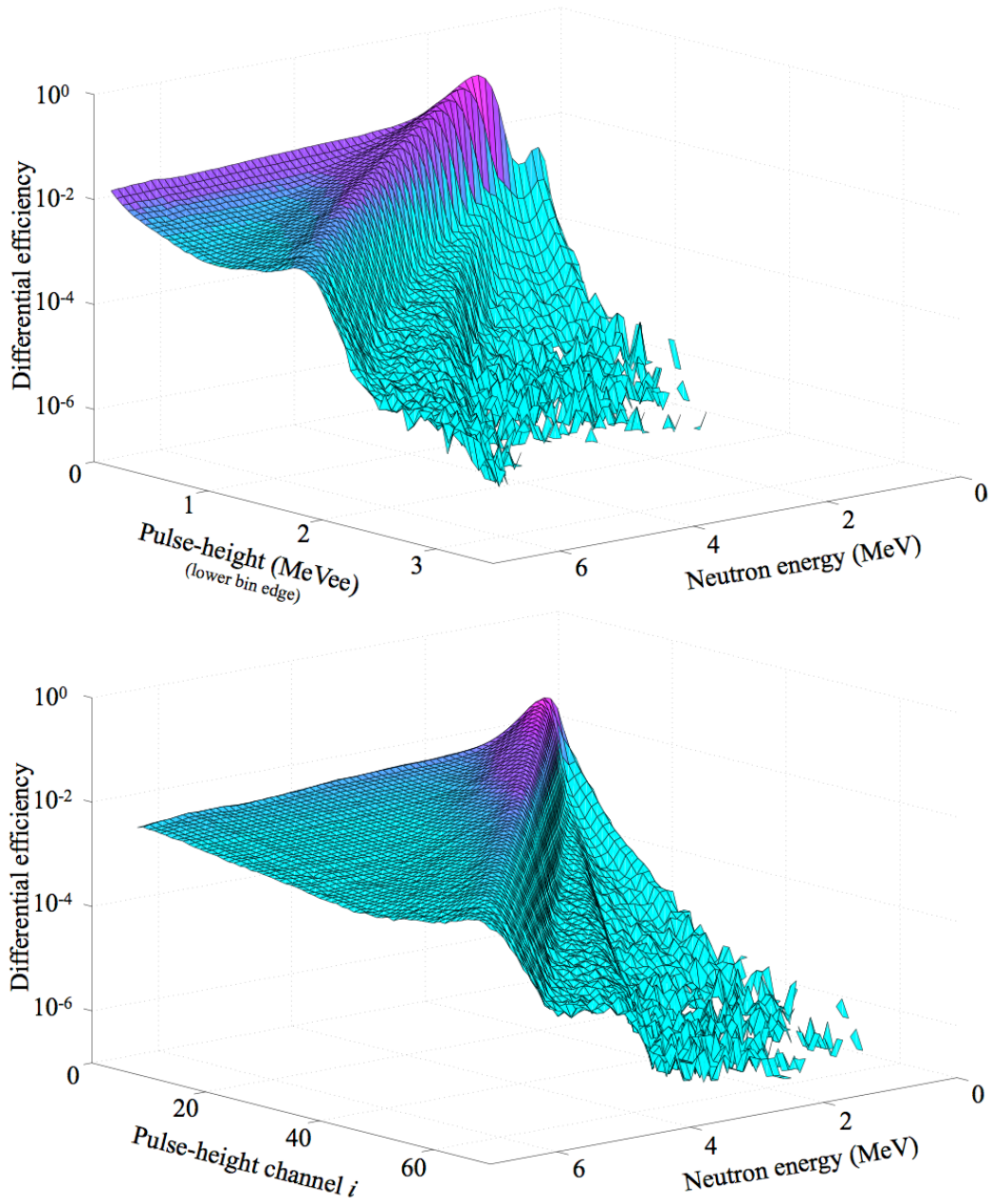
FIG. 7.2. Response matrices of the deuterated EJ315, discretized with evenly-spaced 50-keVee pulse-height bins (above), and with the light-output-conformed binning described in Eqs. 7.3-7.5 (below). The nonlinearity of the light output relation is removed with the conformal binning, improving matrix condition
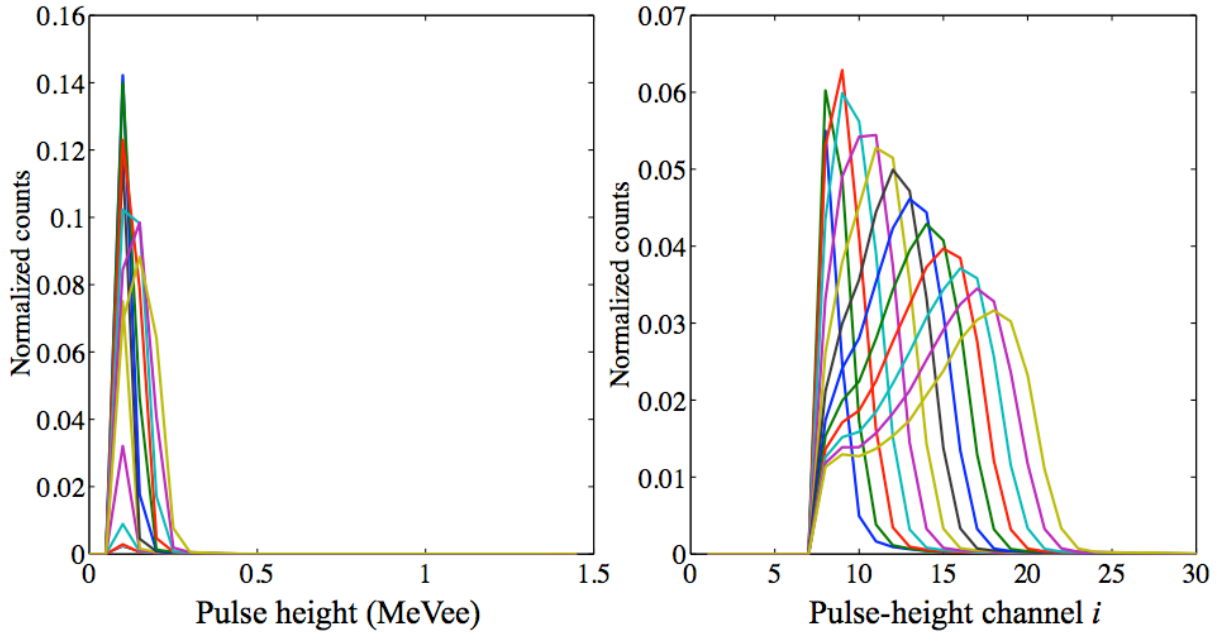
FIG. 7.3. Comparison of low-energy columns of the EJ315 response matrix with evenly-spaced pulse-height bins (left) and light-output-conformed bins.
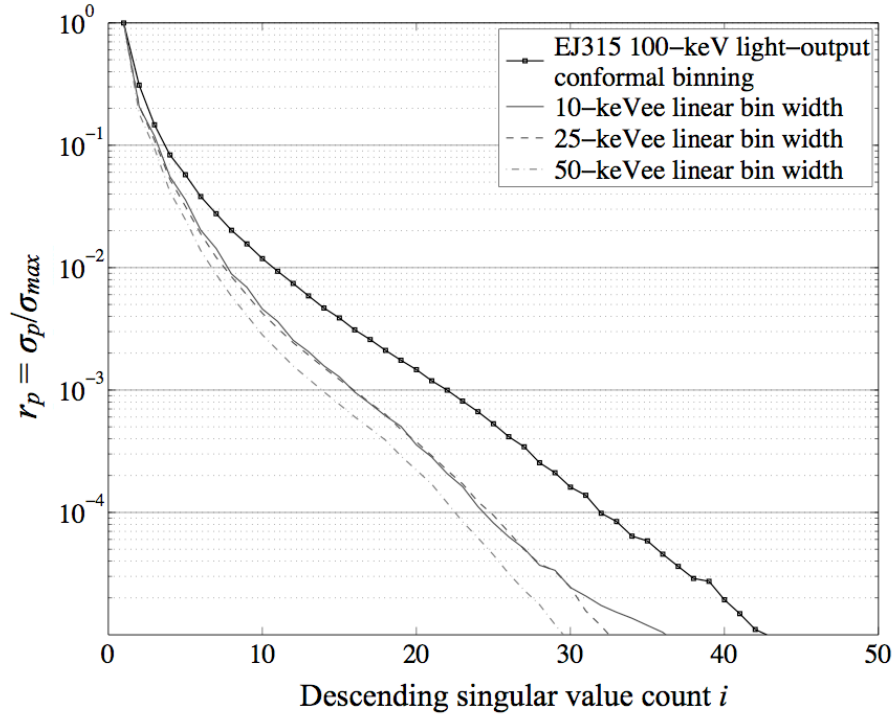
FIG. 7.4. Matrix condition analysis for the EJ315 matrix discretized with the light-output-conformed binning described in Eqs. 7.3-7.5 (bold curve), compared to evenly-spaced bins of different bin widths.

Figure 7.4 shows a condition analysis for the EJ315 with four different discretization schemes. The conformal binning (bold curve) is compared to evenly-spaced binnings of several bin widths, approaching the width of the smallest bins in the conformal scheme. For any given limit for r_{lim} over the region $10^{-4} < r_{lim} < 10^{-3}$, the conformally binned matrix has a considerable advantage in the number of singular values for which $r_p > r_{lim}$ over each of the linearly-binned matrices.

7.2 Scattering kinematics and energy resolution

Figure 7.5 shows selected columns from the response matrices measured for EJ309 (top), EJ299-33 (center) and EJ315 (bottom). Each column corresponds the the PHS expected from mono-energetic neutrons of the corresponding energies. I have used the light-output-conformed discretization structure described in Section 7.1, with the light-output relations reported in Chapter 5. The columns from the EJ315 contain prominent back-scatter peaks, while those from the EJ309 are generally flat, with the exception of some double-scatter structure. Due to the poorer resolution of EJ299-33, the edges of the PHS are much more blurred than those for EJ309.

Figure 7.6 shows the condition analysis for both matrices. For any given limit r_{lim} over the region $10^{-4} < r_{lim} < 10^{-3}$, EJ315 gives 25-30% more eigenvalues for which r_p surpasses that limit than does the EJ309 matrix. This implies a modest but significant improvement in matrix condition for EJ315 over EJ309, similar to that observed in the previous chapter. A significant disadvantage is seen for the EJ299-33 due to the lower resolution of the plastic relative to the liquids.
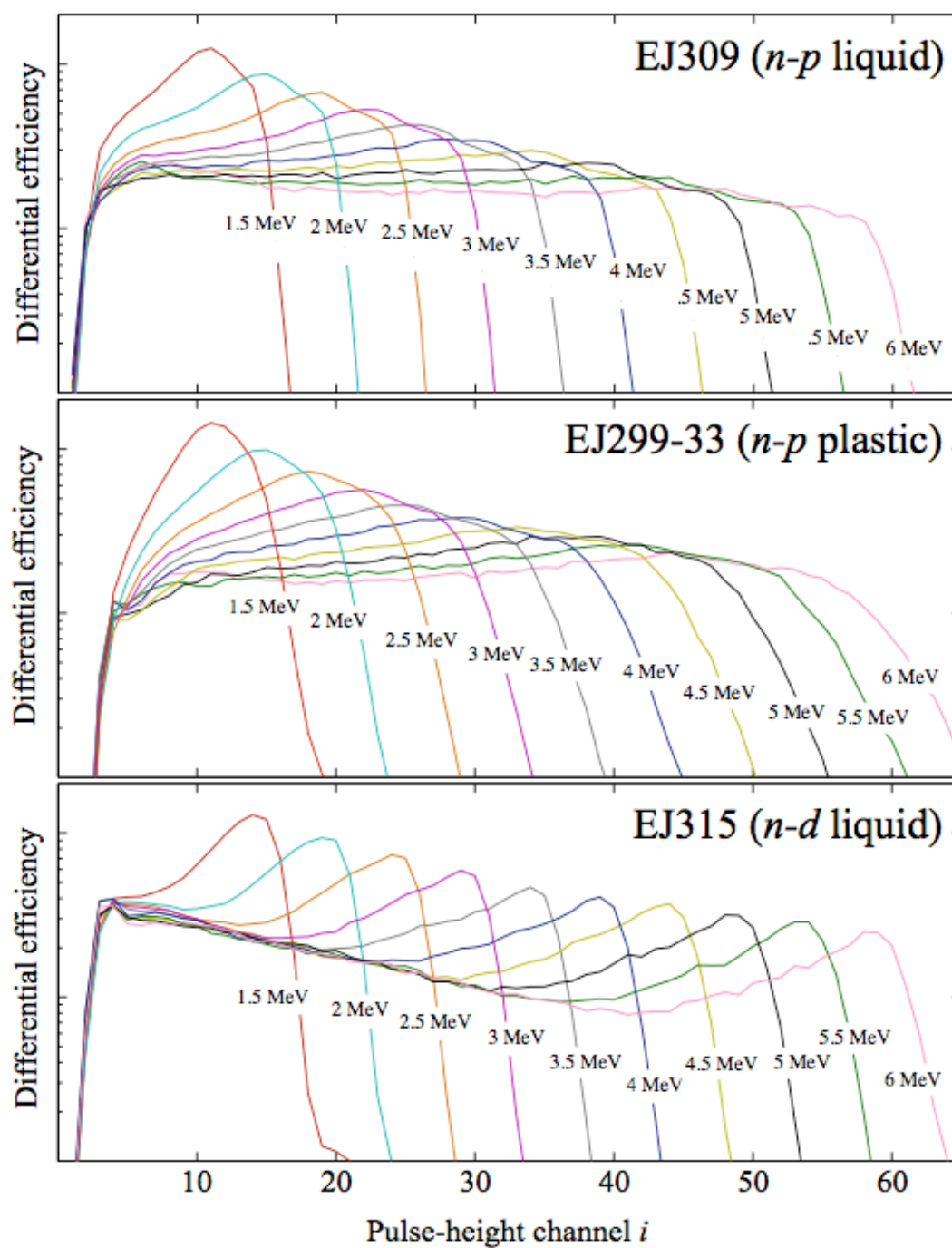
FIG. 7.5. Selected columns of measured response matrices for the hydrogen-based liquid (EJ309; top) and plastic (EJ299-33, center), and the deuterium-based liquid (EJ315; bottom).
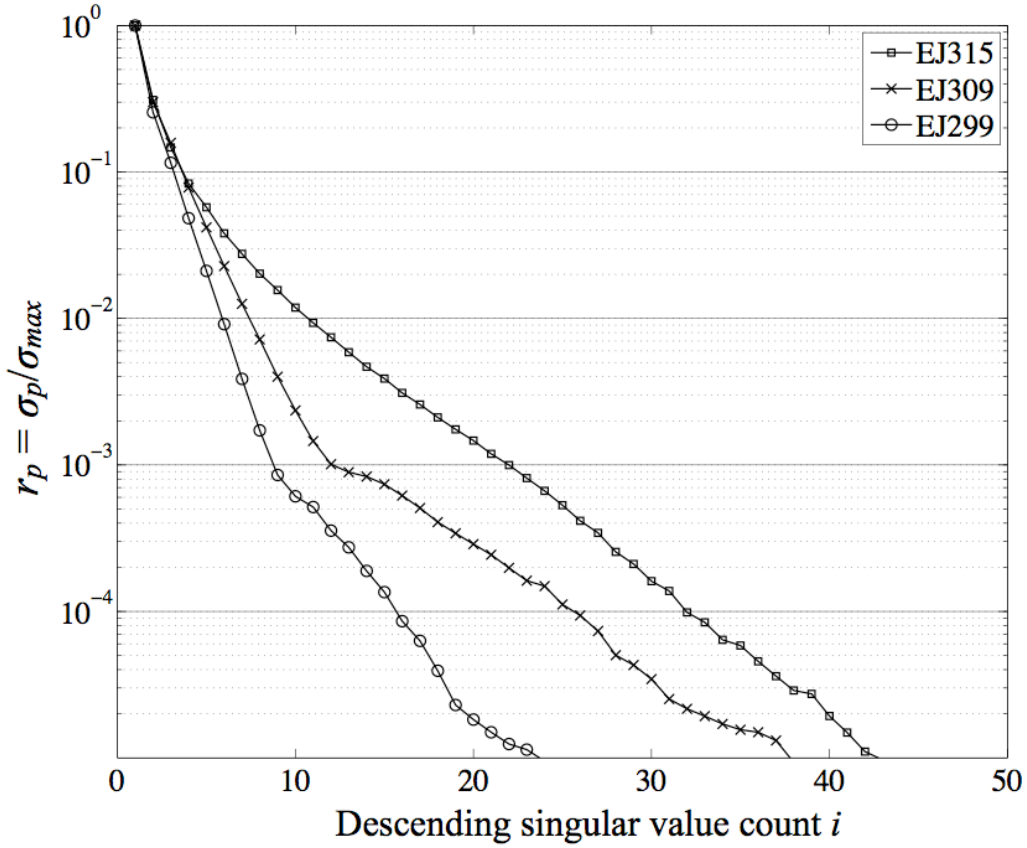
FIG. 7.6. Analysis of response matrix condition for the hydrogen-based liquid (EJ309) and plastic (EJ299-33) and the deuterium-based liquid (EJ315).

7.3 Remarks

I have investigated multiple ways for improving the condition of response matrices R of organic scintillators. First, it was found that matrix condition can be improved by conforming the pulse-height bin widths to the scale of features in the matrix, which is a variant across the pulse-height scale due largely to the nonlinearity of the light output relation $L(E_{dep})$. A novel discretization structure was described which stretches the pulse-height bins such that their widths are proportional to the mean slope dL/dE_{dep} of the light output relation across each bin. This was shown to improve the condition of the response matrix for the deuterated EJ315, and similar improvements can be derived from the hydrogen-based matrices. Then, two important aspects of detector performance were investigated: scattering kinematics of the dominant detectable neutron interaction, and pulse-height resolution. Since the deuterated EJ315 relies on the back-scatter-

peaked *n-d* scattering, the matrix condition is improved by the back-scatter peak in the response, relative to the hydrogen-based detectors. The poorer resolution of the plastic EJ299-33 resulted in a significant degradation of matrix condition. These demonstrations suggest a significant impact of these performance aspects on the unfolding capabilities of organic scintillators.

A few comments should be made about the relevance of the comparison between EJ309 and EJ299-33, which was made in lieu of a more desirable comparison with high-resolution crystal scintillators like p-terphenyl or stilbene. Unfortunately, the crystals available for the measurements presented here were optimized for PSD performance rather than resolution and light output when compared with EJ309. The comparison made between EJ309 and EJ299-33 was intended to highlight the importance of resolution for matrix condition. It is conceivable that the benefits of *n-d* scattering can be combined with the higher resolution of crystals by creating deuterated versions of high-resolution crystals. For instance, Brooks et al. have investigated the spectroscopic capabilities of deuterated anthracene over the energy range from 5 to 30 MeV, and in fact devise a further improvement on spectral performance by selecting back-scatter events using special PSD techniques. It is not clear whether this is possible over the energy range of interest for arm-control applications, but the possibility of deuterated crystals offers a promising direction for future research along the lines suggested in this thesis.

References

[1]   M. Ojaruega, F. D. Becchetti, A. N. Villano, H. Jiang, R. O. Torres-Isea, J. J. Kolata, R. J. Goldston, and C. C. Lawrence, "Evaluation of large deuterated scintillators for fast neutron detection (E=0.5–20MeV) using the D(d,n)3He, 13C(d,n) and 27Al(d,n) reactions," *Nuclear inst. and Methods in Physics Research, A*, vol. 652, no. 1, pp. 397–399, Aug. 2010.

[2]   C. C. Lawrence, A. Enqvist, M. Flaska, S. A. Pozzi, and F. D. Becchetti, "Comparison of Spectrum-unfolding Performance of (EJ315_ and (EJ309) Liquid Scintillators on Measured Cf-252 Pulse-height Spectra," *Nuclear inst. and Methods in Physics Research, A*, vol. 729, no. C, pp. 924–929, Nov. 2013.

[3]   F. D. Brooks, "Development of organic scintillators," *Nuclear inst. and Methods in Physics Research, A*, vol. 162, pp. 477–505, Jun. 1979.

[4]   M. Matzke, "Unfolding Procedures," *Radiation Protection and Dosimetry*, vol. 107, no. 1, pp. 155–174, Dec. 2003.

Chapter 8
Spectrum Unfolding with
Measured Trial Spectra

In this chapter I present unfolding results from measured trial spectra with the hydrogen-based EJ309 and the deuterium-based EJ315. The measurements are taken with the same experimental arrangement, described in Chapter 4, as was used to measure the response matrices. This allows the use of TOF to calculate reliable reference spectra for comparison with unfolded solutions. Finely-structured neutron spectra of relevance for arms-control applications were measured for both detectors. The trial spectra contain features on the scale of 100-keV in width, and resolving these from scintillator PHS would represent a considerable advance in spectrum-unfolding capabilities. In the current literature, spectral features finer than 250-keV wide are not resolvable through unfolding, especially with standard hydrogen-based liquids.

8.1 Accelerator-based measurements for spectrum-unfolding trials

Trial neutron spectra were created by passing the beam of continuous-spectrum neutrons from ^{11}B(d,n) (see Fig. 4.7) through a series of low-Z materials that are relevant for warhead verification. Conventional high explosive used to induce implosion is composed mainly of hydrogen, carbon, nitrogen and oxygen. Beryllium metal is commonly used as a neutron reflector in modern fission weapons. While the cross section of hydrogen is largely featureless, the other four elements all have distinctive features in their cross sections that will add fine structure to the otherwise smooth spectrum of neutrons from the beam. Tab. 8.1 lists the attenuating materials used for each trial measurement, and they are shown in Fig. 8.1.

TAB. 8.1. Attenuator materials chosen for trial measurements, along with approximate thicknesses.

Elements of interest	Materials used	Thickness (cm)
^1H, ^{16}O	Distilled water	5.2 (+/- 0.1)
^{Nat}C	Graphite	3.8 (+/- 0.1)
^{14}N	Liquid nitrogen	12 (+/- 1.5)*
^9Be	Beryllium metal	3.8 (+/- 0.05)

* Liquid nitrogen contained in thin-walled cylindrical glass dewar
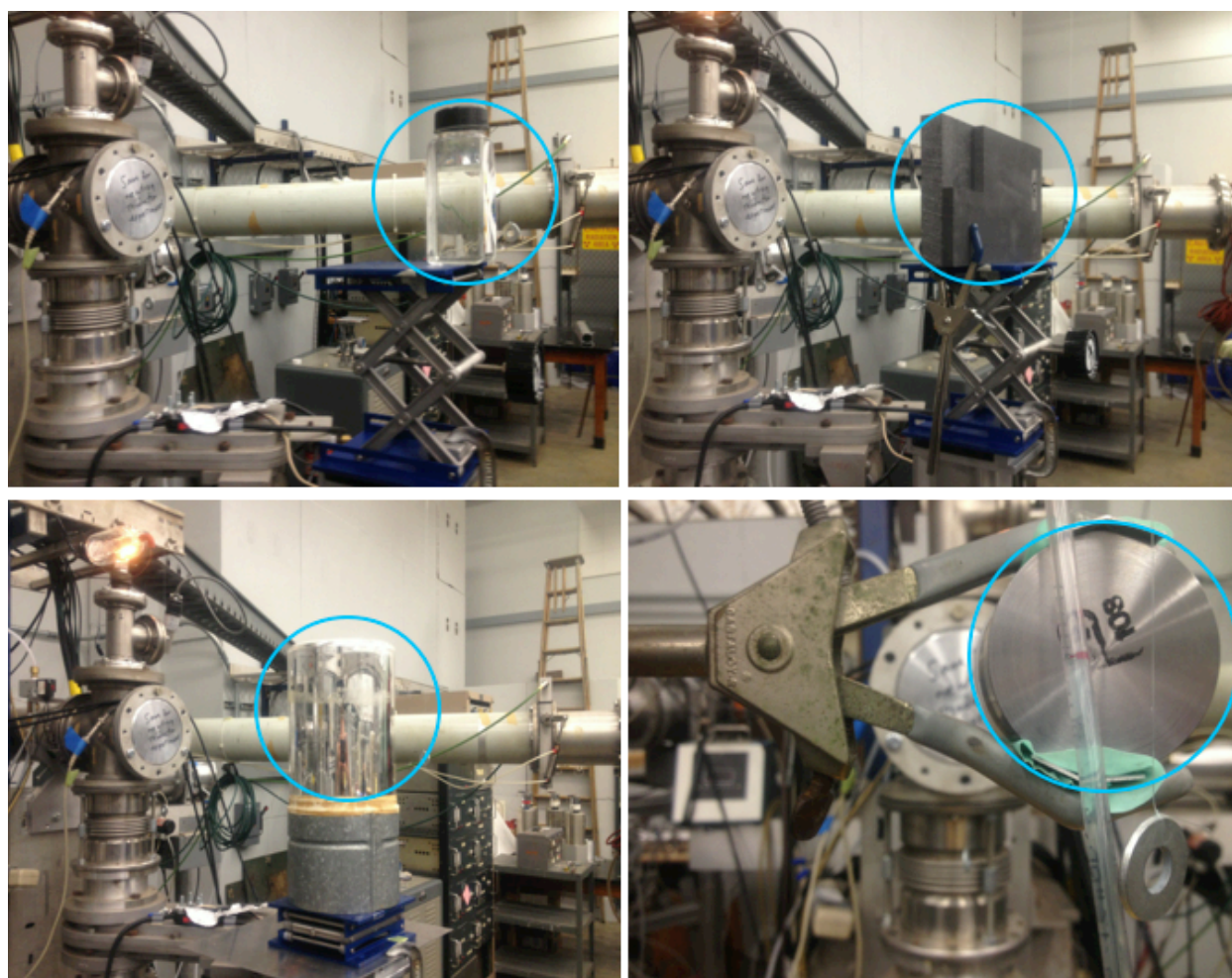
FIG. 8.1. Attenuators used to create finely-structured spectra for the unfolding trials. Tap water (upper left), graphite (upper right), liquid nitrogen (lower left) and beryllium metal (lower right) are materials contained in modern nuclear-weapon components.

It should be noted that these measurements are preceded by those of Chichester et al. who measured simular spectra using a Cutler-Shalev ^{3}He spectrometer. However, the ^{3}He has extremely low detection efficiency, on the order of 10^{-4} - 10^{-3}, and this represents a significant disadvantage. Also, no unfolding was performed on the pulse-height spectra [1].

All measurements are taken with the same experimental arrangement as that used to measure the response matrices, and TOF data are taken alongside the pulse-height data used for the unfolding trials. Separate measurements were taken with each attenuator and with each detector (EJ309 and EJ315) for a total of eight trial measurements. Each trial measurement is taken for four hours, with equal primary beam current for each sample.
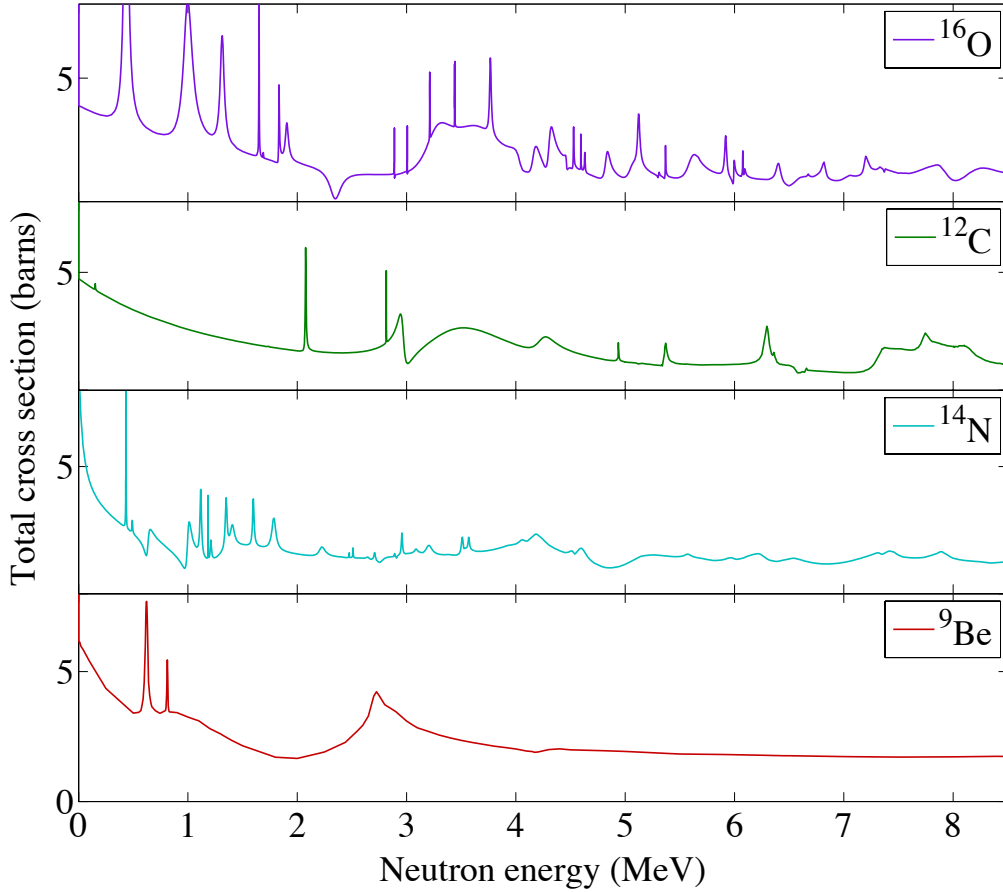
FIG. 8.2. Total neutron-scattering cross sections for the low-*Z* elements contained in each of the attenuators used for creating trial neutron spectra (ENDF/B_6.1 [2]).

Figure 8.2 shows the total neutron interaction cross sections of the relevant elements (ENDF/B_6.1 [2]). The location of the attenuating material was approximately 5 meters away from the detector, so that the scattered neutrons were minimized due to solid-angle attenuation. Thus, the cross sections shown in Fig. 8.2 can be treated as elimination cross sections to a very good approximation for this geometry.

8.2 Diagnostics from time-of-flight data

Table 8.2 (reproduced for convenience from Tab, 3.2) lists some of the sources of perturbation δn that, when amplified by an ill-conditioned matrix, distort the solution spectrum ϕ_{unf}. The list is not claimed to be exhaustive. Poisson variance in the PHS should be singled out amongst the rest as likely the ultimate limitation on unfolding performance. All radiation measurements have Poisson error that is related to the number of quanta detected, and hence to the limited commodity of measurement time. I distinguish here between Poisson variance in the PHS, versus that in the response matrix, for practical reasons. The response matrix only needs to be measured once for a given detector, so it is practical to make this measurement of sufficient duration that the attendant Poisson variance in the resulting matrix is negligible. Any PHS data taken in the field is likely subject to time constraints, so there will be non-negligible Poisson error. The degree to which this error is amplified by the matrix will give us a sort of "upper limit" on the unfolding performance we can hope to achieve with a given deployable detection system. We will look at this more in depth in Section 8.4.

TAB. 8.2. (reproduced from Tab. 3.2). Sources of perturbation in measured pulse-height spectra that contribute to error in unfolded spectra.

Source of perturbation	Likely improvement for field
Poisson variance in PHS	N/A
Inaccuracies in response matrix	Detector with directly-measured response matrix
Shifts in PMT gain	Direct optical input to scintillator cell for real-time calibration during measurement
Shifts in PSD discrimination threshold	Eljen proprietary additive to improve PSD performance [3]; systematic placement of PSD discrimination curve [4]

There is good reason to believe the other three sources can either be removed, or dramatically improved, in a future deployable system, by incorporating currently-available technologies. The first perturbation listed is associated with inaccuracy of the response matrix. As described in Chapter 3, most spectrum unfolding studies reported in the literature use either simulated matrices, or measured matrices provided with the unfolding code used. While these may be sufficiently accurate to unfold the broad features of spectra for dosimetry applications, they are likely insufficient for our purposes. Simulation of detector response is imperfect, and often does not account for performance attributes such as gamma-ray and neutron misclassification by PSD. Also, simulation often only models the detector itself, while real measured data is governed by the PMT and data acquisition electronics as well. In order to achieve the results that would likely be required for treaty verification, the entire measurement system should be characterized using the methods described in Chapters 4-6.

Gain shifts in the PMT often occur during a measurement, and can broaden the detector resolution, or shift the response altogether. Gain calibration during field measurements should be identical to that during the measurement of the matrix, and resulting shifts can distort the unfolded results. However, it is easy to imagine how these shifts can be prevented in a field-able system. Scintillator housings are available with optical ports for introduction of a standardized light pulse. This can be carried out periodically during a measurement for real-time calibration data, and gain adjustment can even be automated.

The final source of perturbation listed is related to PSD performance. There is always some misclassification of neutrons and gamma-rays at the low end of the pulse-height spectrum. In principle, this is included in a measured response matrix, but if the discrimination threshold shifts (to be precise, more often the detector response shifts with respect to a stationary threshold), then the detector response no longer matches that represented by the response matrix. This can be addressed from two angles. First, there is a proprietary additive offered by Eljen which dramatically improves PSD separation, and this would in turn reduce the misclassification rates themselves. While we have investigated this additive and confirmed the improvement in PSD [3], it was not used for the measurements presented here[xvii]. With this improvement, misclassification may not even be an issue for spectrum unfolding. Second, the PSD discrimination threshold is usually placed by visual inspection based on the features in the PSD plot (see Fig. 2.7), and this is a sensitive process that can affect the shape of the final PHS. We are currently investigating systematic ways to place the discrimination threshold relative to the features in the PSD plot, such that if the features move from measurement to measurement, the PSD gate would be placed in an identical location relative to those features [4]. Methods for systematic PSD-gate placement will be reported in a coming publication. These developments taken together, it is then reasonable to expect that PSD performance can be significantly stabilized in a fieldable system using current technology, together with these new techniques.

While these useful features are not included in the detection system used for the present measurements trial, we can use the TOF data taken alongside the trial pulse-height data to monitor and correct the time-dependent shifts in detector response. Let R_{model} specify the response matrices presented in Chapters 6 and 7, which will be used here for unfolding. For each trial measurement taken, an independent response matrix R_{trial} can be constructed from the attendant TOF data, the same way R_{model} was constructed in Chapter 6. In principle, if no shifts in detector performance have occurred, the two matrices R_{model} and R_{trial} should be identical to

---

[xvii] The PSD additive would have complicated the direct comparison between hydrogen-based and deuterated scintillators.

within Poisson variance[xviii]. Discrepancies between the two can reveal some of the shifts described above.
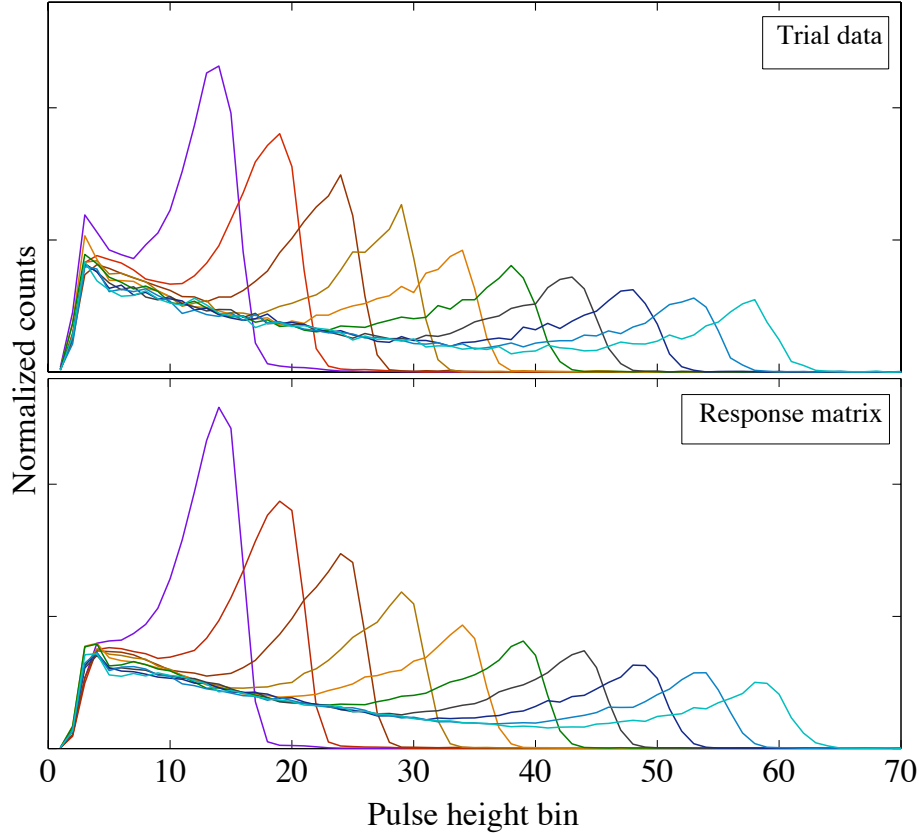
FIG. 8.3. Shifts in PMT gain and PSD performance during the trial measurements can be monitored using TOF-gated pulse-height spectra. Normalized, TOF-gated PHS from a trial measurement with the EJ315 (above) are compared to the columns of the response matrix for EJ315, indicating shifts in PMT gain and PSD performance.

An example is shown in Fig. 8.3. Selected columns of the EJ315 response matrix R_{model} are shown (below), along with the same columns from R_{trial} constructed from the data taken with the water attenuator. First, note that the columns of R_{trial} are shifted slightly downward in pulse height, relative to the columns of R_{model}. This indicates a shift in PMT gain that occurred during the trial measurement. In addition, the low-pulse-height bins of R_{trial} are ramped up slightly, while those in R_{model} are not. This indicates a shift in PSD performance that was caused by the shift in PMT gain. The neutron and gamma-ray distributions in the PSD plot were therefore

_____

[xviii] This is true as long as neutrons of all the energies represented in R_{model} are included in the trial spectrum. This is the case for all trial measurements used here.

shifted by a small amount relative to a stationary discrimination gate, such that more gamma-ray pulses at the low-pulse-height end were misclassified as neutrons. The amount of shift was imperceptible from the PSD plot, but moving the discrimination gate in small increments lead to the removal of the ramp shown in Fig. 8.3.

Performance shifts of these sorts were corrected for the trial PHS used in these trials so that the unfolding results represent the true unfolding potential of the detectors that could be achievable if the true detector response is accurately represented by the response matrices used.

8.3 Unfolding results

Unfolding of each trial spectrum is performed using the conjugate gradient method on Eq. 3.16

$$(R^\dagger R + \lambda I)\phi = R^\dagger n. \tag{8.1}$$

Regularization parameters λ are chosen using the *L*-curve method [5], [6]. The light-output-conformal discretization schemes introduced in Chapter 7 are used, with 100-keV-wide energy bins. Each unfolded result, along with the corresponding TOF-calculated reference spectra, are presented in Fig. 8.4. As expected, the prominent peaks in the cross-section curves correspond to valleys in the TOF references where neutrons of those energies are more strongly attenuated. The unfolded spectra from both detectors follow the broad features of the references quite well, especially considering the fine energy binning used. However, the EJ315 appears to better preserve the finer structure, and is more stable with respect to the oscillatory error component characteristic of unfolded spectra. Thus, we continue to see a modest but significant improvement for the deuterated EJ315 over the hydrogen-based EJ309, as seen in previous chapters. It is also clear that, without accurate TOF reference spectra for comparison, it would be very difficult to distinguish between genuine well-preserved spectral features, and features added by the oscillatory error component. The TOF reference confirms that much of the jagged structure in the unfolded spectra, particularly in the EJ315 case, is genuine spectral structure that is preserved through the unfolding process.
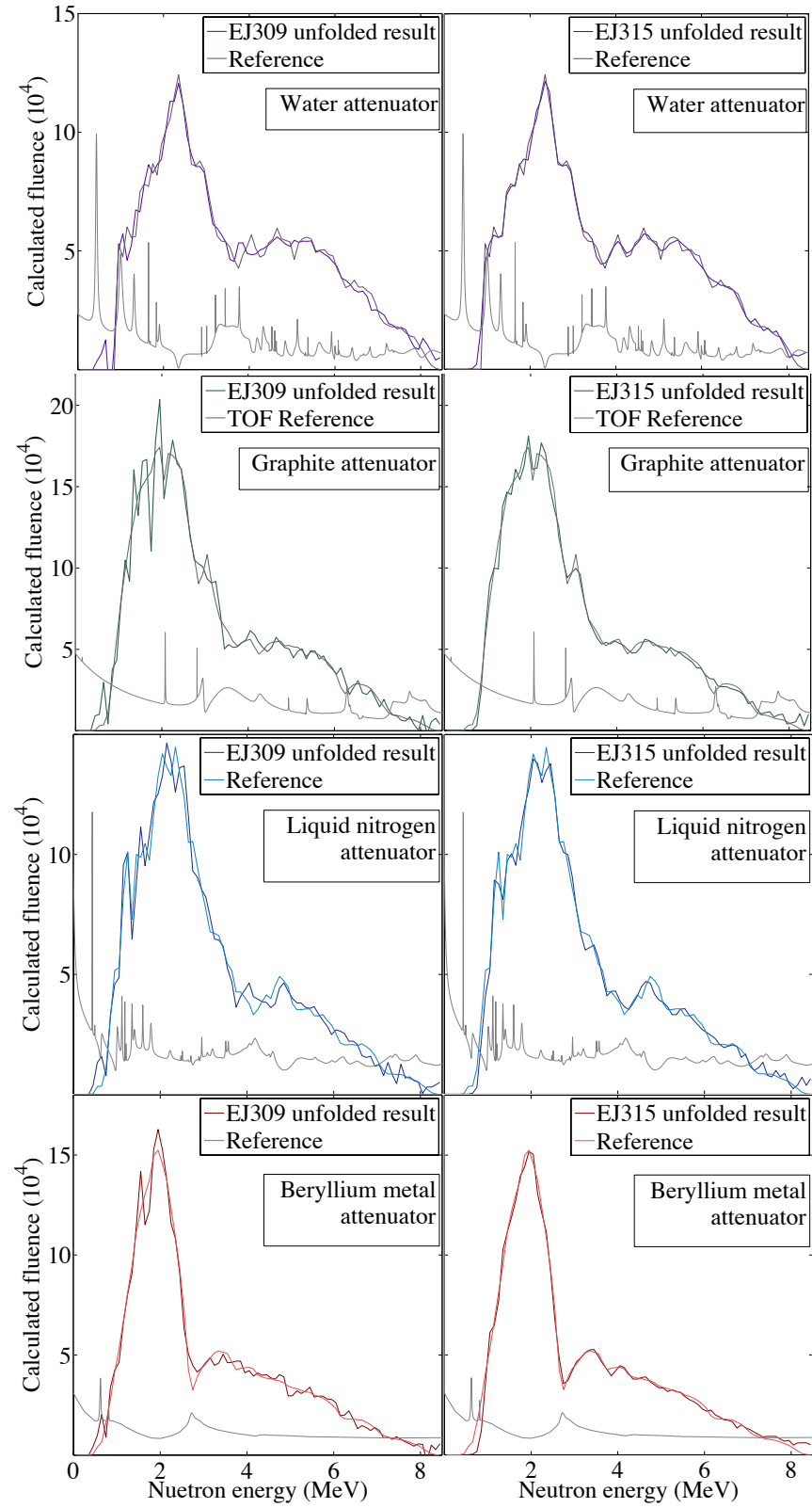
FIG. 8.4. Unfolding results from trial measurements with EJ309 (left) and EJ315 (right), using the attenuators listed in Tab. 8.1. TOF reference and total-interaction cross sections are included in each figure.

8.4 The effect of Poisson variance on unfolded spectra

I have argued that Poisson variance (i.e. counting statistics) in the measured pulse-height spectrum n is probably the limiting factor on the stability of unfolded solutions for a given detector, and with a given measurement duration. The question arises: how stable are the results presented in section 8.3 to Poisson variance? If we took the same measurements a second or third time, would the same spectral features be preserved? In order to answer these questions, we can create an array of Poisson-variant PHS $n^{(p)}$ associated with a given measurement $n^{(trial)}$, where the number of counts $n_i^{(p)}$ in each pulse-height bin i is drawn from a Poisson distribution with mean equal to the measured counts element $n^{(trial)}$:

$$P(n_i^p) = \frac{(n_i^{(trial)})^{n_i^p} e^{-n_i^{(trial)}}}{n_i^p!} . \tag{8.2}$$

After unfolding each of the Poisson-variant PHS $n^{(p)}$, we create a corresponding array of solutions $\phi^{(p)}$, on which statistical analysis can be carried out. This process was carried out on the water-attenuated measurements with both detectors (Fig. 8.4 top row). Figure 8.5 shows multiple overlapped unfolded results $\phi^{(p)}$ form Poisson-variant PHS $n^{(p)}$ for both EJ309 (left) and EJ315 (right). The top row of plots represent ten trials each, while the bottom row represents a heat map corresponding to 10^3 Poisson variant trials each. This provides a good representation of the advantage for the deuterated detector: the features are better preserved for the EJ315 trials, and the band of variance is narrower across the spectrum, indicating higher stability of the unfolded EJ315 solutions to Poisson variance. The standard deviation of fluences in each energy group was 25-30% higher for the EJ309 detector than for the EJ315 detector.
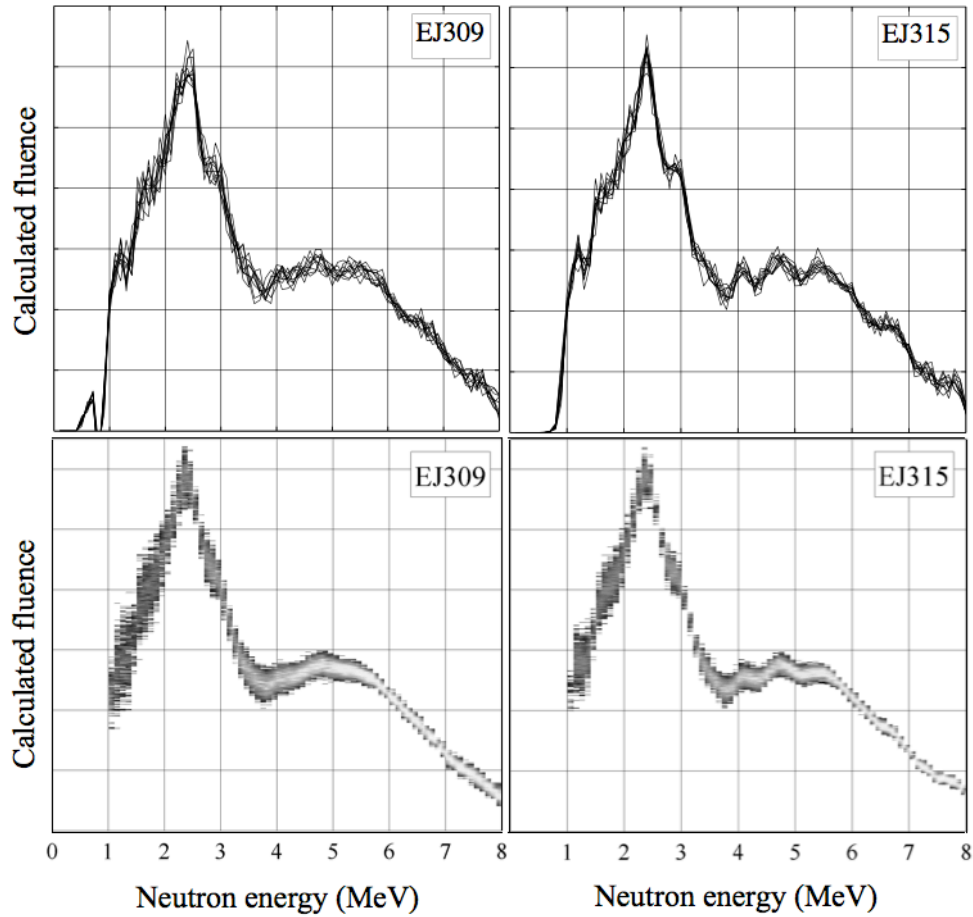
FIG. 8.5. Unfolded results from ten (above) and 10^3 (below) Poisson-variant pulse-height spectra for EJ309 (left) and EJ315 (right).

8.5 Remarks

Unfolded spectra from PHS measured with the hydrogen-based EJ309 and the deuterium-based EJ315 were presented. Trial neutron spectra for the measurements were created by passing the neutrons from $^{11}B(d,n)$ (see Chapter 4) through low-Z attenuating materials commonly found in weapons components, listed in Tab. 8.1. Comparison was made with TOF-calculated reference spectra, verifying the preservation of spectral features as fine as 100-keV in width. This represents a considerable improvement over results found in published literature, which are unable to resolve features narrower than 250 keV in width. The unfolding results for EJ315 are superior to those of EJ309. The capability to distinguish between spectral features caused by different attenuating materials could be useful for future warhead-verification applications.

References

[1]   D. L. Chichester, J. T. Johnson, and E. H. Seabury, "Fast-neutron spectrometry using a 3He ionization chamber and digital pulse shape analysis," *Applied Radiation and Isotopes*, vol. 70, no. 8, pp. 1457–1463, Aug. 2012.

[2]   *Cross-section Plotter*. [Online]. Available: http://atom.kaeri.re.kr/cgi-bin/endfplot.pl. [Accessed: 09-Jun-2014].

[3]   C. C. Lawrence, A. Enqvist, M. Flaska, S. A. Pozzi, and F. D. Becchetti, "Comparison of Spectrum-unfolding Performance of (EJ315_ and (EJ309) Liquid Scintillators on Measured Cf-252 Pulse-height Spectra," *Nuclear inst. and Methods in Physics Research, A*, vol. 729, no. C, pp. 924–929, Nov. 2013.

[4]   J. K. Polack, M. Flaska, A. P. Enqvist, and S. A. Pozzi, "A Computer-aided, Visual Charge-integration Pulse-discrimination Method for Organic Scintillators," presented at the Institute for Nuclear Materials Management, 54th Annual Meeting, Palm Desert CA, 2013.

[5]   P. C. Hansen, *The L-curve and Its Use in the Numerical Treatment of Inverse Problems*. 2003, pp. 1–24.

[6]   P. C. Hansen, "MATLAB Regularization Toolbox," *Numerical Algorithms*, vol. 46, pp. 189–194, Mar. 2007.

Chapter 9
Re-parametrization of the
Unfolding Problem

Thus far, I have approached spectrum unfolding as a task of solving for the fluences ϕ_j of neutrons contained in a series of energy groups j. If the energy range of interest extends up to 15 MeV, and if we want to see sharp spectral features of width on the order of 100-keV, this amounts to ~150 unknown parameters ϕ_j. As we have seen, measured PHS n_i do not contain enough information to constrain this many free parameters, and so we must implement some a priori information to further constrain the problem. This is typically done by including some penalty in the extremized functional by which candidate solutions are evaluated. For the unfolding results presented in Chapter 8, a penalty was implemented against solutions with large oscillations (see Section 3.2.1). However, the oscillatory error from the solution instability has tended to look similar to the genuine spectral features which we want to preserve, so the regularization was used at the cost of dulling sensitivity to these finer features. Indeed, in the case of the hydrogen-based detector, by the time the error components were removed from the solutions, most of the spectral features of interest were as well.

This formulation of the unfolding problem seems natural enough, and its dominance in the literature is motivated by a desire for generality. We would like to be able to take a neutron spectrometer into any environment, and detect any conceivable neutron field without any preconceived notions or commitments. But this desire itself implies an artificial distinction. A clear line is drawn between an object to be known - i.e. the spectrum of neutrons present - and the means by which it can be known - i.e. the detection system. According to this distinction, preliminary knowledge about the detection system (i.e. the response matrix) is accepted as the "data constraint", while preliminary knowledge about the energy spectrum is sanctioned as "a priori information", external to the "data", whose implementation is a regrettable but necessary trespass.

But consider a practical problem like that envisioned for warhead verification. An inspectorate desires to know a series of treaty-relevant parameters τ_l about an enclosed test *object*, and the various radiative and acoustic couplings are the *means* by which these might be known. Here the line of sanction has shifted: no one cares about the neutron or phonon distributions themselves, but about the presence or absence of various attributes that would define the object as a weapons component. In solving the inverse problems associated with warhead verification, we can take this practical shift seriously by incorporating it in our formulation. We can try to write a more direct relationship between our observables n_i and the treaty-relevant parameters τ_j that we desire to know:

$$n_i = f\left(\tau_1, \tau_2 ... \tau_p\right).$$

(9.1)

Here f takes the place of the response-matrix operator, and now it can rightfully contain information that is known about the measurement task. The operator f would take very different form in the warhead-verification scenario than it would for, say, dosimetry applications, even if the same detector was used. But by taking these obvious differences between measurement challenges to heart, we may arrive at a problem with far fewer unknown parameters than if we insisted on treating the spectrum itself as the object of interest.

This chapter will explore the possibility of using a priori information about the measurement task at hand to re-parametrize the unfolding problem, in hopes of arriving at a smaller solution space. I begin by describing how this might take place in the warhead-verification scenario. The possible physical configurations that amount to a genuine nuclear warhead are extremely limited, and involve important symmetries within a localized space. Neutrons emitted from the plutonium pit would pass through concentric shells of neutron-reflecting and high-explosive (HE) material, and they would be spectrally altered by those materials before reaching a surrounding detection system. However, writing down a workable f for this scenario would require an extensive research effort that is beyond the scope of this dissertation. I therefore construct a simplified one-dimensional problem, in which neutrons of a continuous spectrum are passed through an attenuating slab of low-Z materials, as in the

accelerator measurements discussed in the previous chapter. I will write f as a function of the optical thicknesses of candidate attenuating materials, and solve for those thicknesses. This will first be done using the same measured pulse-height data presented in Chapter 8. Then I will perform MCNP-PoliMi simulations in which Watt-spectrum neutrons are passed through slabs of HE, and the neutron spectra seen by the detector are calculated via a surface tally. Trial PHS associated with these simulated neutron spectra will be constructed from measured pulse-height and TOF data. From these trial spectra, the elemental compositions of the simulated HE will be estimated to an accuracy of around 10%. These results illustrate the usefulness of approaching the unfolding problem by focusing on the measurement system itself, and suggest an area of future research on the warhead verification problem.

9.1 Warhead-verification scenario: three-dimensional attenuation problem

While there is some variation in the design of modern fission weapons, the constraints on that variation are fairly severe. A metal core of either plutonium or uranium is imploded by a surrounding arrangement of HE lenses to momentarily produce a super-critical assembly. The essential design challenges are to minimize neutron multiplication prior to detonation to minimize the risk of pre-detonation; maximize the criticality of the imploded assembly to maximize yield efficiency; and to minimize "insertion time", i.e. the time it takes for implosion to bring the assembly into maximum criticality. A few design aspects are key to achieving these aims [1]-[3]:

- Geometrical symmetry - either spherical or ellipsoidal - to ensure maximum insertion speed and density of imploded metal
- Inclusion of some neutron-reflecting layer - typically of beryllium metal - to reflect fission neutrons back into the reacting metal after implosion
- Strict separation between fissile metal - which also decays by alpha emission - and any potential α-n target.
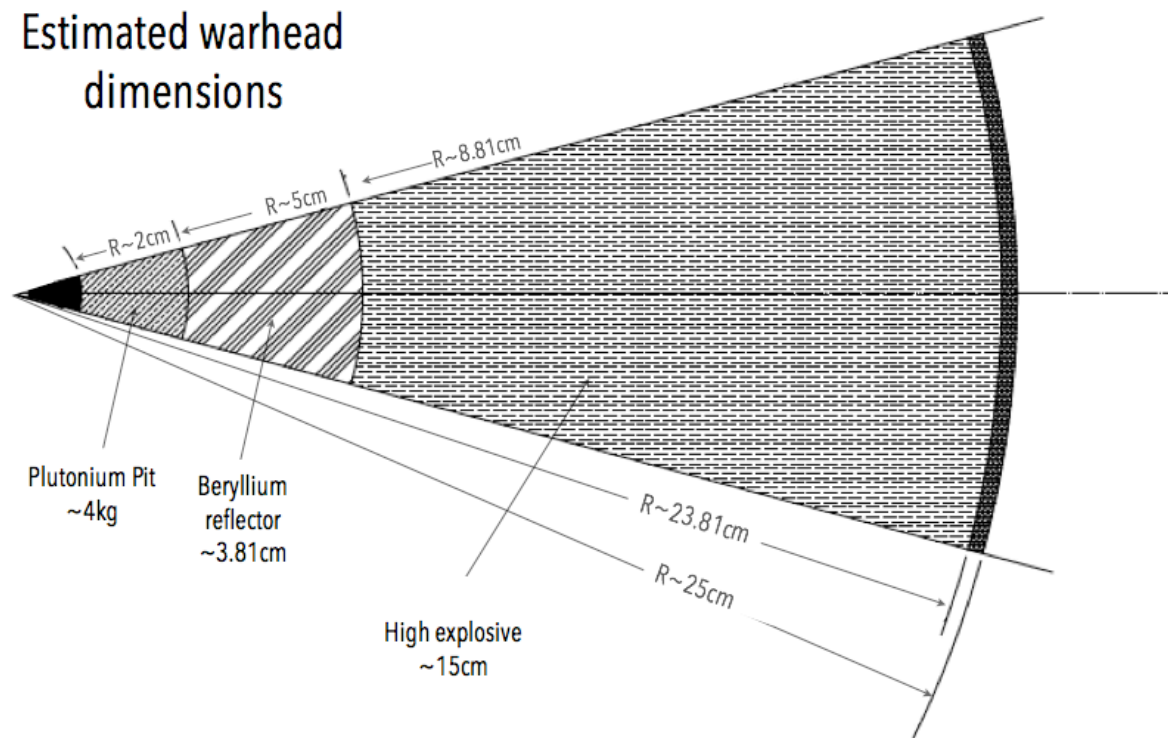
FIG. 9.1. Estimated dimensions of a simplified warhead.

The feats of detonation are to be achieved within an extremely constrained space, in order to facilitate weapon delivery. While highly-enriched uranium will be difficult for passive-assay techniques because it produces very few neutrons, the majority of modern weapons use plutonium because it allows criticality to be achieved with considerably less material. Figure 9.1 shows a representation of a simplified fission device. A plutonium-metal core is contained within concentric spheres of beryllium metal and HE material. While the plutonium used in modern weapons is predominantly of odd-number isotopes, a small amount of ^{240}Pu always remains, which spontaneously fissions to produce neutrons of a well-known Watt spectrum. These must pass through the reflector and HE-lens system, which contain the low-Z elements H, C, O, N and Be. As is seen in Fig. 8.2 of the previous chapter, the cross sections of these elements each contain well-known and distinguishable features, which in turn introduce spectral features to the neutron field incident on an external detection system. The task of the analyst is therefore to write a relation between the PHS observed by an external neutron detector, and various treaty-

relevant parameters, as in Eq. 9.1. Here, we would want to include parameters τ_l to represent the presence of various possible neutron sources (i.e. fission versus α-n, for example), and the optical thicknesses of any candidate low-Z elements. We would also likely need to incorporate data other than the neutron PHS into n_i. The PHS from detected gamma rays would likely add constraints on the possible α-n reactions present (many of which produce prominent high-energy gamma-ray lines that would be easy to detect with organic scintillators), and multiplicity measurements could verify the presence of a multiplying source, as would be a required attribute for a nuclear weapon.
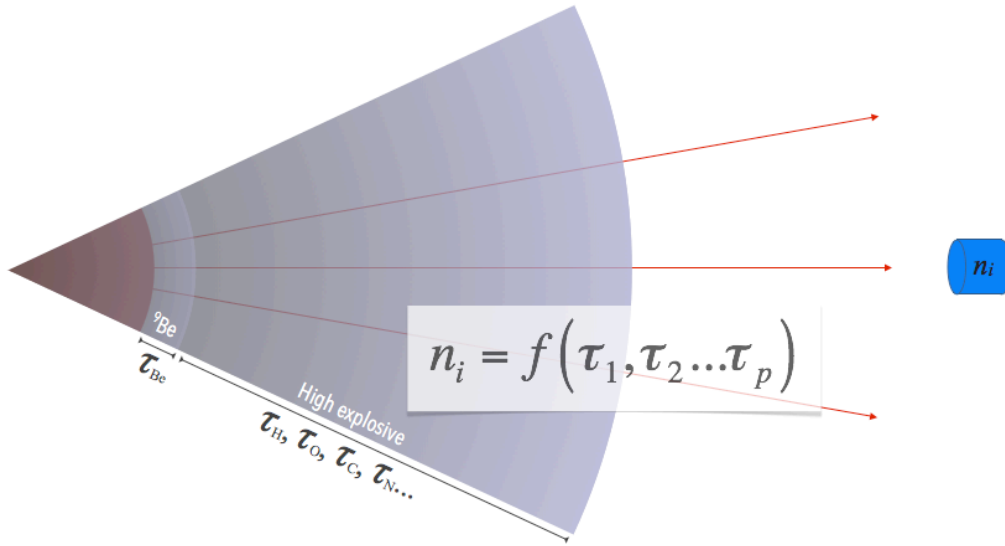
FIG. 9.2. Formulation of warhead-verification problem, writing detector response elements as functionally dependent upon treaty-relevant parameters, such as presence of low-Z constituents of high explosive and neutron reflecting materials.

It is conceivable that some form of Eq. 9.1 could be written that depends on many fewer parameters than our tradition unfolding problem. But the construction of a workable form for Eq. 9.1 in a given warhead-verification scenario is a research project in itself, and beyond the scope of this dissertation. Instead, I will demonstrate the usefulness of adapting the form of Eq. 9.1 to a given problem by considering a simplified one-dimensional attenuation problem, using the same weapons-relevant materials with a known incident spectrum.

9.3 One-dimensional attenuation problem

As an example of how re-parametrization of the unfolding problem can reduce the number of free parameters, consider a simple one-dimensional case similar to that observed in our accelerator experiments. As in the warhead case, the initial spectrum $W(E_n)$ of neutrons is well known, as is the neutron-interaction cross section σ_l of the each material l through the neutrons pass. Thus, we can represent the attenuated spectrum $\phi^{(mod)}$ incident on the detector as a product of the known initial spectrum $W(E_n)$ and a series of energy-dependent attenuation coefficients:

$$\phi^{(mod)} = W(E_n)\prod_l \exp(-\sigma_l(E_n)\cdot\tau_l) \tag{9.2}$$

where $\sigma_l(E_n)$ is the known energy-dependent total interaction cross section of the lth candidate attenuating material, and τ_l the optical thickness of that material in the attenuator. In order to translate this into a detector response n_i, we can discretize the energy dependence with the same discretization scheme used in our response matrices R_{ij}

$$\phi_j^{(mod)} = W(E_n)\prod_l \exp(-\sigma_{lj}\tau_l). \tag{9.3}$$

The discretized model of the incident spectrum is then acted upon by the detector response matrix R_{ij} to produce a model relating detector response n_i directly to a series of unknown optical thicknesses τ_l:

$$n_i = \sum_j R_{ij}\phi_j^{(mod)} = \sum_j R_{ij}W_j\prod_l \exp(-\sigma_{lj}\tau_l) \tag{9.4}$$

The solution parameters solved for are the optical thicknesses τ_l of the candidate materials. This allows us to utilize the known energy dependence of each $\sigma_l(E_n)$ to constrain the solution space: if there are around ten or so candidate materials, this implies that the dimensionality of the problem is reduced by a factor of ten. There are, of course, many materials out of which attenuators could be made. But in this area nature appears to have been kind: the majority of

isotopes either contain little or no structure in their cross sections over our energy range of interest, or they contain structure which is so fine that it appears flat to our detectors. These might be represented by a composite term. The materials we are interested in, on the other hand, do contain distinguishable features, as seen in Chapter 8.
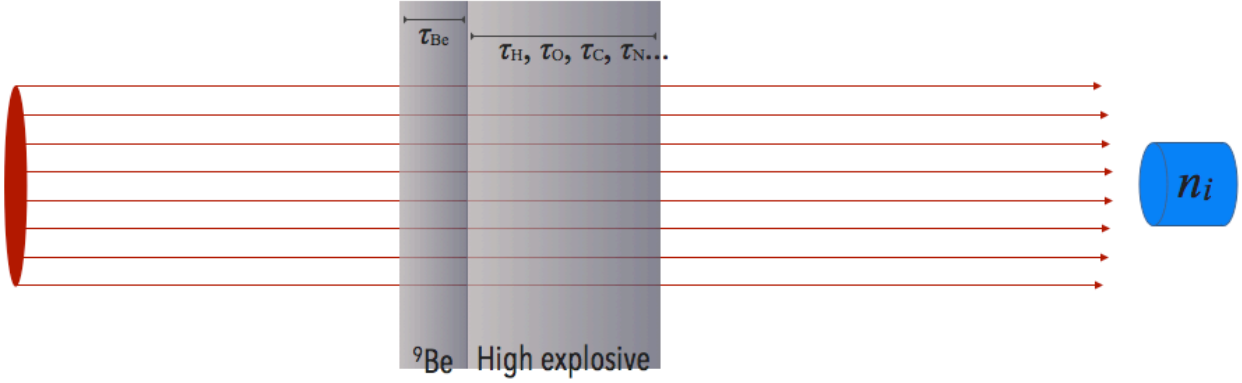
FIG. 9.3. Simplified one-dimensional attenuation problem, solving for optical thickenesses τ_j of attenuating low-Z elements.

9.3.1 Measured pulse-height spectra with single attenuators

I first demonstrate this technique using the purely measured spectra described in Chapter 8. Each includes a single attenuating material, through which a beam of neutrons from ^{11}B(d,n) passes. The initial spectrum from the reaction was measured separately, and is shown in Fig. 4.7. Cross sections for each material were obtained from ENDF [4], re-discretized into 100-keV energy bins, and normalized by density such that the thicknesses are written in units of length. A residual vector is calculated as

$$r_i = n_i^{(mod)} - n_i^{(meas)} . \qquad (9.6)$$

Four thickness terms τ_j are solved for by minimizing the residual 2-norm using a Levenberg-Marquardt method.

TAB. 9.1. Estimated attenuator thickness from measured pulse-height spectra.

Elements of interest	Materials used	Thickness τ^o (cm)	Estimated thickness τ_j and discrepancy (%)			
			H_2O τ_w (cm)	Graphite τ_C (cm)	Nitrogen τ_N (cm)	Beryllium τ_{Be} (cm)
^{1}H, ^{16}O	Distilled water	5.2 (+/- 0.1)	5.06 (-3%)	10^{-14}	0.3 (+8%†)	0.01
^{Nat}C	Graphite	3.8 (+/- 0.1)	0.05 (+1%†)	3.44 (-9%)	0.46 (+12%†)	0.07 (+2%†)
^{14}N	Liquid nitrogen	12 (+/- 1.5)*	0.78 (+7%†)	10^{-8}	12.4 (+3%)	0.01
^{9}Be	Beryllium metal	3.8 (+/- 0.05)	10^{-9}	10^{-10}	0.12 (+3%†)	3.6 (-6%)

* Liquid nitrogen contained in thin-walled cylindrical dewar †When true material thickness is zero, percent deviations are w.r.t. thickness of thinnest present material

Table 9.1 shows the results of each trial. Each row corresponds to a single trial, listing the attenuating material used, its measured thickness (as a reference), and the estimated thickness of each candidate material included in Eq. 9.5. In each trial, the thickness of the present material is estimated to within 10%, while the estimated thicknesses of the absent materials are generally small. When an appreciable thickness is (erroneously) estimated for a material that is absent in the measurement, the percent deviation (in brackets) is given with respect to the actual thickness of the present material. For instance, in the trial with ^{12}C, the results of the calculation erroneously suggest the presence of 0.46 cm of liquid nitrogen, which is 12% of the actual thickness of the ^{12}C attenuator. Most of the estimates for absent materials descend to very small levels, indicating essentially the appropriate null result.

9.3.2 High-explosive attenuators

The next step is to see if solutions can be estimated when multiple materials are actually present. Unfortunately, there was not sufficient time with the accelerator measurements to measure trial spectra using combinations of attenuators, so we must resort to Monte Carlo simulations. However, we still want to maintain the realism of measured PHS. I have devised a

method for achieving both of these aims by simulating the attenuated spectra $\phi^{(0)}$ using MCNP, and constructing the associated PHS out of measured TOF and pulse-height data.

For the attenuating materials, three different combinations of Be metal and HE material will be simulated. While many types of HE are listed in the MCNP compendium of materials [5], we can divide them into three categories, and perform a simulation which approximates the composition of each category. The compounds RDX and HMX fall into a first category, labeled HE1. The case labeled HE2 roughly corresponds to nitroglycerin, while the third case is TNT. In each case, a 15-cm-thick slab of material containing ^{1}H, ^{14}N, ^{12}C and ^{16}O is simulated, with the relative amounts of each element present chosen to approximate the composition of the HE category represented. In addition to the HE, each case also contains a small slab of beryllium metal. The absolute thicknesses of each material are listed in Tab. 9.2. Neutrons of a Watt spectrum are passed through the attenuators in each simulated case, and a surface tally is performed downstream of the slab to calculate the attenuated spectrum $\phi^{(0)}$ which would be incident on a detector placed there. Figure 9.4 shows resulting spectra $\phi^{(0)}$ calculated in this way for each case. For orientation, note that the dominant feature in all three spectra is the peak associated with the gap or valley in the cross section for ^{16}O.
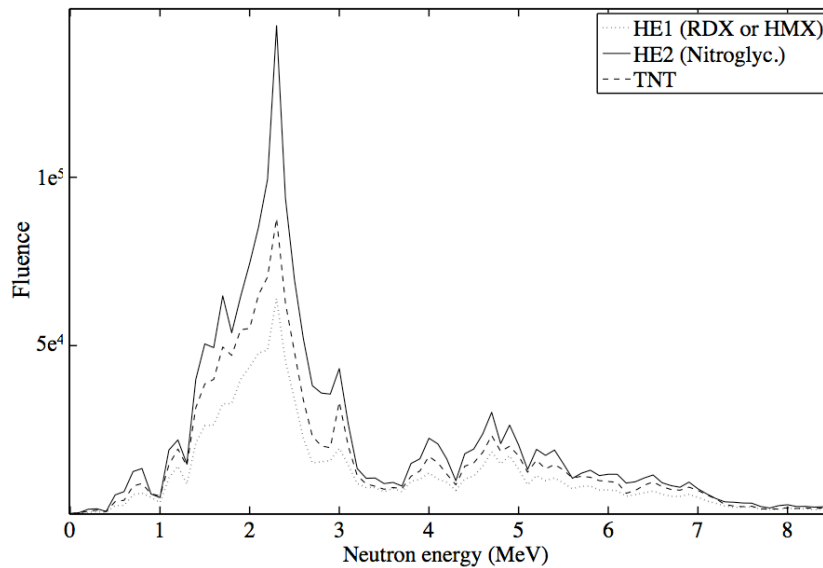
FIG. 9.4. Attenuated neutron spectra, simulated via surface tally in MCNPx, for attenuators approximating three different HE compounds, along with beryllium metal.

The process for constructing PHS $n^{(obs)}$ associated with these simulated spectra $\phi^{(0)}$ out of measured data is as follows. For each energy group j in the discretized spectrum $\phi^{(0)}$, the total fluence ϕ_j is multiplied by the detector efficiency ε_j over that energy group, to estimate the number of detected neutrons in the group

$$\phi_j^{(det)} = \varepsilon_j \cdot \phi_j^{(o)} . \tag{9.7}$$

Then, $\phi_j^{(det)}$ neutron pulses are drawn from within the jth TOF-calculated energy group from a set of measured TOF and pulse-height data, measured as described in Chapter 4. The pulse-height data from these counts are added to the constructed PHS. This constructed PHS contains all the attributes listed in Tab. 10.2 that complicate the unfolding process with real measured spectra, but are associated with known spectra $\phi^{(0)}$ determined in the simulation process. The resultant PHS are shown in Fig. 9.5, and they serve as the "observed" PHS $n^{(obs)}$ for our trials.
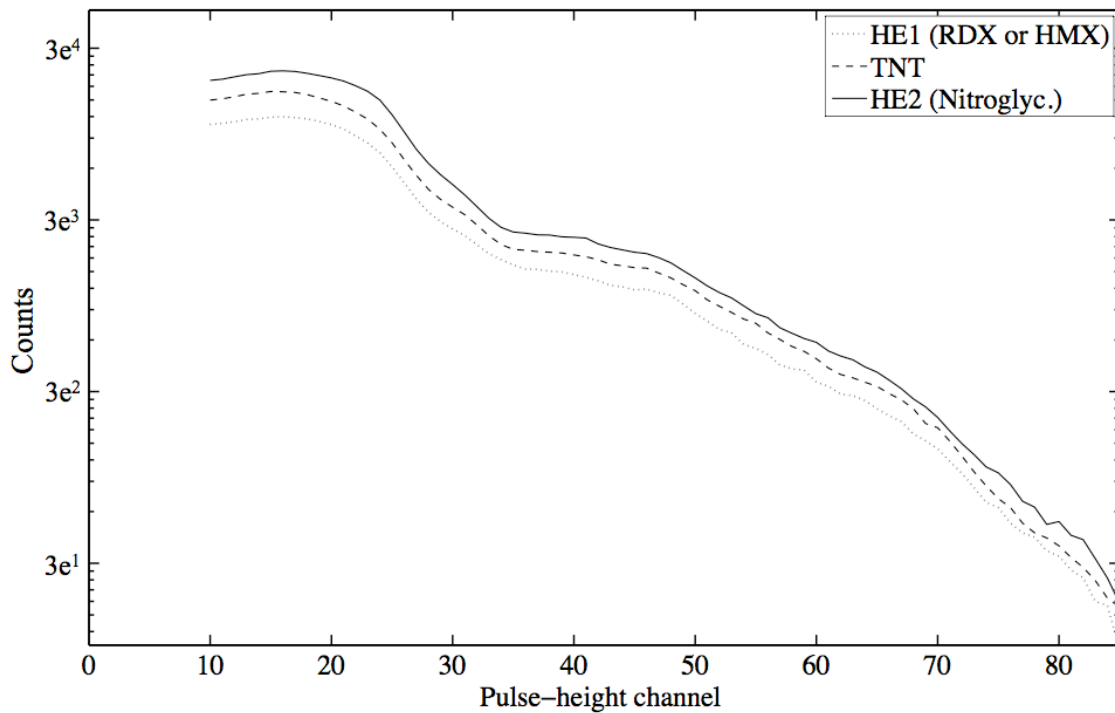
FIG. 9.5. Pulse-height spectra, constructed from measured data, associated with the simulated neutron spectra shown in Fig. 9.4.

As in the previous section, elemental compositions of the attenuator in each trial is estimated by minimizing the 2-norm of the residual between $n^{(model)}$ and $n^{(obs)}$. The results are given in Tab. 9.2. Most of the estimates are correct to within 10%, indicating impressive success of the method. There appear to be some systematic effects leading to patterns in the discrepancies. For instance, the estimate is high for carbon in all three trials, while it is consistently low for beryllium.

TAB. 9.2. Estimated attenuator thickness from pulse-height spectra constructed from measured data using simulated incident spectra.

Elements of interest	Case1: RDX (approx.)		Case2: NG (approx.)		Case3: TNT (approx.)	
	Simulated τ^o (cm)	Estimated τ^{est} (cm)	Simulated τ^o (cm)	Estimated τ^{est} (cm)	Simulated τ^o (cm)	Estimated τ^{est} (cm)
^{1}H	0.33	0.30 (-10%)	0.33	0.31 (-7%)	0.33	0.29 (-13%)
^{16}O	6	5.6 (-7%)	9	8.5 (-6%)	6	5.8 (-3%)
^{Nat}C	3	3.27 (+9%)	3	3.32 (+11%)	6	6.5 (+8%)
^{14}N	6	6.2 (2%)	3	3.1 (+3%)	3	3.2 (+7%)
^{9}Be	3.81	3.6 (-5%)	2.5	2.35 (-6%)	3	2.75 (-8%)

In order to investigate whether these discrepancies were systematic, An analysis similar to that described in Section 10.4 was performed. For each case presented in Tab. 9.2, 10^3 Poisson-variant trial spectra were created, using $n^{(obs)}$ for the mean of the Poisson distribution. Estimated thicknesses τ^{est} were calculated from each of these, and the results are histogramed in Fig. 9.6. As can be seen, the distribution of results for each material are contained within a Gaussian-like cluster. For the estimates that deviate by a large amount, the FWHM of the distribution of estimates is considerably smaller than the size of the discrepancy, indicating that the discrepancy is systematic, and could potentially be corrected for.
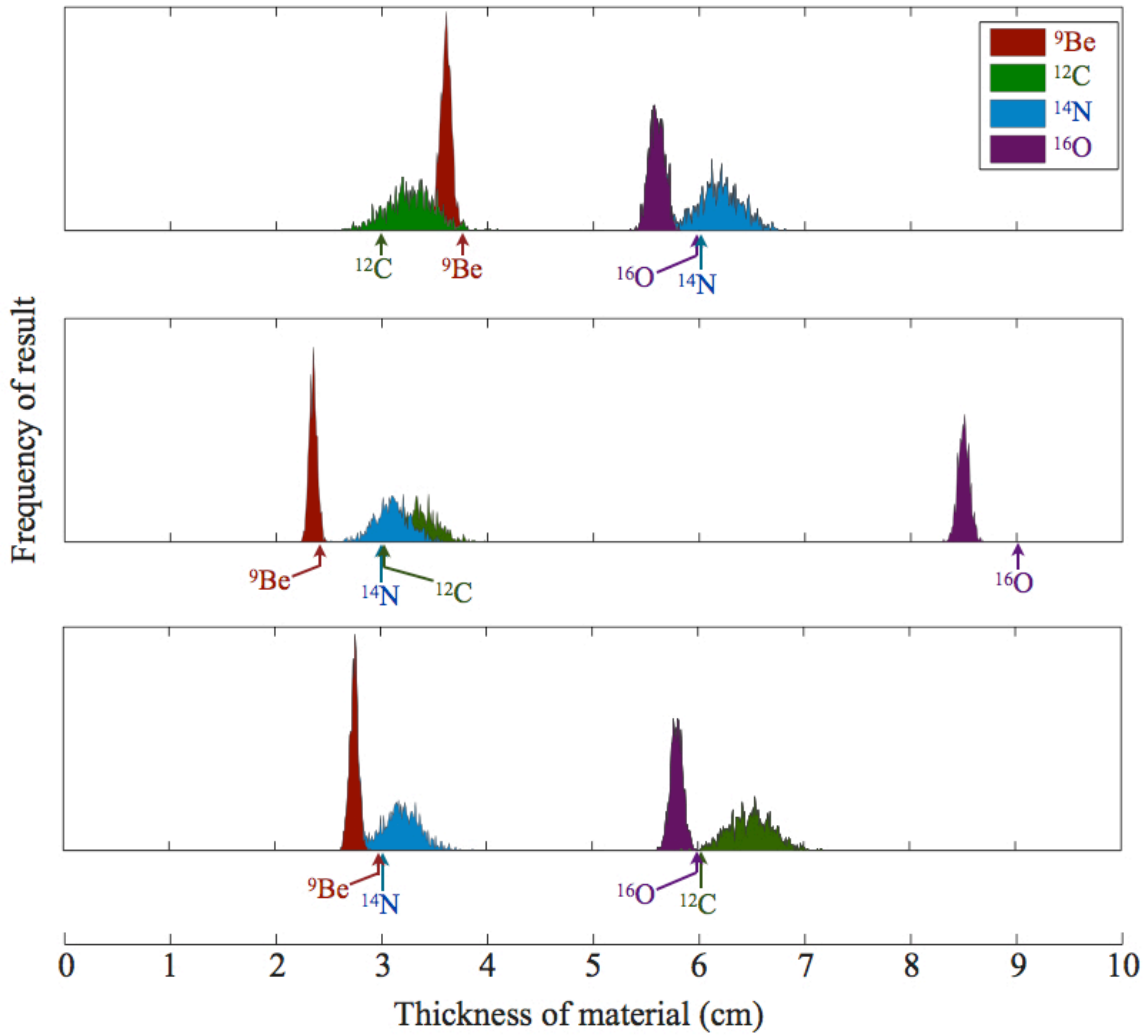
FIG. 9.6. Analysis of the effect of Poisson variance in pulse-height spectra on the estimated thicknesses τ^{est} of attenuating materials. Arrows indicate correct solution values τ^0.

In any case, each type of HE material is clearly distinguishable from the others in Fig. 9.6, regardless of the discrepancies mentioned above. This indicates that useful estimates of elemental composition can be made using scintillator PHS.

9.4 Remarks

In this chapter, it was argued that the key to drawing useful information out of scintillator PHS is to re-parametrize the unfolding problem to reflect the challenge at hand. By incorporating a priori information about the measurement system into the functional form of an operator

relating detector response n_i to relevant parameters of interest τ_w, we can constrain the inverse problem into a lower-dimensional space. This would be a useful approach in the highly controlled environment envisioned for warhead verification. This approach was demonstrated on a simple one-dimensional attenuation problem, in which it was possible to extract an estimate of the elemental composition of the attenuating material from scintillator pulse-height data alone. While this problem differs from the three-dimensional case seen in warhead verification, it illustrates a general approach that could prove useful for verification if developed further.

References

[1]   C. Sublette, "4.1 Elements of Fission Weapon Design," *Nuclear weapon Archive*, 11-Feb-1999.

[2]   R. Serber, "Los Alamos Primer," Los Alamos National Laboratory, Jul. 1996.

[3]   J. Fuller, "Verification on the Road to Zero: Issues for Nuclear Warhead Dismantlement," *Arms Control Today*, pp. 1–11, Jul. 2010.

[4]   *Cross-section Plotter*. [Online]. Available: http://atom.kaeri.re.kr/cgi-bin/endfplot.pl. [Accessed: 09-Jun-2014].

[5]   Employee, "Compendium of Material Composition Data for Radiation Transport Modeling," pp. 1–375, Aug. 2011.

Chapter 10
Concluding Remarks and
Future Systems

The overall aim of this dissertation has been to bring neutron spectroscopy with organic scintillators into the warhead- and material-verification toolbox. Neutron spectroscopy has the potential to fill some persistent holes in current attribute-verification capabilities, such as the distinction between metal and oxide forms of Pu [1], [2], and confirmation of the presence of high explosive materials in a warhead [3]. Since neutron spectra contain much less information than gamma-ray spectra, neutron spectroscopy will likely be more palatable for practitioners concerned with the vulnerability of sensitive warhead-design information. However, verification of warhead and material attributes using neutron spectra would require resolution of spectral features around 100 keV in width [4], a capability that has previously been out of reach for standard hydrogen-based neutron spectrometers. Much progress has already occurred in the area of neutron-spectrum unfolding, and further improvement in the performance of unfolding algorithms comes up against hard informatic limits imposed by the ill-conditioned matrices of standard hydrogen-based scintillators .

In order to improve the performance of neutron spectroscopy systems, I have shifted focus from the unfolding procedure to the detection system on one hand, and to the measurement challenge on the other. By focusing on the attributes of the detection system, I have identified possible improvements in response-matrix condition and stability that can bring about the quality of unfolding results we desire - namely the resolution of spectral features around 100 keV in width. These improvements are listed in Tabs. 3.1 and 3.2. I also showed how a focus on the measurement challenge itself can bring about a re-parametrization of the unfolding problem, and dramatically constrain the number of free solution parameters to allow the extraction of useful information from scintillator pulse-height spectra.

Two considerations are important for the interpretation of this work. First, while the neutron spectroscopy system I envision is realizable with currently-available technologies, it was only partially realized in the system used for this work. Many of the important attributes were demonstrated: deuterated liquids were shown to have superior matrix condition to standard hydrogen-based liquids; light-output-conformed pulse-height binning improved the matrix condition; response matrices were accurately measured using accelerator-based measurements. But other attributes like real-time automated gain adjustment and PSD-enhancing additives [5], were not available to me at the time of these measurements.

Second, the three-dimensional scenario envisioned for warhead verification will differ substantially from the simplified one-dimensional attenuation measurements reported in this thesis. In order for a similar technique to yield treaty-relevant parameters τ_l from warhead measurements, an appropriate model $f(\tau_1, \tau_2..\tau_p)$ must be devised to causally link the parameters τ_l to observable data parameters n_i. In a workable system, these data parameters will likely come from multiple measurement systems, including, but not limited to, scintillator pulse-height spectra. And while the model f used for the one-dimensional case in Chapter 9 was analytically motivated, more complicated models may require iterative MCNP simulations, and/or insight from measurements on actual or artificial test items.

With these considerations in mind, I use this final chapter to sketch a possible way forward for incorporating neutron spectrometry, along with other measurements, in an overall warhead-verification measurement system.

10.1 A deuterated crystal spectrometer?

In choosing a scintillator solution we would like to combine the desirable attributes of deuterated detectors with the superior light output, pulse-height resolution PSD performance obtainable from organic crystals like p-terphenyl or stilbene [6], [7]. While the anisotropic response of organic crystals is a problem in many dosimetry applications, it would not be problematic for the controlled measurements envisioned for warhead verification. Unfortunately, I am unaware of any deuterated crystals that are commercially available at this time, or of any

previous analysis of deuterated p-terphenyl or stilbene spectrometers, and this suggests an area of development that may hold some promise. If large crystals of deuterated p-terphenyl or stilbene could be grown and optimized for high light output, resolution and PSD capability, it may be possible to create a neutron spectrometer with far superior performance than has been demonstrated for organic liquids. This would solidify the place of neutron spectrometry in the arms control toolbox.

The idea of a deuterated crystal spectrometer is not new. In 1988, F.D. Brooks developed a deuterated anthracene spectrometer for neutrons over the energy range from $5 < E_n < 30$ MeV [8]. Brooks did not take the step of unfolding the data, but he demonstrated an intriguing possibility: he invented a PSD technique to gate on backscatter events, yielding a full-energy peak over this energy range. While he considered the resolution of the full-energy peak sufficient for his purposes, unfolding techniques could be used to further enhance the resolution of neutron spectra obtainable from such a detector. If a similar technique could be devised for lower neutron energies, it would represent a further improvement on matrix condition. Unfortunately, this direction appears to have ended with Brooks' 1988 study, and I am unable to find further research on neutron spectroscopy with deuterated crystals. But in light of the potential usefulness of neutron spectroscopy for warhead verification, this research area should be revived.

10.2 Stabilization of PMT gain and PSD performance

In order to obtain stable unfolding results, PMT gain and PSD performance must be uniform across measurements. For the unfolding trials described in Chapter 8, uniformity of these attributes between the matrix measurement and the trial measurements was enforced artificially using TOF with a long flight path. Of course, long-flight-path TOF would not be available for verification measurements, so these attributes must be stabilized using means inherent in the detection system.

Systems for the stabilization of PMT gain are already well developed. A standardized light pulse is periodically introduced to the scintillator active volume during the measurement, via an optical port in the scintillator cell. Throughout the measurement, automated systems can

adjust the PMT gain in real time such that the total integrated charge of PMT pulses associated with the standardized optical pulses remains constant. This calibration data can be acquired during the matrix measurement, and used during field measurements to conform the PMT gain to that used during the matrix measurement.

Regarding the stability of PSD performance, I have several comments. First, if crystal scintillators are used, considerably better PSD performance can be obtained [9]. For instance, in our stilbene detectors, there is virtually no PSD misclassification above a threshold of 100 keVee. If liquids are used, there are ways to enhance the PSD performance using proprietary additives available from Eljen Technologies. In a previous publication, we demonstrated PSD performance in a PSD-enhanced EJ315 liquid that was similar to that of our stilbene crystals [5]. If neutron and gamma-ray misclassification is negligible, then slight shifts in the location of the PSD gate thresholds will not effect unfolding performance. Finally, other members of DNNG are currently developing systems for automated placement of the PSD gate thresholds relative to features in the PSD plot, such that if those features shift, the gate thresholds would shift accordingly [10]. These systems should be validated using accelerator-based TOF measurements, as in Ref. [11]. It is important to remember that the considerations of PSD performance that are relevant to unfolding performance are different than those relevant to other applications. But with these developments and further research on the sensitivity of unfolding performance to PSD quality, it is reasonable to expect that stable PSD performance will be possible with current and future systems.

10.3 Detector arrays and coincidence information

A fieldable neutron spectrometry system for warhead verification should include multiple detectors for two (good) reasons. Most obviously, the improvement in absolute efficiency would be very beneficial - probably required - for obtaining measurement statistics sufficient for arriving at a stable solution of the unfolding problem. Second, depending on how data is acquired, multiple detectors can acquire neutron multiplicity information useful for obtaining other treaty-relevant attribute data, or for further constraining unfolding solutions. For instance,

measurement of double-coincident neutron detections can distinguish between a fissioning source and an alpha-n source, or be combined with neutron-spectral data to estimate the amount of fissioning material [12]-[15]. Multiplying sources can be distinguished by utilizing higher-order multiplicity counts (triples, etc.) [12], [13], or by correlating the time delay between coincident detections with pulse-height information [14]. While it is not clear what aspects of multiplicity counting will be considered sensitive to practitioners in a hypothetical future dismantlement scenario, research should be carried out to determine what information is derivable from scintillator arrays that combine spectral and multiplicity datas of various complexities.

10.4 The three-dimensional warhead verification problem

If we approach the warhead-verification problem as we did the one-dimensional attenuation problem in Chapter 7, then our task is to write down a forward operator $f(\tau_1, \tau_2..\tau_m)$ which relates a series of treaty-relevant parameters τ_p to a set of observable data parameters n_i acquired by various means. Thus, an important direction for research is to turn our attention to the possible test items themselves. Surrogate test items could be constructed out of simple fission and α-n sources, surrounded by concentric shells of low-Z materials like Be metal and HE simulants. Parallel models could be constructed analytically and in Monte Carlo simulations. While a three-dimensional test item is more complicated than the one-dimensional case, our task is likely made considerably easier by the geometrical symmetries - spherical or ellipsoidal - of nuclear warheads. Nevertheless, the contribution of single- and double-scattered neutrons would likely have to be incorporated into f, and/or reduced through various shielding arrangements. Other forms of data, such as acoustic tomographic imaging [16] or electromagnetic coil impedance measurements [2], could also be incorporated to further constrain desired parameters τ_p. But whatever the forms of data, charting the space of possible test items, and constructing the corresponding models f, would put us in the position to extract treaty-relevant parameters from otherwise ambiguous datas n_i like scintillator pulse-height spectra.

References

[1]   A. Peurrung, R. Arthor, B. Geelhood, R. Scheel, R. Elovich, and S. Pratt, "Origin of the 871-keV Gamma Ray and the 'Oxide' Attribute," Pacific Northwest National Laboratory, PNNL-13180, Mar. 2000.

[2]   R. Kouzes and B. Geelhood, "Composite Signatures of Nuclear and Non-nuclear Technologies for Weapons Material Component Verification," Pacific Northwest National Laboratory, PNNL-13861, Apr. 2002.

[3]   D. Archer, "Third Generation Attribute Measurement System," presented at the Institute for Nuclear Materials Management, 53rd Annual Meeting, 2012, pp. 1–4.

[4]   R. C. Runkle, A. Bernstein, and P. E. Vanier, "Securing special nuclear material: Recent advances in neutron detection and their role in nonproliferation," *J. Appl. Phys.*, vol. 108, no. 11, p. 111101, 2010.

[5]   C. C. Lawrence, A. Enqvist, M. Flaska, S. A. Pozzi, and F. D. Becchetti, "Comparison of Spectrum-unfolding Performance of (EJ315_ and (EJ309) Liquid Scintillators on Measured Cf-252 Pulse-height Spectra," *Nuclear inst. and Methods in Physics Research, A*, vol. 729, no. C, pp. 924–929, Nov. 2013.

[6]   N. P. Zaitseva, J. Newby, S. Hamel, L. Carman, M. Faust, V. Lordi, N. J. Cherepy, W. Stoeffl, and S. A. Payne, "Neutron detection with single crystal organic scintillators," presented at the SPIE Optical Engineering + Applications, 2009, vol. 7449, pp. 744911–744911–10.

[7]   C. Matei, F. J. Hambsch, and S. Oberstedt, "Nuclear Instruments and Methods in Physics Research A," *Nuclear inst. and Methods in Physics Research, A*, vol. 676, no. c, pp. 135–139, Jun. 2012.

[8]   F. D. Brooks, W. A. Cilliers, B. R. S. Simpson, F. D. Smit, M. S. Allie, D. T. L. Jones, W. R. McMurray, and J. V. Pilcher, "Deuterated Anthracene Spectrometer for 5-30 MeV Neutrons," *Nuclear Instruments and Methods in Physics Research A*, vol. 270, pp. 149–149156, Jun. 1988.

[9]   N. Zaitseva, A. Glenn, L. Carman, R. Hatarik, S. Hamel, M. Faust, B. Schabes, N. Cherepy, and S. Payne, "Pulse Shape Discrimination in Impure and Mixed Single-Crystal Organic Scintillators," *IEEE Transactions on Nuclear Science*, vol. 58, no. 6, pp. 3411–3420, Dec. 2011.

[10]   J. K. Polack, M. Flaska, A. P. Enqvist, and S. A. Pozzi, "A Computer-aided, Visual Charge-integration Pulse-discrimination Method for Organic Scintillators," presented at the Institute for Nuclear Materials Management, 54th Annual Meeting, Palm Desert CA, 2013.

[11]   C. C. Lawrence, A. Enqvist, M. Flaska, S. A. Pozzi, and F. D. Becchetti, "Gamma-ray and Neutron Misclassification Rates Versus Pulse-height in Organic Scintillation Detectors EJ309, and EJ315.," presented at the Institute for Nuclear Materials Management, 53rd Annual Meeting, 2013, pp. 1–7.

[12]   R. Kouzes and B. Geelhood, "Methods for Attribute Measurement and Alternatives to Multiplicity Counting," Pacific Northwest National Laboratory, PNNL-13250, May 2000.

[13]   N. Ensslin, W. C. Harker, M. S. Krick, D. G. Langner, M. M. Pickrell, and J. E. Stewart, "Application Guide to Neutron Multiplicity Counting," Los Alamos National Laboratory, LA-13422-M, Apr. 1998.

[14]   E. C. Miller, "Characterization of Fissionable Material using a Time-Correlated Pulse-Height Technique for Liquid Scintillators," University of Michigan, 2012.

[15]   J. Dolan, "Safeguarding Special Nuclear Material by Detecting Fast Neutrons in Liquid Scintillators," University of Michigan, 2013.

[16]   N. Duric, C. Li, O. Roy, and S. Schmidt, "Acoustic tomography: Promise versus reality," presented at the 2011 IEEE International Ultrasonics Symposium (IUS), pp. 2033–2041.